



Cite this: *Energy Environ. Sci.*,
2018, **11**, 476

New-generation integrated devices based on dye-sensitized and perovskite solar cells

Sining Yun, ^{*a} Yong Qin, ^b Alexander R. Uhl, ^c Nick Vlachopoulos,^d
Min Yin, ^e Dongdong Li, ^e Xiaogang Han ^f and Anders Hagfeldt ^d

The sharp increase of research passion in the new-generation solar cells in recent years has resulted in a new trend in combining multiple types of energy devices in a single device. In view of the enhanced and/or diversified function of integrated devices, as compared with conventional devices with limited performance or sole applicability, many integrated power packs have been widely developed by combining different devices, such as a silicon solar cell (SSC), Cu(In,Ga)(Sn,Se)₂ (CIGS), organic solar cell (OSC), dye-sensitized solar cell (DSSC), perovskite solar cell (PSC), lithium-ion battery (LIB), nano-generator (NG), supercapacitor (SC), photoelectrosynthetic cell (PESC), and electrolysis cell (ELC), into one unit. In this Review, with a particular emphasis on their recent advances, we cover the integrated solar cell device research in a broad sense and provide an overview of state-of-the-art progress on the integrated solar cell devices based on DSSC and PSC, such as DSSC/LIB, DSSC/SC, DSSC/NG, DSSC/LIB/NG, PSC/OSC, PSC/CIGS, PSC/PSC, PSC/SSC, SSC/SC, PSC/SC, OSC/SC, DSSC/PESC, PSC/PESC, and PSC/ELC, for energy harvesting and storage that are significantly important for self-powering systems and portable/wearable electronics. Finally, the challenges and future outlooks in this promising photovoltaic (PV) field are featured on the basis of current development.

Received 5th November 2017,
Accepted 3rd January 2018

DOI: 10.1039/c7ee03165c

rsc.li/ees

Broader context

The integration of devices, that is the combination of several technologies in a single unit, is a powerful means to improve the performance of a system, reduce its size and weight, and widen its applicability. Both dye-sensitized- (DSSC) and perovskite- (PSC) based solar cell technologies have received growing attention with respect to device integration on account of increasing performance values and their ease of processing at low temperatures. Three main areas of integration can be distinguished depending on their combinations with (i) other solar cells, (ii) electrical energy storage devices, and (iii) electrochemical devices for energy storage in solar fuels. This Review aims to provide a comprehensive summary of the current status and recent research trends and highlights in the area of integrated devices employing both DSSCs and PSCs. Our concluding remarks and future outlook offer a critical evaluation of various power systems and discuss challenges and opportunities for their successful realization and marketability.

1. Introduction

1.1. Solar energy resource and photovoltaic technologies

Human activities strongly depended on the abundance of natural resources (especially water, minerals, and energy). A sustained population growth and the desire for improved living conditions make people have an increasing energy demand that may be far beyond the available conventional energy supply such as coal, petroleum, and natural gas. The estimated energy consumption of the world will reach 27 Terawatt-years in 2050.^{1,2} This means that the energy consumption pattern need be shifted from finite energy reserves to renewable resources in a more efficient manner, and by doing so, reduce our dependence on traditional fossil fuels, mineral, and natural resources. In this regard, utilizing renewable energy is of importance for a

^a Functional Materials Laboratory (FML), School of Materials & Mineral Resources, Xi'an University of Architecture and Technology, Xi'an, Shaanxi, 710055, China. E-mail: alexsyun1974@aliyun.com, yunsining@xauat.edu.cn; Fax: +86-29-82205245; Tel: +86-29-82205245

^b Institute of Nanoscience and Nanotechnology, School of Physical Science and Technology, Lanzhou University, Lanzhou, Gansu, 730000, China

^c Department of Chemical Engineering, University of Washington, Seattle, WA 98195, USA

^d Laboratory of Photomolecular Science, Institute of Chemical Sciences Engineering, École Polytechnique Fédérale de Lausanne (EPFL), 1015 Lausanne, Switzerland

^e Shanghai Advanced Research Institute, Chinese Academy of Sciences, Shanghai 201210, China

^f Center of Nanomaterials for Renewable Energy (CNRE), Key Lab of Smart Grid of Shaanxi Province, State Key Lab of Electrical Insulation and Power Equipment, Xi'an Jiaotong University, Xi'an, Shaanxi, 710049, China

sustainable development of our society and the protection of our planet/environment.

Comparing various energy resources of our planet (Fig. 1), the potential of solar energy dwarfs the potential from any other energy resource on the planet.^{1,2} Solar energy produced from sunlight striking the earth in 1 h is higher than all the energy consumed by human beings on the planet in one year. Therefore, solar energy, as the most abundant renewable energy source on the planet, can be harvested and transformed into various forms of energy for practical applications by thermo-electric, photocatalytic, photovoltaic (PV), and photoelectrochemical (PEC) technologies. Among them, the PV technology as one model of solar energy utilization is generally deemed to play a critical role in capturing solar energy and directly transforming it into electrical energy.

The PV technologies are growing in high speed in basic research and industrialization. Historically, the development of solar cells, from the first crystalline silicon solar cell (SSC) with 6% efficiency envisioned by Bell Lab in 1954 to today, can be divided into three stages.³ The first-generation solar cells are known as silicon-based solar cells (SSCs). The confirmed power conversion efficiencies (PCE) of crystalline silicon cells have exceeded 20% and those of single crystalline cells have reached up to 26.6%.⁴ The SSCs have been an advanced and proven PV technique that are completely dominating the total PV market with a total market share of more than 90%.⁵ The second-generation solar cells are represented by thin-film solar cells such as GaAs, CdTe, and Cu(In,Ga)(S,Se)₂ (CIGS). The confirmed record PCEs are 28.8%, 22.1%, and 22.6% for GaAs, CdTe, and CIGS, respectively.⁶ As compared to silicon-based and thin-film



Sining Yun

Sining Yun is a Professor at School of Materials & Mineral Resources, Xi'an University of Architecture and Technology, China. He obtained his PhD from Xi'an Jiaotong University in 2007 and was a postdoctoral fellow at Yonsei University (Korea). He is a visiting professor at State Key Lab. of Fine Chemicals (China), University of Reading (UK), Prof. Michael Grätzel and Prof. Anders Hagfeldt's laboratory at EPFL (Switzerland). He is currently a

Research Director and Group Leader of Functional Materials Laboratory and Key Lab of Nanomaterials and Nanotechnology of Shaanxi Province (China). His research focuses on solar energy and biomass energy.



Yong Qin

Yong Qin received his BS (1999) in Material Physics and PhD (2004) in Material Physics and Chemistry from Lanzhou University. From 2007 to 2009, he worked as a visiting scholar and Postdoc in Professor Zhong Lin Wang's group at Georgia Institute of Technology. Currently, he is a professor at the Institute of Nanoscience and Nanotechnology, Lanzhou University, where he holds a Cheung Kong Chair Professorship. His research inter-

ests include nanoenergy technology, functional nanodevices and self-powered nanosystems. Details can be found at: <http://www.yqin.lzu.edu.cn>.



Alexander R. Uhl

Alexander R. Uhl is a postdoctoral fellow in Chemical Engineering at the University of Washington (USA) with Prof. Hugh W. Hillhouse. He obtained his PhD in Material Science in 2013 from ETH Zurich (Switzerland) under Prof. Ayodhya N. Tiwari and Prof. Joerg Loeffler. He received his Diploma in Nanostructural Engineering from the University of Wuerzburg (Germany) after graduate stays at the University of British Columbia (Canada) and University of

Uppsala (Sweden), where he worked together with Prof. Marika Edoff. His primary research focus is on solution-processing and characterization of thin film layers for the application in photovoltaic devices.



Dongdong Li

Dongdong Li received his PhD degree in Materials Science from Shanghai Jiaotong University in 2010. Under the support of the Ministry of Education of the People's Republic of China, he worked in the Department of Electrical Engineering at the University of Southern California (2007–2009). Currently, he is a professor at Shanghai Advanced Research Institute, Chinese Academy of Sciences. His research focuses on structural and inter-

facial engineering of functional nanomaterials, for technological applications in energy conversion and storage.

solar cells, the third-generation solar cells such as dye-sensitized solar cells (DSSCs) and perovskite solar cells (PSCs) have the potential for a lower processing cost in the emerging PV fields. Record PCEs of 13% in DSSCs have been obtained while accelerated lifetime tests passed with high durability efficiencies.^{7,8} The newer PSC technology has achieved a champion PCE of 22.1%, which has been independently confirmed by the international authority and authenticating institution, NREL.^{6,9} Large-area PSCs with an aperture area exceeding 1 cm² have achieved a maximum PCE of 20.5% and a certified PCE of 19.6%.¹⁰

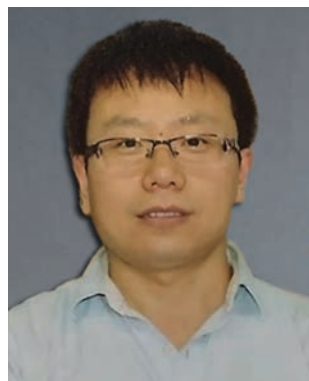
Although the cell efficiencies of the third-generation solar cells are at present still lower than those of silicon-based and thin-film solar cells, the total cell efficiency of the hybrid devices combining PSCs with SSCs is expected to exceed 30% in the near future, while the estimated maximum attainable efficiency in theory for this type of tandem device can reach up to 44%, as predicted by Prof. Michael Grätzel, who is the inventor of DSSCs (or Grätzel cell).¹¹ Remarkably, both the DSSC and PSC technologies can fulfill all of the desired properties of conventional SSCs, such as environment-friendly and earth-abundant materials, high cell efficiency, low-cost and large-scale solution manufacturing processes.

1.2. Dye-sensitized solar cells (DSSCs)

Over the past 20 years, great progress has been made in fundamental research and the technological application for DSSCs. Recent advances and the basic working principles of DSSCs have been summarized in several important review papers.^{12–28} A sandwich-type DSSC is composed of a dye-sensitized mesoscopic TiO₂ photoelectrode, an iodide/triiodide (I⁻/I₃⁻) redox couple electrolyte, and a platinized counter electrode (CE). Generally, each component of a DSSC system performs a specific task. This means that each DSSC component must be carefully designed to meet its practical application.

From 1991 to now, the development of alternative cell components, such as PEs, CEs, electrolytes and dyes, has resulted in a tremendous advancement in the PCE of DSSCs, as illustrated in Fig. 2.^{9,29–45} The PCEs of DSSCs have increased from 7.12% in 1991 to 14.3% in 2015.^{9,11,19} For early metal Ru dye-based DSSCs with an iodine-mediator and a Pt CE, the best reported cell efficiency was 11.7% while lower PCEs of 10.3% were obtained for DSSCs with organic dyes. By contrast, the porphyrin dye can achieve better cell efficiency in cobalt-mediated DSSCs. The champion PCE value of 14.3% was achieved in cobalt-mediated DSSCs with graphene nanoplatelet (GNP) CEs and combined photosensitizers of ADEKA-1 and LEG4 dyes, close to the standard required for commercialization (15%). It is apparent that the superior performance of DSSCs depends strongly on the optimized and well-matched cell components within the device. Note that the substantial increase in PCE in the past two decades has been far lower than that of the recently discovered PSCs. A large amount of publications did not result in a substantial improvement in PCE for DSSCs. This means that more focused research is highly desirable for achieving more efficient and more stable DSSC components. This will promote the practical applications of DSSCs to a broader PV market.

The goal of targeted research projects related to DSSCs is to enhance the industrial application of DSSCs. Advances made in design, incorporation on different substrates, modules, stability, and scalable fabrication techniques have allowed DSSC technology to transfer from the laboratory to practical applications.⁴⁶ Although the cell efficiency of DSSCs is lower than that of silicon-based and thin film solar cells, it is a truth that DSSC panels can deliver more electricity than their silicon-based and thin film counterparts of similar power ratings when they are exposed to weak light operating conditions. DSSC's workability under such conditions makes them become potential market leaders in building and automobile integrated PV and portable or indoor light harvesting PV technology. On the



Xiaogang Han

Xiaogang Han is a professor at Xi'an Jiaotong University (XJTU) in China. He obtained his PhD from the University of Science and Technology of China in 2009, and then worked as a postdoc at the University of California and the University of Maryland in the US, respectively. After that he joined XJTU. Currently, his research interests are solid-state lithium batteries, lithium metal anode, and holey graphene applications.



Anders Hagfeldt

Anders Hagfeldt has been a Professor at the Institute of Chemical Sciences Engineering, École Polytechnique Fédérale de Lausanne (EPFL) and the Head of the Laboratory of Photomolecular Science since 2013. He obtained his PhD in 1993 from Uppsala University and was a post-doctoral fellow with Prof. Michael Grätzel (1993–1994) at EPFL, Switzerland. Before 2014 he was a professor in Physical Chemistry and the director of

Center for Molecular Devices at Uppsala University, Sweden. He is a member of the Royal Swedish Academy of Sciences, European Academy of Sciences, Royal Society of Sciences in Uppsala, and the Royal Swedish Academy of Engineering Sciences in Stockholm.

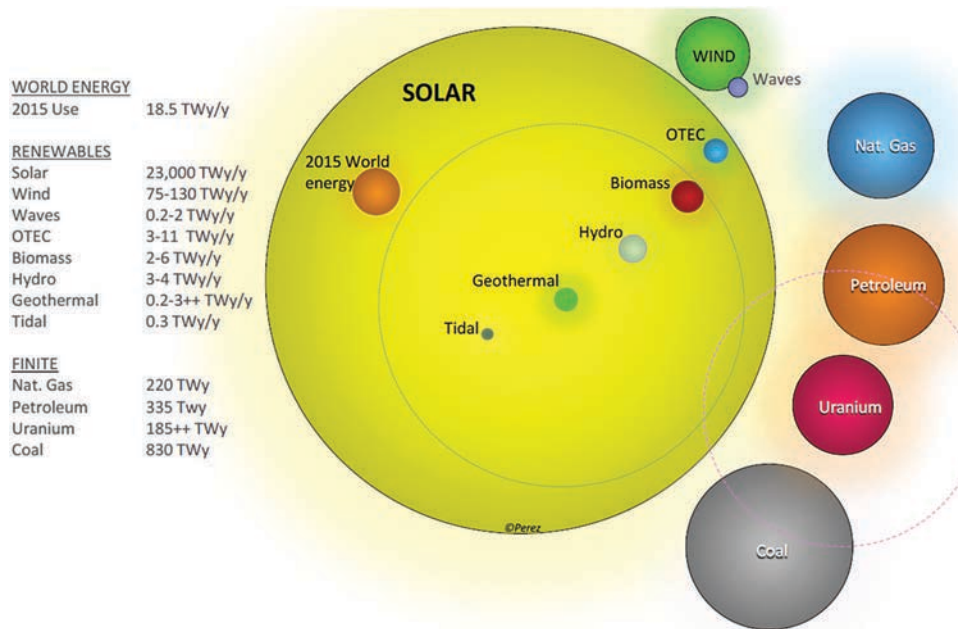


Fig. 1 Estimated finite and renewable planetary energy reserves (Terawatt-years). Note that total recoverable reserves are shown for the finite resources whereas yearly potential is shown for the renewables. Reproduced with permission from ref. 1 and 2. Copyright 2015 International Solar Energy Society.

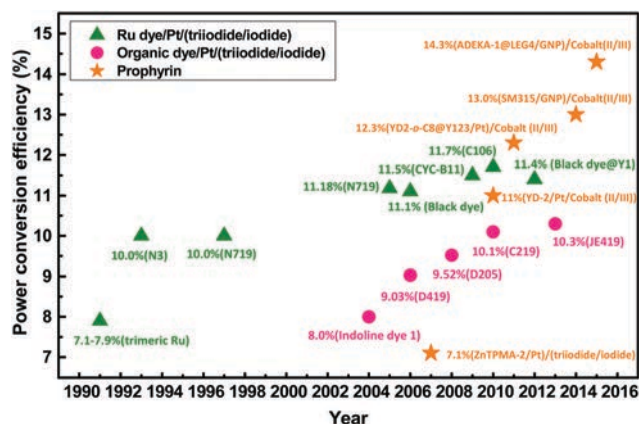


Fig. 2 Advances in PCE for DSSCs with a TiO_2 photoelectrode reported in the past 25 years (1991–2016). For more detailed PV parameters of DSSCs depicted in Fig. 2,^{9,29–45} please refer to our recent reviews.^{15,19,22}

other hand, due to their low-cost and tenability of color and transparency, DSSCs are well suited for BIPV and portable devices. While the former prompts rather large area devices, several applications in the portable device area can be envisaged where small scale integrated devices are useful. Actually, large-area DSSC modules suffer from performance loss and long term stability issues compared to their lab-scale devices.^{13,47–49} The above-mentioned facts are the main reasons that a DSSC system can distinguish itself among other solar cells from building integrated BIPV and portable electronic devices.

Commercial sales of DSSCs have started in solar modules for building integrated PV (BIPV) and portable electronic devices. Three examples are: (1) the energy producing glass facade made of DSSCs in Swiss-Tech Convention Center in Lausanne,

Switzerland,⁵⁰ (2) the electric power generating colored look-through glass panels produced by G2E (www.g2e.ch), and (3) backpacks with integrated flexible DSSCs to produce continuous electricity and stored in a power bank for powering electrical equipment (<http://ipi.epfl.ch>). Reports on integrated devices based on DSSCs are more numerous as compared to PSCs based on the maturity of the DSSC technology. To date, the DSSC technology excels with inherent low toxicity, low cost, and increased long-term stability which has been realized by several commercial companies such as G2E, SOLARONIX, G24 Power Limited, EXEGER, and others. On the way to practical application of DSSC technology, the integrated DSSC devices for energy harvesting and storage will be given a special concern in this review.

We want to stress that the main commercial selling points of DSSCs are (next to the choice of rigid or flexible substrates, low cost, and scalability) their excellent performance under low light conditions (*e.g.* in-door), and tenability of color and transparency. This makes DSSC an excellent choice for BIPV and portable electronic devices.

1.3. Perovskite solar cells (PSCs)

1.3.1. Structural evolution of PSCs. Perovskite materials are well-known for their distinctive crystal structure and unique properties in electronic ceramics (*i.e.* BaTiO_3 -based ferroelectric ceramics).^{51–59} Use of perovskite-structured organometal halide materials (*i.e.* methylammonium-lead iodide, MAPbI_3) as the key materials to fabricate the PSCs, as illustrated in Fig. 3a and b, has become very popular in recent years. An overview of the historical development of the organometal halides has been recently elucidated by Prof. Michael Grätzel in a 2014 Nature Materials article.⁶⁰ In the organometal halide perovskite

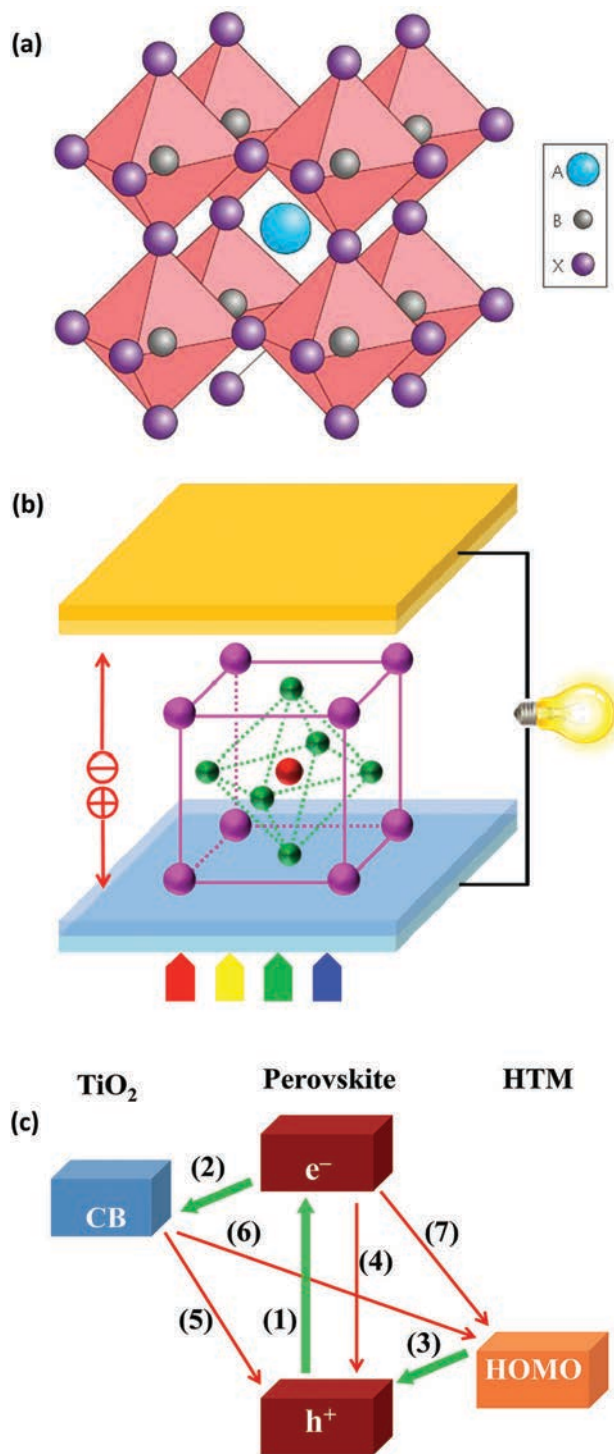


Fig. 3 (a) Crystal structure of cubic metal halide perovskite with generic chemical formula ABX_3 (A site: the large organic cations; B site: the small metal cations; and X site: halogen ions). Reproduced with permission from ref. 61. Copyright 2014 NPG. (b) Organolead halide perovskite materials in PSCs. Reproduced with permission from ref. 67. Copyright 2016 Wiley-VCH. (c) Schematic illustration of the involved charge-transfer processes in PSCs. Reproduced with permission from ref. 66. Copyright 2015 Wiley-VCH.

materials, organic $CH_3NH_3^+$ (MA) and $HC(NH_2)_2^+$ (FA) cations occupy position A whereas metal cations (Pb^{2+} , Sn^{2+}) and

halogen ions (I^- , Br^- , Cl^-) occupy the B and X positions, respectively.⁶¹ Ideal perovskite has a cubic crystal structure while in reality structures are often pseudo-cubic or distorted cubic because of distortion. The distorted structure will evidently affect the optical, electronic, magnetic, and dielectric properties of perovskite materials.⁶²

The working principle of PSCs can be generally demonstrated by the critical charge-transfer processes shown in Fig. 3c. Under light illumination, the perovskite absorbers undergo photo-excitation and charge separation (1), electrons are collected by the ETL and move to the fluorine-doped tin dioxide (FTO) conductive substrate (2), while holes move to the metal contact through the HTM (3). Those light-generated charge carriers (both electrons and holes) produce a potential difference at the front and back contacts of the PSCs and can generate an electric current through a connected external circuit. During the charge-transfer processes, some undesirable charge recombination often occurs at the interfaces of the involved layers. Light-generated electrons can recombine with holes in the perovskite layer (4) and at the interface of perovskite and the HTM layer (7). The injected electrons may further recombine with the holes at the interfaces of ETL/perovskite (5) and ETL/HTM (6). The interfacial properties mainly determine the performance of solar cell devices. The interface molecular engineering has turned out to be one effective strategy to solve the charge recombination that occurs at the interface of PSCs.^{63–66} For achieving high-performance PSCs, charge generation and extraction (1)–(3) must be on much faster timescales than charge recombination (4)–(7).

Today, so-called PSCs originate from the solid-state DSSCs containing perovskite as a sensitizer. The historical evolution of device architectures for the PSCs is in detail depicted in Fig. 4a–d. The incipient PSCs are an exact mimic of the solid-state DSSCs, as illustrated in Fig. 4a. The N719 dye or $MAPbI_3$ perovskite plays the role of a sensitizer that generates electrons and holes that are injected into the conduction band of a mesoscopic TiO_2 scaffold and a solid-state hole-transporter material (HTM) (spiro-OMeTAD in most cases), respectively.^{68,69} In the meso-superstructure (Fig. 4b), a film of mesoporous scaffold Al_2O_3 instead of TiO_2 is covered with an ultrathin conformal coating of $MAPbI_3$ perovskite. It is evident that Al_2O_3 is not able to aid in electron extraction and transport due to its large bandgap. Therefore, $MAPbI_3$ is regarded as a light harvester as well as an electron conductor. This meso-superstructured configuration sporadically suffers from the poor pore filling of the HTM. Although a PCE of up to 10.9% has been achieved, the role of the mesoscopic Al_2O_3 scaffold in these PSC devices remains unclear. It should be noted that $MAPbI_3$ also plays a role of a hole conductor in HTM-free mesoscopic architectures.^{70,71} This is different from its role in the meso-superstructured configuration. A certified PCE of up to 12.8% has been obtained in HTM-free PSCs with excellent stability, as compared with many HTM-based PSCs. Based on the HTM-free architecture, a more advanced architecture has been developed (Fig. 4c) where the mesoscopic TiO_2 scaffold is fully infiltrated with the perovskite light harvester and poly(triarylamine) HTM while the latter

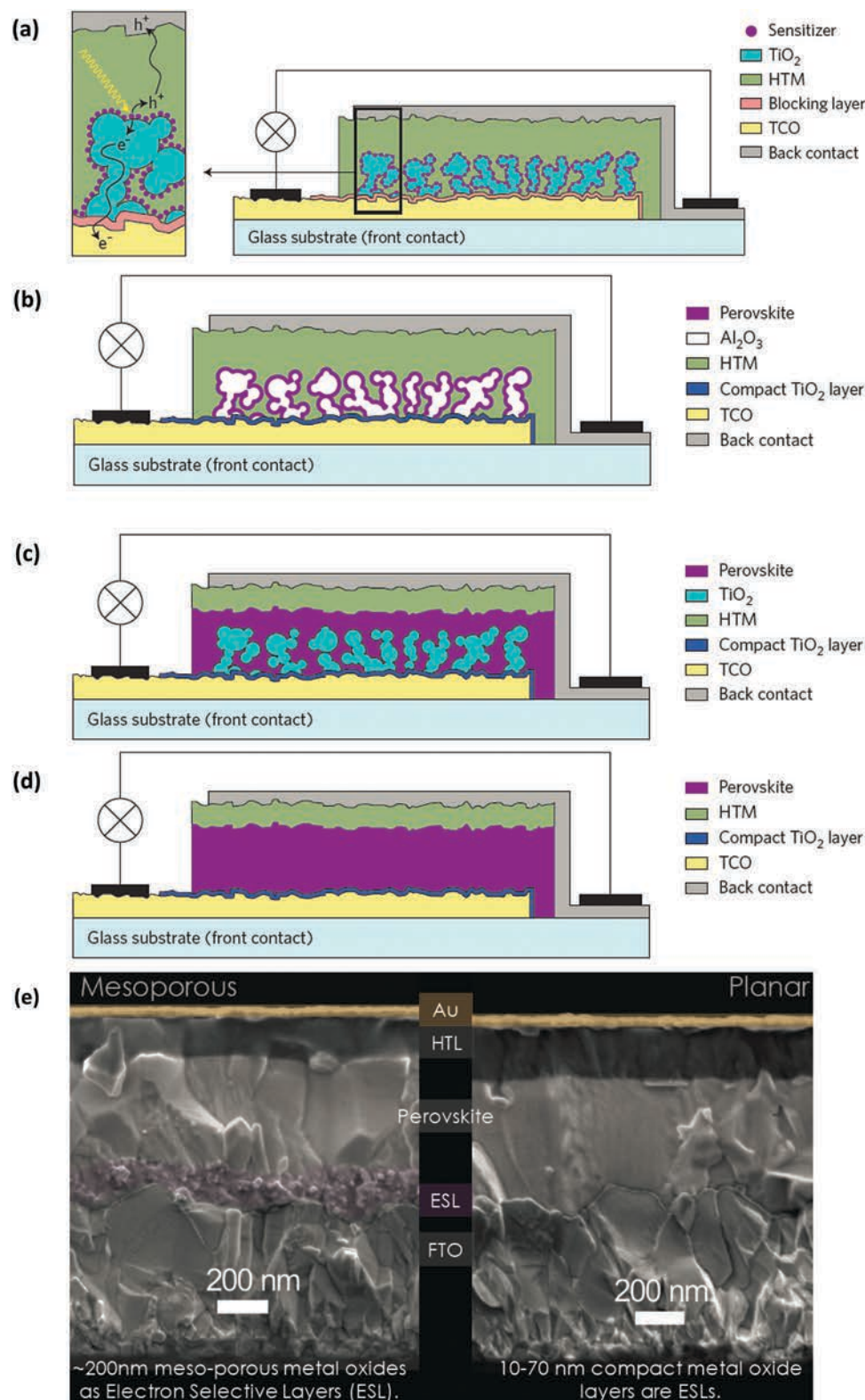


Fig. 4 (a) Solid-state mesoscopic solar cell using MAPbI₃ as a sensitizer and spiro-OMeTAD as an HTM (9.7%). (b) Meso-superstructured Al₂O₃ scaffold covered with an ultrathin layer of MAPbI₃ perovskite (10.9%), (c) the mesoscopic TiO₂ scaffold infiltrated by the perovskite (12%), (d) A planar pn heterojunction solar cell lacking the TiO₂ mesoporous scaffold (15.4%). Reproduced with permission from ref. 60. Copyright 2014 NPG. (e) Cross-sectional scanning electron microscopy (SEM) image of typical layered common device architectures of mesoscopic (left) and planar (right) PSCs composed of fluorine-doped tin dioxide (FTO), ETLs (TiO₂ or SnO₂), the perovskite film, HTM (spiro-OMeTAD), and a gold top electrode. SEM image by courtesy of Dr Juan-Pablo Correa-Baena.

penetrates the mesoscopic scaffold to a much smaller degree. This permeation has been confirmed by energy-dispersive spectroscopy and X-ray diffraction depth profiling technologies.⁷² In this advanced configuration, the perovskite plays the dual role of a light absorber and a hole conductor, and the thickness of the mesoscopic MAPbI₃/TiO₂ nanocomposited film can be reduced to 200–300 nm without photocurrent loss. The high PCE of 12% that was obtained in this configuration indicated that the MAPbI₃ perovskite was very effective as a hole conductor. An improved PCE of 15% was further achieved by the MAPbI₃ infiltrated composite structure with a two-step coating method.⁷³ Since the perovskite can play a dual role in transporting electrons and holes, the mesoscopic TiO₂ scaffold layer is not required. Based on this design idea, the planar pn junction concept was proposed, as depicted in Fig. 4d. A thin layer of perovskite material is sandwiched between the HTM layer and the compact TiO₂ blocking layer, which made the device fabrication much easier than the before-mentioned two configurations. In the PSC architectures with a planar geometry, 300 nm-thick MAPbI_{3-x}Cl_x films were fabricated by vapour deposition of CH₃NH₃I and PbCl₂, and a PCE of 15.4% was achieved.⁷⁴ By contrast, the planar configuration could achieve a similar device performance to the mesoporous configuration. It is noted that a thin TiO₂ blocking layer as the bottom electron transport layer (ETL) is still required in the planar configuration lacking the TiO₂ mesoporous scaffold.

Except for the difference in the design configuration mentioned above, another difference between the mesoscopic and the planar structure is that approximately 200 nm mesoporous metal oxide (mp-TiO₂) is employed as the electron transport layer (ETL) for the former, whereas an only 10–70 nm-thick compact metal oxide ETL is used for the latter, as illustrated in Fig. 4e. In addition, the role of the perovskite materials changes from an electron conductor in the meso-superstructure configuration to a hole conductor in the mesoscopic-structured configuration besides acting as a light absorber. Although planar and mesoporous configurations have achieved champion PCE records, the mesoporous configuration requires a high temperature (usually greater than 450 °C) sintering process for the TiO₂ scaffold, and the planar configuration based on the TiO₂ ETL usually suffers from a *J*-*V* hysteresis. It should be mentioned that based on this regular planar configuration, an inverted planar structure, which adopted a similar device structure to the OSC devices, was firstly proposed.^{75,76} This inverted planar structure uses p-type and n-type materials as bottom and top charge transport layers, respectively, and the charge transport layers used in OSC devices were successfully transferred into PSC devices. The inverted planar structure of PSCs has shown PCE values as high as 18%, lower temperature processing, flexibility, and, furthermore, negligible *J*-*V* hysteresis effects.⁷⁶

1.3.2. Advances in the efficiency level for PSCs. Each big breakthrough of device configuration can generate a key advance in cell efficiency and fabrication process. The development of the device configuration of PSCs, from DSSCs to the planar heterojunction PSCs, was accompanied by a dramatic advance in PCE

from 3.81% in 2009 to 22.1% in 2016, as presented in Fig. 5a.^{69,71–74,77–90} MAPbI₃ was initially used by Miyasaka and co-workers as a sensitizer in liquid-state DSSCs with a PCE of 3.81% in 2009.⁸³ Subsequently, a PCE of 6.5% was reported in 2011 for perovskite sensitized DSSCs in which perovskite quantum dots were used as sensitizers and the triiodide/iodide redox couple was employed.⁸² A major breakthrough was achieved in 2012, and PCEs of 9.7% and 10.9% were achieved by introducing organometal halide perovskite sensitizers in perovskite-based solid-state DSSCs (or PSCs).^{62,91} As a milestone, these two publications enabled a huge application potential for perovskite materials in low-cost and high-performance solar cells. As a result, more exciting discoveries and great progress in PSCs came within a short period of time from 2012 to 2015. For example, sequential deposition as a route to fabricate high-performance PSCs greatly increased the performance reproducibility and achieved a PCE of 15%. A dual-source vapour-deposited perovskite as the absorbing material yielded a PCE of 15.4% in a simple planar heterojunction PSC. Solvent engineering resulted in extremely uniform and dense perovskite layers for high-performance PSCs with a PCE of 16.2% by combining mesoscopic and planar structures.⁸¹ Compositional engineering by incorporating MAPbBr₃ into FAPbI₃ stabilizes the perovskite phase of FAPbI₃ and improves the PCE of PSCs to 18.4%.⁷⁹ With interface engineering by controlling the formation of the perovskite layer and careful choices of other materials, a PCE of approximately 19.3% was achieved in a planar geometry without an antireflective coating, and while carrier recombination in the absorber was suppressed, good carrier extraction at the electrodes was retained.⁷⁸ The perovskite layers fabricated through intermolecular exchange in PSCs brought about a certified PCE of 20.1%.⁷⁷ Today, the best research-cell efficiency has reached a NREL certified PCE of 22.1% by KRIC/UNIST, which is more than 5.8 times higher than the value achieved in 2009 (3.81%). This is an unprecedented rise in PCE for a PV technology. Moreover, the higher efficiency level indicates that PSCs will have a more efficient operation in the integrated devices based on solar cells.

As discussed, early PSCs came from solid-state DSSCs that can be dated back to 1998 (Fig. 5a), where a PCE of 0.74% was achieved when the HTM spiro-OMeTAD and the N719 dye were used in solid-state DSSCs.⁹⁰ In 2001, the performance of solid-state DSSCs was improved to 2.56% by controlling the charge recombination across the interface of the heterojunction by adding lithium bis(trifluoromethane sulfonimide) (LiTFSI) and *tert*-butylpyridine (tBP).⁸⁵ A replacement of the N719 dye with the metal-free organic D102 dye resulted in an enhanced PCE of 4.1% in solid-state DSSCs in 2005.⁸⁷ The use of D-π-A dye C220 in solid-state DSSCs resulted in a new record of 6.08%, and a PCE of 7.2% was further achieved by using p-type dopant FK102 in 2011.^{84,89} The solid-state DSSCs were not given a special concern at early stages because of the relatively low PCE values. No noticeable advance was made from 2005 to 2011.

A comparison of PCEs of mesoporous and planar PSC is shown in Fig. 5b. This graph illustrates that the PCE of mesoporous PSCs is generally higher than that of planar PSCs.

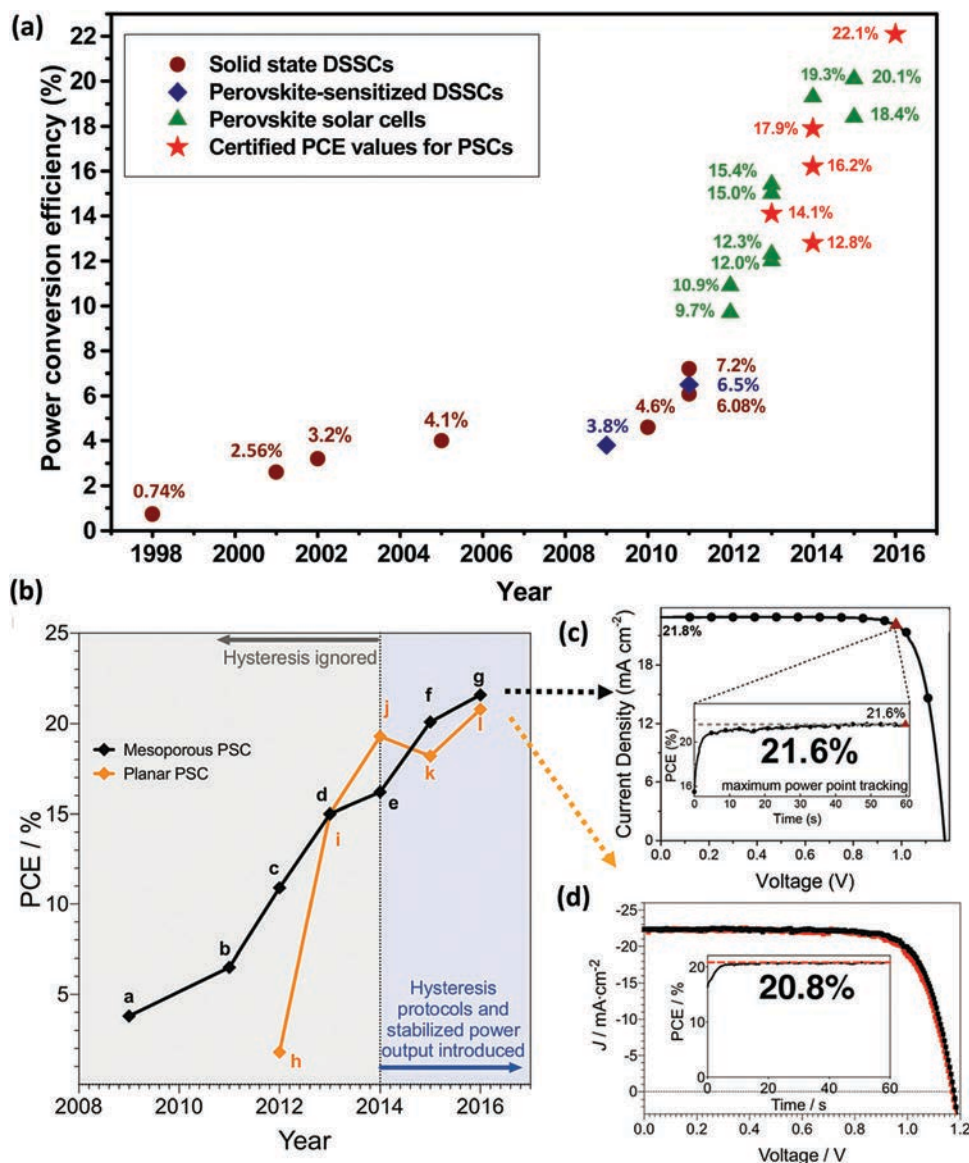


Fig. 5 (a) Some representative PCE advances in perovskite-based and solid-state DSSCs reported in top journals. The certified cell efficiency records resulted from the efficiency chart by National Renewable Energy Laboratory (NREL) (<http://www.nrel.gov/ncpv/>) and ref. 60 and 96. (b) A comparison of PCEs of mesoporous and planar PSCs. The highest published PCE for a TiO₂ mesoporous infiltrated PSC (d). Reproduced with permission from ref. 94. Copyright 2017 RSC.

The current–voltage (J – V) hysteresis phenomenon depending on the forward or backward scan direction was ignored, and non-stabilized efficiencies were measured during the first few years (shaded in grey in Fig. 5b). Many efforts have been made to improve measuring protocols from 2014 to today, and slow scan rates of the J – V curve and/or maximum power point tracking define the record PCEs today (inset in Fig. 5c). A stabilized efficiency of 21.6%, with remarkable V_{oc} values of up to 1.24 V (for a theoretical maximum of 1.35 V), was achieved in TiO₂ mesoporous infiltrated PSCs with multiple cation formulations by incorporating Rb into the Cs/FA/MA perovskite.⁹² By contrast, the highest stabilized PCE of 20.8% with V_{oc} values above 1.19 V was reported in solution-processed SnO₂ as ETLs in planar PSCs (Fig. 5d).^{93,94}

Intrinsically, the high performance of PSCs can be contributed by the fact that ABX₃ are suitable to be efficient light absorber materials to meet desired demands for solar cells, such as an appropriate bandgap for outstanding light-harvesting ability, energy level/band alignment with contacting materials, high charge carrier lifetime, and high charge carrier mobility. High and balanced electron–hole mobility and lifetime mean that the light-generated electrons and holes can move sufficiently large distances (the average carrier-diffusion distance ranging between 100 nm and 1000 nm) to be extracted as a current, instead of losing their energy as heat within the cell.^{60,67,95}

Very recently, accelerated degradation of MAPbI₃ perovskites has illustrated that the release of I₂ vapor can cause MAPbI₃

(including FAPbI_3 and $\text{FA}_{0.8}\text{Cs}_{0.2}\text{PbI}_3$) to be severely degraded due to chemical chain reactions.^{97,98} The volatile I_2 vapor was produced when the MAPbI_3 was subjected to moisture, oxygen, light illumination, thermal stress, and applied electric fields. In this regard, the release of volatile I_2 vapor will be inevitable for PSCs in practical applications. This means that research on alternative perovskite materials is highly required to obtain good long-term stable PSCs.⁹⁷ Interestingly, Pb-free Sn-based CsSnI_3 perovskite ingots with high-quality large single crystal grains have recently been melt-synthesized, and long minority-carrier diffusion lengths reaching 1 μm and low surface-recombination velocities of approximately $2 \times 10^3 \text{ cm s}^{-1}$ (similar to Pb-based perovskites) were measured. A PCE of approximately 23%, beyond the current highest certified efficiency level of 22.1%, was predicted for optimized CsSnI_3 single crystal solar cells, highlighting their great potential in practical applications.⁹⁹ In addition, enhanced stability and cell efficiency in HTM-free CsSnI_3 -based PSCs have been very recently verified.¹⁰⁰ It should be noted that a road towards 25% efficiency and beyond has been recently proposed for tandem PSCs.¹⁰¹ Apart from developing alternative perovskite materials to solve the degradation issue of MAPbI_3 , there are several reported strategies to overcome this challenge;^{98,102,103} for more details, please consult recent review papers.^{104–106}

All kinds of solar technologies will find their own markets, and the new-generation perovskite PV technology is approaching the performance of the existing silicon-based and thin film PV technologies. However, the present efficiency level of PSCs is still far behind the theoretical Shockley–Queisser limit (greater than 34%) and can be expected to be increased further by using revolutionary technologies in the future. In addition, the reproducibility and long-term stability of the PSCs need to be specially addressed to improve the technology's practical utility. Several review papers have recently summarized the progress of PSCs.^{60–62,64,66,67,95,96,106–129} For more composition engineering, interface engineering, solvent engineering, device operation, structure evolution, efficiency achievement, charge transport behavior, stability improvement, commercialization challenge, open issues and pitfalls, and others, please refer to several important papers.^{60,61,64,96,113–115,118}

1.4. Integrated solar cell devices

Solar energy is generally intermittent and is typically installed in remote regions which can make it difficult to connect them directly to the national grid. In addition, solar cells cannot directly store the electrical energy captured from sunlight. Therefore, the intermittence of solar energy creates an urgent demand for suitable energy storage technologies. Currently, the universal practice for energy storage is to externally connect rechargeable batteries to the solar module installation. For example, silicon solar panels and solid-state lithium batteries were conventionally developed as two independent devices. Recent advances in energy harvesting and storage technologies have demonstrated a new trend in harvesting multiple types of energy using a single device.^{130–140} This means that an integrated power pack, energy harvesting and storage technologies

operating together in a power system, may be an effective path to obtain a small sized, light-weight, high power density, and high reliability energy system. In this regard, the development of integrated energy harvesting and storage technologies, that capture and convert solar energy from sunlight with high efficiency, and then consecutively store the electrical energy by means of an electrochemical battery or other devices, is of great importance to meet the special demands in the future.

Present research on new-generation solar cells generally focuses on improving the PCE. Other fields of research like the integration of energy harvesting and storage systems receive only minor attention but are significantly important for emerging markets such as self-powering systems and portable/wearable electronics. Generally, DSSCs, lithium-ion batteries (LIBs), nanogenerators (NGs), and supercapacitors (SCs) can be deposited on a rigid or flexible substrate, which means that they can easily be integrated into one unit. Due to the ease of fabrication and higher efficiency, solar cells are often chosen as sources of electrical energy harvesting whereas LIBs and SCs are often utilized as energy storage units. Great progresses have been made on integrating conventional planar devices for energy harvesting and storage. A planar-shaped integrated device for both PV conversion and energy storage has been realized.^{141,142} As an example, the voltage of the integrated DSSC/SC device can be charged and maintained at 0.72 V with an energy storage efficiency as high as 84% and an entire photoelectric conversion and storage efficiency of 5.12%.¹⁴¹ However, the planar structure can not meet the combined requirements of light weight, miniaturization, and flexibility of modern electronics. To meet these requirements, flexible and fiber-shaped integrated devices have been recently developed.^{130,135,143,144} The integration of new-generation solar cells (DSSCs, PSCs, SSCs, and OSCs) and chemical energy storage technologies (LIBs, SCs) enable us to store flexibly and fully utilize the intermittent solar energy.

In view of the enhanced and/or diversified function of integrated solar cell devices as compared with conventional devices with limited performance or sole applicability, many integrated systems have been widely developed by combining different devices into one unit. DSSCs as low-cost PV devices are especially suited for building and automobile integrated PV and portable/wearable or indoor light harvesting applications.⁴⁶ Although the PCEs of DSSC systems are not on a par with commercially available silicon-based or thin film solar cells, DSSCs possess many features, such as transparency, light weight, flexibility, conformability, workability under weak-light conditions, and easy integration with other devices, that can compel further DSSC's development in modules. Unlike silicon-based devices, DSSCs weakly depend on the angle of incident light and perform much better under low light operating conditions, which makes them suitable energy harvesting devices for integration with other energy storage devices. Note that the transparent and flexible devices deliver low PCEs at the lab scale, which means that the devices turning into practical applications still face many challenges. Likewise, PSCs have

shown great promise for next-generation PV technology, due to their intriguing optoelectronic properties (strong absorption in the visible range,^{145,146} high carrier mobility,^{147,148} bipolar transport,¹⁴⁹ long photo-generated carrier diffusion length),^{150,151} and low cost and high efficiency, which enable realization of highly efficient integrated PV devices. In addition, the research enthusiasm, observed from the increasing number of papers about PSCs, make PSC-based integrated devices a topic of increasing popularity.

The noteworthy examples of integrated solar cell devices based on PSCs and DSSCs are illustrated in Fig. 6. (i) PSCs can be integrated with other solar cells (CIGS, OSCs, and SSCs) into one unit to form a tandem device; (ii) solar cells such as DSSCs, PSCs, OSCs, and SSCs can be integrated with LIBs, SCs, and NGs into one unit to achieve integrated systems; (iii) DSSCs and PSCs can be integrated with photoelectrosynthetic cells (PESCs) into DSSC/PESC and PSC/PESC for hydrogen generation and CO₂ reduction.

The challenge to review the growing research field of integrated devices is the rapidly increasing number of publications and research data. With the risk of missing some interesting and important works for developing the integrated solar cell technologies, the purpose of this review is to cover the integrated solar cell device research in a broad sense and provide an overview of trends in solar energy harvesting and storage applications.

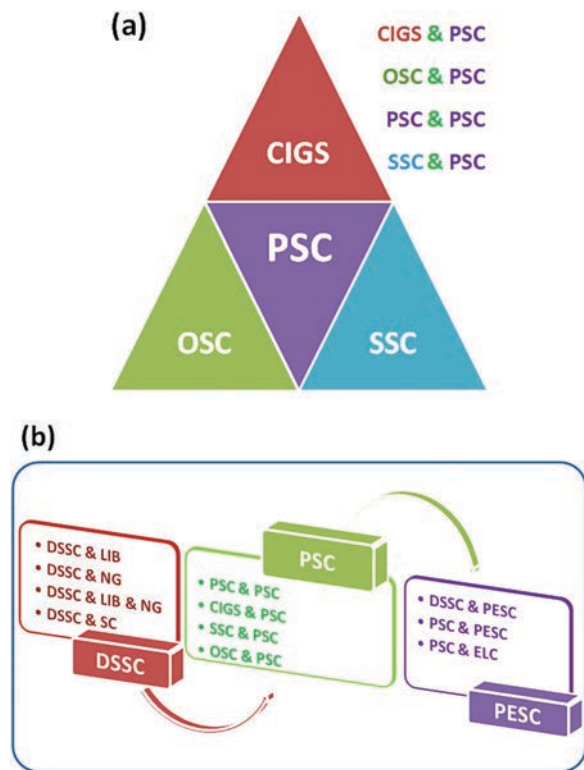


Fig. 6 (a) Integrated devices for energy harvesting and conversion based on PSCs. (b) Integrated solar cell devices for energy harvesting and storage. DSSC: dye-sensitized solar cell; PSC: perovskite solar cell; SSC: silicon solar cell; CIGS: Cu(In,Ga)(S,Se)₂; OSC: organic solar cell; PESC: photoelectrosynthetic cell; ELC: electrolysis cell.

We will, however, mainly limit ourselves to the integrated devices based on DSSCs and PSCs.

2. Integrated solar cell devices for energy harvesting and conversion

2.1. PSC/silicon tandem devices

Tandem solar cells present an exciting means for increasing the PCE of solar modules thereby reducing the balance of system cost (BOS) for PV systems and potentially the cost per watt peak (\$ per W_p) of modules if the associated added costs can be kept negligible. Tandem solar cells are fabricated such that one or more p-n junctions that employ wide-bandgap absorbers are above a p-n junction that employs a small-bandgap absorber, in order to improve the utilization of the solar spectrum and reduce the thermalization losses of photons.^{152,153} Highest efficiency tandem solar cells are based on III-V semiconductors and five-junction cells have achieved up to 38.8% efficiency under one sun.¹⁵⁴ However, the high material cost and expensive epitaxial layer growth of III-V semiconductors limit tandem devices to special markets such as concentrated PV or extra-terrestrial applications. PSCs are highly suitable for their integration in tandem devices as they exhibit wide bandgap tunability and low sub-bandgap absorption while allowing for the use of economical solution processing methods with low processing temperatures, which is indispensable for their use as top cells.^{155–159} Moreover, the lack of a liquid electrolyte in solid-state (p-i-n) PSCs allows for easier manufacturing and increased stability of integrated tandem devices as reduced emphasis has to be devoted on leaking and hermetic sealing.¹⁶⁰

The combination of large-bandgap perovskite and small-bandgap SSCs in an integrated or tandem device is a highly popular research field and widely regarded as a market entry point for the perovskite technology.^{5,161} With the leading market share of over 90% for Si modules, any improvements to the existing technology can have a major impact on the consumer market.¹⁶² The nearly ideal band gap for tandem bottom cells of 1.12 eV makes Si devices a good match in conjunction with perovskite top cells having large band gaps between 1.7–1.8 eV.^{101,163–165} While optimal top cell band gaps can be obtained by the substitution of I⁻ with Br⁻ in typical MAPbI₃ absorbers,^{166–168} increasing research is devoted to address the reported photo-induced instability of mixed halide composition.^{169–171}

Mechanically stacked, monolithic, as well as spectrally split tandem devices have been explored with various types of Si cells, device architectures, top cell band gaps, transparent contacts, and light trapping schemes. Simulations predict tandem device efficiencies over 30–35% for two-terminal^{165,171–179} and four-terminal devices^{163,171,176,177,180,181} with optimized light management, bandgap tuning, layer thicknesses, and architecture, surpassing the record for single junction c-Si at 26.6%.^{6,182} Jiang *et al.* estimated highest tandem performances for two-terminal devices, recommending the use of indium tin oxide (ITO) as top contacts as compared to graphene or thin metal layers.¹⁷⁶

Several Si cell technologies have been employed for integrated devices such as polycrystalline, monocrystalline homojunction, passivated emitter rear contact (PERC),^{183–186} heterojunction technology (HJT),¹⁸⁷ and inter-digitated back contact (IBC) cells,¹⁸⁸ and the choice has major ramifications for tandem efficiencies, device processing, and the choice of architecture.¹⁷¹ Four-terminal, mechanically stacked architectures are inherently easier to manufacture and can be readily amended to the existing Si technology.¹⁷³ Requirements for monolithic devices, such as current matching, flatness of the bottom cell, suitable contacting layers, and choice of adequate processing temperatures and reagents to allow fabrication on prior deposited films, can be omitted. Additionally, the energy yield of monolithic devices in real time operation can be affected by up to 5% by variations in spectral irradiance distribution, incident angle of light, and temperature, due to non-ideal current-matching.^{164,189} Recently, Braly *et al.* investigated the impact of phase segregating mixed halide perovskite top cells on the performance of current-matched tandem devices. Notably, the authors found that despite the induced phase segregation and the accompanied dramatic decrease in output current in the top cell, the current output of the PSC-shaded bottom cell was left unaffected, which could point to an additional advantage for four-terminal devices.¹⁹⁰

The biggest hurdle in the manufacturing of mechanically stacked tandems is the replacement of opaque contact layers in the perovskite top cell. Lang *et al.* used a flexible transfer process of a single graphene layer to fabricate up to 6.2% efficient semi-transparent PSCs, which resulted in 13.2% efficient tandem devices when stacked on HJT bottom cells. The reduced FF in the MAPbI₃ device as compared to the Au contacted cell was attributed to the high sheet resistance of graphene, which was estimated to be 350 ohm sq⁻¹.¹⁹¹ The use of a MoO_x/ITO hole transport layer (HTL) yielded a slightly reduced top cell transmittance of around 55% but enabled MAPbI₃ devices with a similar performance at 6.2% PCE and tandems up to 13.4% when combined with HJT cells.¹⁷⁸ McGehee and co-authors employed transfer-laminated Ag nanowire (NW) electrodes with 90% transmission and around 10 ohm sq⁻¹ sheet resistance to develop semitransparent MAPbI₃ top cells with up to 12.7% efficiency. These cells were mechanically stacked on both polycrystalline and monocrystalline Si cells to obtain 17.0% and 17.9% PCE, respectively.¹⁹² Transparent top cells with improved stability and efficiency of up to 12.3% were fabricated by sputtering ITO contacts on an Al-capped ZnO nanoparticle layer on PCBM ETLs. This inverted architecture was seen to exhibit an improved temperature stability as compared to opaque cells with Al/Ag contacts with a temperature coefficient as low as 0.22% per °C. In combination with 17.0% efficient mono-Si bottom cells, up to 18.0% efficient tandem devices were achieved.¹⁹³

Sputtered ITO was also used by Duong *et al.* to obtain 12.4% semi-transparent top cells with a high transmission of 80% at around 900 nm wavelength. When these cells were stacked on high performance PERC Si cells with 19.6% PCE, up to 20.1% efficient tandems could be measured.¹⁹⁴ McMeekin *et al.*

investigated larger band-gap (FA,Cs)Pb(I,Br)₃ perovskite materials for optimum band-gap matching with bottom Si cells and increased light stability and achieved stabilized 16.0% efficient opaque devices with a band gap of 1.74 eV. An ITO nanoparticle layer allowed the sputter deposition of ITO on a spiro-OMeTAD HTL for 15.1% efficient (12.5% stabilized) semi-transparent top cells. 19.2% efficient HJT bottom cells enabled up to 19.8% steady-state PCE while up to 25.2% was projected from best performing opaque devices assuming 100% transparent electrodes.¹⁹⁵ Employing thin metal layers as transparent top contacts, *i.e.* 7 nm Au on 1 nm Cu seed layer, 16.5% semi-transparent MAPbI₃ PSCs were presented by Chen *et al.* In combination with 21.2% HJT cells as bottom absorbers, 23.0% efficient tandem devices were obtained.¹⁹⁶ Ren *et al.* presented semi-transparent PSCs with a MoO₃/Au/MoO₃ multilayer stack that was evaporated on a spiro-OMeTAD HTL to achieve 18.1% efficient top cells. The combination with 19.1% efficient monocrystalline Si cells resulted in 23.6% efficient tandem devices.¹⁹⁷ Peng *et al.* introduced indium doping of state-of-the-art TiO₂ ETL layers to improve conductivity and band alignment at the ETL/perovskite interface. ITO and Au gold fingers were deposited on MoO₃ and spiro-OMeTAD HTLs to enable 16.6% stabilized PCEs for (Cs,MA,FA)Pb(I,Br)₃ devices. In combination with 24.0% highly efficient, IBC Si bottom cells,¹⁸⁸ up to 24.5% tandem devices were achieved.¹⁹⁸ Ballif and co-workers developed near-infrared (NIR) transparent MAPbI₃ perovskite top cells with transmission values over 70% between 800–1200 nm wavelength and stabilized efficiencies up to 16.4% with IO:H/ITO layers that were sputtered on MoO_x. An optical coupling liquid was used between the subcells to optically connect cells and reduce reflection losses (see Fig. 7a). Tandem efficiencies of up to 25.2% were obtained in combination with 22.1% SHJ bottom devices.^{199,200} Close to the current single junction Si record at 26.6% PCE, a recent publication by Duong *et al.* presented highest mechanically stacked, four-terminal PSC/Si tandem devices of up to 26.4% efficiency.²⁰¹ Multi-cation MA/FA/Cs/Rb perovskites with a bandgap of 1.73 eV and quartz glass substrates were used to obtain semi-transparent devices with steady state PCEs of up to 16.0% and an average transmittance of 84% between 720 and 1100 nm wavelength. Silicone gel was employed to improve the optical coupling between the perovskite top cell and the 23.9% efficient IBC Si cell bottom cell.

A few results were reported for mechanically stacked two-terminal devices. Two separate subcells are thereby individually processed and finally electrically connected by enabling a direct contact between the cell top electrodes. Matteocci *et al.* reported up to 14.5% efficient devices using a stacked ITO interlayer to connect a MAPbI₃ and HJT cell. 14.5% PCE was reported with V_{oc} of up to 1.56 V confirming good voltage addition of the subcells. However, large hysteresis of the devices was observed.²⁰² Similar devices with ITO interlayers but on monocrystalline Si bottom cells and with the addition of a thin Au layer between spiro-OMeTAD and ITO were presented by Kanda *et al.*, showing reduced hysteresis and up to 13.7% PCE.²⁰³

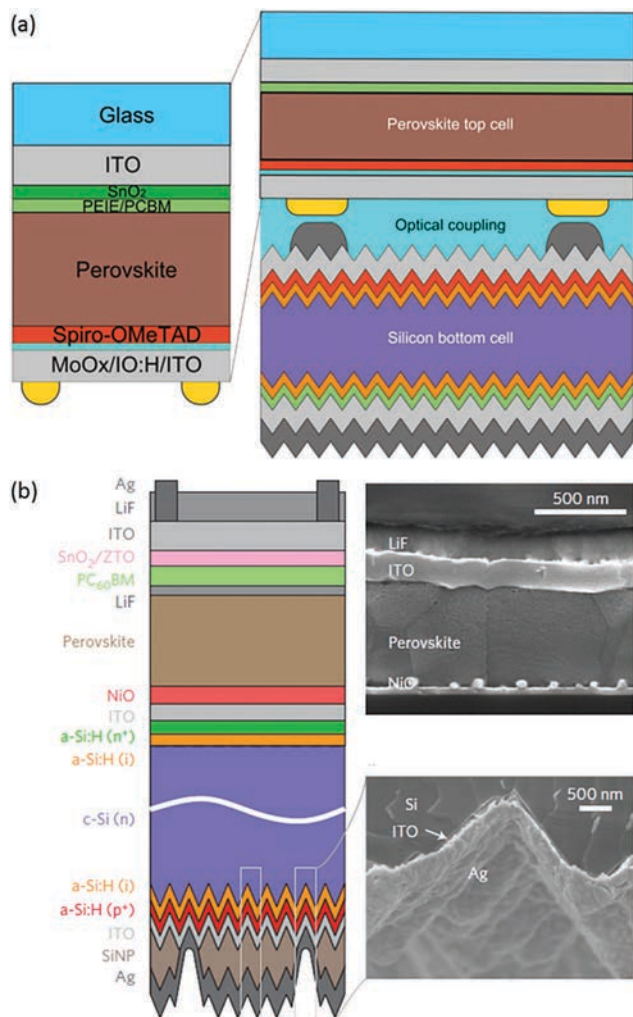


Fig. 7 (a) Four-terminal HJT Si-perovskite tandem device architecture that yielded up to 25.2% efficiency. An optical coupling liquid was used between the subcells to optically connect cells and reduce reflection losses. Reprinted with permission from ref. 200. Copyright 2016 ACS. (b) Monolithic devices on polished HJT Si substrates have achieved up to 23.6% efficiency to date. Reprinted with permission from ref. 220. Copyright 2017 Wiley-VCH.

Another means of mechanically connecting tandem devices is spectral beam splitting.^{204,205} The inherent advantage in this architecture is a higher degree of freedom in manufacturing as compared to stacked devices as the need for a semi-transparent top cell is omitted. Uzu *et al.* employed a dichroic mirror that was positioned at 45° with respect to a 25.2% efficient HJT and a 15.3% MAPbI₃ perovskite device to gain combined efficiencies of up to 28.0%.²⁰⁶ Sheng *et al.* used a similar architecture with a beam splitter to combine large-band-gap MAPbBr₃ solar cells with both multicrystalline Si and PERC devices to arrive at up to 18.8% and 23.4% efficiency, respectively.²⁰⁷ Duong *et al.* reported on a reflective tandem configuration, in which the PSC acts as a spectral filter and reflects the long wavelength light to a Si cell. In this setup, a combined efficiency of up to 23.1% was obtained using 22.4% and 15.2% efficient IBC Si and perovskite devices, respectively.²⁰⁸ A similar performing tandem device

was reported by Li *et al.* using a 16.4% efficient (FA,Cs)Pb(I,Br)₃ PSC and a 21.3% efficient PERC Si cell in a reflective tandem configuration.²⁰⁹

There are also several reports on two-terminal, monolithic tandem devices with perovskite and Si absorber layers. Reduced resistive and optical losses stemming from the omission of an additional substrate and/or charge transport layers should enable monolithic devices to reach more superior performance than mechanically stacked devices.^{173,176,178} However, the more stringent requirements on current matching, device interconnection, and consecutive processing steps add complexity to the realization of such devices. The direct deposition of perovskite top cells on Si substrates requires feasible manufacturing and high cell performance in the substrate configuration. SSCs can be fabricated with both n-type and p-type wafers leaving some flexibility on the device polarity of the top cell. The use of certain high efficiency Si technologies, however, such as HJT devices with n-type wafers or PERC cells with p-type wafers, can dictate the use of conventional or inverted cell architecture, respectively, as well as operation of the top cell in the superstrate or more commonly the substrate configuration. As highest PSC device efficiencies are typically obtained in the superstrate configuration, additional research and optimization is required to mitigate performance losses in inverted device operation. The thin layers of perovskite layers might further require a planar surface of bottom cell substrates, which can lead to increased reflection losses in the Si device.²¹⁰ Light trapping structures for high PCE Si devices receive major attention to improve the inherently weak light absorption in the NIR.^{211,212} High efficiency Si cells therefore typically employ sophisticated light trapping schemes with textured front and/or rear surfaces. Other limitations on processing can arise from temperature restrictions of the Si cell. While diffused junction silicon devices undergo diffusion and oxidation steps around 800–900 °C and should therefore be compatible with processing temperatures around 500 °C (as can be required by NiO_x or TiO₂ layers in PSCs),^{213,214} thin HJT cells might necessitate much lower temperatures below 150–200 °C to avoid performance loss due to passivation degradation and substrate warping.^{187,213–215}

Additionally, typically used ITO or indium zinc oxide (IZO) transparent conducting tin oxide (TCO) layers in HJT cells are neither electrically nor optically stable upon annealing at 500 °C in an oxygen containing environment.²¹³ With record efficiencies up to 26.3% and their use of TCO top contacts, HJT Si cells are nevertheless highly attractive and commonly used for monolithic tandem applications with perovskite top cells.^{6,182}

McGehee, Buonassisi, and co-workers reported first monolithic Si-perovskite devices with up to 13.7% stabilized efficiency by employing a Si-based n⁺/p⁺ tunnel junction between an n-type Si wafer and a perovskite top cell. The semi-transparent top cells were manufactured in the conventional architecture with high temperature processed TiO₂ layers and transparent Ag NW mesh top electrodes.^{216,217} Werner *et al.* reported increased PCEs of up to 16.4% with homojunction Si bottom cells utilizing zinc tin oxide (ZTO) as a high temperature

stable recombination layer for mesoscopic TiO₂-based perovskite top cells.^{21,3} Albrecht *et al.* employed HJT bottom cells and replaced TiO₂ ETLs with low-temperature-processed tin oxide layers by the atomic layer deposition (ALD) technique, which formed the recombination contact together with ITO. MoO₃ and ITO were used as HTLs for semi-transparent (FA,MA)Pb(I,Br)₃ perovskite devices to enable up to 19.9% efficient (18.1% stabilized) monolithic tandem solar cells.^{165,218} Werner *et al.* presented low-temperature-processed IZO films as recombination layers between HJT bottom cells and MAPbI₃ top cells. Highly transparent top cells with up to 16.4% stabilized power output were enabled by sputtering of IO:H and ITO layers on MoO_x HTLs. Monolithic two-terminal tandems from this architecture resulted in up to 21.2% and 20.5% stabilized efficiency for 0.17 cm² and 1.43 cm² large devices, respectively.^{199,219} Bush *et al.* recently presented monolithic perovskite-HJT devices with up to 23.6% certified PCE with stable power output and no hysteresis (see Fig. 7b). Encapsulated, semi-transparent (Cs,FA)Pb(I,Br)₃ cells with SnO/ZTO buffer layers and sputtered ITO exhibited up to 14.5% PCE and withstood a 1000 hour damp heat test at 85 °C and 85% relative humidity, which is the international electrotechnical commission (IEC) standard for crystalline Si modules.²²⁰

2.2. PSC/CIGS tandem devices

Chalcopyrite Cu(In,Ga)(S,Se)₂ (or CIGS) solar cells are a highly attractive technology for the incorporation into integrated or tandem devices due to their thin film nature, high PCE, and tunable bandgap. PCEs of up to 22.6% have been achieved for single junction devices, which exceeds PCEs of market leading pc-Si and all other thin film PV technologies.^{221,222} The thin film nature allows for a wide choice of deposition methods and substrates which opens the door for low-cost printing techniques, roll-to-roll deposition, and flexible tandem modules.^{223,224} The bandgap of CIGS can be tailored from 1.0 eV up to 2.4 eV by increasing the gallium and sulfur content in the absorber.²²⁵ Both highest performing devices at a band gap of 1.15 eV and lower band gap variants down to 1.0 eV are gaining increasing attention for the use as bottom cells in tandem devices with perovskite top cells.^{226,227} Simulations predict theoretical tandem PCEs of up to 42% for a combination of a 1.6–1.9 eV band-gap top cell with a 0.9–1.2 eV band-gap bottom cell, which is well accessible for perovskite and chalcopyrite absorbers, respectively.^{228–232}

Most reports on PSC/CIGS tandem devices to date have focused on the mechanically-stacked architecture. A semi-transparent perovskite solar cell is thereby stacked on top of a CIGS device to increase the utilization of the solar spectrum. The low capital investment of this method allows upgrading of existing technologies, providing a simple pathway for commercialization.¹⁹² The typically employed four-terminal configuration omits the need for sophisticated current matching *via* the bandgap, absorber thickness, or area of in-series-connected cells, which is crucial for two-terminal devices. The use of two separate substrates further reduces restrictions on processing parameters, reagents, and device architecture.

The biggest hurdle for four-terminal devices has been the fabrication of semi-transparent perovskite devices. Typically used opaque metal contacts, such as gold,^{233–236} silver,^{237–240} or aluminum,^{241,242} have to be replaced by transparent contacts. Bailie *et al.* developed a transparent contact in the form of a spray-coated Ag NW film that was transferred *via* a lamination process onto the spiro-OMeTAD layer of the perovskite cell. While this method posed a high risk of shorting or incomplete transfer, low sheet resistances (12.4 ohm sq⁻¹) and high transmission values (90%) were obtained. Due to the poor stability of mixed-halide perovskites,¹⁶⁹ semi-transparent MAPbI₃ devices with 12.7% PCE and a band-gap of 1.6 eV were stacked on 17.0% CIGS solar cells ($E_g = 1.1$ eV) to produce up to 18.6% tandem devices.¹⁹² Improved tandem PCEs of up to 19.5% were obtained by Tiwari and co-authors by using a transparent contact composed of evaporated MoO₃ and sputtered ZnO:Al to yield 12.1% semi-transparent MAPbI₃ PSCs and stacking them on 18.4% efficient CIGS bottom cells (see Fig. 8a).²⁴³ Substitution of the ZnO:Al TCO by sputtered In₂O₃:H led to 14.2% efficient PSCs and 20.5% tandem devices due to higher NIR transmission of the TCO.²⁴⁴ By moving to a substrate configuration and inverting the architecture of the PSC, up to 16.1% transparent PSCs were obtained without any additional anti-reflective (AR)-coating. Amongst others, substitution of MoO₃ with PTAA HTL resulted in over 80% transmission of the PSCs in the NIR region. The combination with 1.15 eV bandgap CIGS and 1.0 eV bandgap CuIn(S,Se)₂ (CIS) devices resulted in up to 22.1% and 20.9% efficient tandem devices. It is noteworthy that the bottom cells thereby had a stand-alone PCE of 19.2% and 13.0% for CIGS and CIS, respectively.²⁴⁵ A 20.7% efficient tandem device was recently presented by Guchhait *et al.* The group utilized a 1 nm thin Ag buffer layer together with sputtered ITO to obtain 16.0% semi-transparent MAPbI₃ devices; bottom cells exhibited a stand-alone PCE of 12.3%.²⁴⁶ First tandem modules of up to 17.8% efficiency have been reported for a mechanically stacked 3.76 cm² sized mini-module, surpassing individual module efficiencies for both subcell technologies.²⁴⁷

The thin film nature of both perovskite and chalcopyrite absorbers allows for the employment of low-cost printing methods which are expected to further reduce cost for tandem devices. Lee *et al.* have reported four-terminal tandem devices with solution-processed absorbers and electrode layers that achieved up to 10.8% PCE. CIGS absorbers with an absorption edge at 1250 nm were thereby formed from a methanol solution with polyvinyl acetate (PVA) binder that was converted with Se vapors and H₂S gas. Semi-transparent PSCs with up to 8.3% PCE were obtained using Ag NW films that were transferred onto spiro-OMeTAD. For the 8.0% efficient CIGS device, ZnO and ZnO:Al layers were spin-coated from sol-gel solutions with embedded Ag NWs to improve the conductivity.²⁴⁸ Yang *et al.* reported solution-processed tandem devices with up to 15.5% efficiency. Hydrazine solutions were employed to fabricate 12.4% efficient CIGS devices while semi-transparent PSCs with up to 11.5% PCE were obtained by thermally evaporating MoO₃/Au/Ag/MoO_x layer stacks that served as the transparent HTL.²⁴⁹

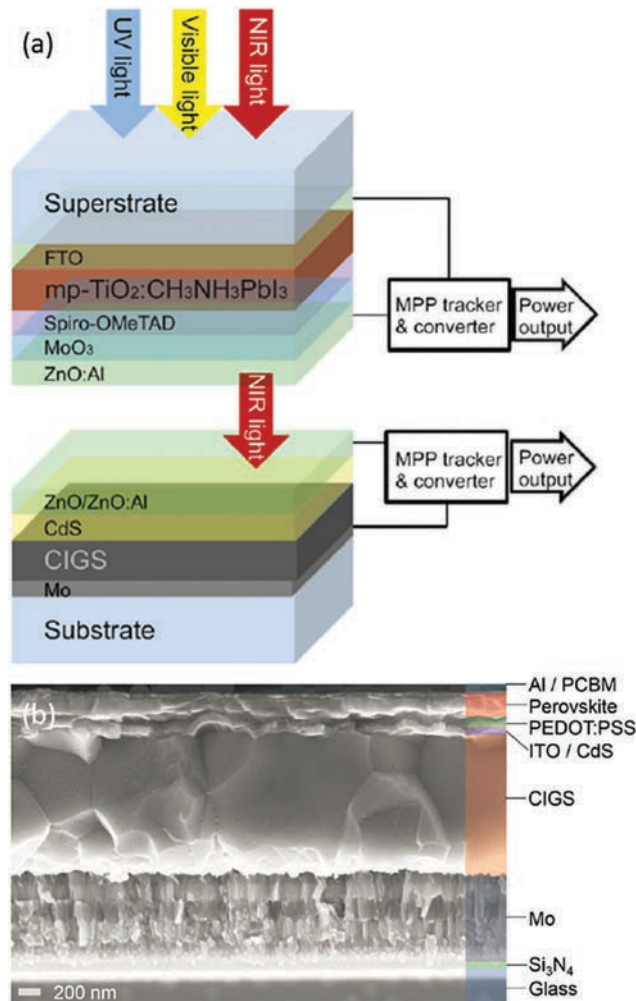


Fig. 8 (a) Four-terminal CIGS-perovskite integrated device architecture that yielded up to 19.5% efficiency. Further advancements by the same group led to up to 22.1% efficient devices. Reprinted with permission from ref. 243. Copyright 2015 ACS. (b) Solution-processed monolithic devices have achieved up to 10.9% efficiency to date. Reprinted with permission from ref. 260. Copyright 2015 Wiley-VCH.

Uhl *et al.* used a combination of spin-coated C_{60} /bis C_{60} bi-layers together with sputtered ITO as the ETL to gain semi-transparent PSCs with up to 13.6% PCE (without AR-coating). CIGS absorbers were obtained from a molecular ink with dimethyl sulfoxide (DMSO) and thiourea to yield up to 14.3% efficient CIGS and 13.0% efficient CIS devices. Mechanically-stacked tandems with various top and bottom bandgap combinations showed highest tandem stabilized efficiencies of up to 18.8% for CIGS bottom cells with $MAPbI_3$ top absorbers and up to 18.7% for CIS with $MAPbI_3$. Current-matched, two-terminal tandem devices were also projected which resulted in up to 18.5% PCE when combining low-bandgap CIS with $MAPbI_3$ absorbers, highlighting the excellent suitability of low-bandgap CIS devices for the application in monolithic bottom cells. Best current matching was thereby obtained for 1.15 eV and 1.70 eV devices as well as 1.0 eV and 1.51–1.59 eV devices. The authors also highlighted potential fill factor (FF) losses for CIS bottom

cells under UV-filtered light, which were shown to be mitigated by a slight adjustment to the sulfur content.²⁵⁰

To date, there has only been one report of monolithic tandem devices with CIGS and perovskite absorbers, which points to the increased difficulty of device manufacturing. Processing temperatures, layer compatibilities, film roughness, and device architectures have to be considered carefully. The formation of the CIGS absorber typically requires temperatures between 400–600 °C,^{223,251–253} which is incompatible with perovskite devices.^{254–256} Similarly, high temperature calcination steps that are used for typical charge transport layers in perovskite cells are incompatible with CIGS solar cells. The TiO_2 ETL and NiO_x HTL, for example, that are used for highest efficiency perovskite devices in the conventional and inverted architecture, respectively, require annealing steps around 400–550 °C for 30–60 minutes.^{136,192,234,237,241} Kijima *et al.* have shown that temperatures over 320 °C can lead to a dramatic breakdown of the CIGS device performance due to the counter-doping of the absorber by Cd or Zn diffusion from the buffer layer.²⁵⁷ Low temperature air-annealing at 200 °C is typically regarded to be harmless (or even beneficial) for CIGS devices when conducted for several minutes, while extended durations can result in cation diffusion as well.^{258,259} Todorov *et al.* found that the proximity of ZnO layers in CIGS devices can lead to deterioration of the perovskite at temperatures as low as 60 °C, while ZnO-free CIGS devices allowed annealing at 120 °C for several hours without damage.²⁶⁰ The planarization of the bottom cell might also have to be addressed due to the inherent roughness of polycrystalline CIGS absorbers.^{192,224} Lastly, the electrode polarity of CIGS devices in the substrate configuration with a bottom anode and a top cathode demands the perovskite top cells to be fabricated in substrate configuration and inverted architecture when monolithic tandem devices are desired, which can impose severe constraints on device processing and limit the electronic quality of the absorber and charge selective contacts.^{250,261} The list of practical disadvantages, however, might be offset by economic benefits from cost savings in manufacturing (*i.e.* monolithic integration and omission of an additional substrate and electrode) and improved performance (*i.e.* reduced optical and resistive losses), which can make monolithic two-terminal devices economically advantageous.^{178,224,228,232}

Todorov and co-authors have addressed these issues and reported on up to 10.9% efficient monolithic tandem devices (see Fig. 8b). Semi-transparent PSCs were developed with ETLs composed of PCBM and thin Al layers (50% transmission) or Ca-based electrodes (80% transmission), respectively. The polystyrenesulfonate doped poly(3,4-ethylenedioxythiophene) (PEDOT:PSS) was employed as a recombination layer between ITO and the perovskite. CIGS solar cells with a band gap of 1.04 eV were fabricated with a hydrazine-based solution process and covered with mixed-halide PSCs with a band gap of 1.72 eV to achieve monolithic tandem devices with up to 8.0% PCE for Al contacts and 10.9% PCE for Ca-based contacts. From single junction device performances, two-terminal PCEs of up to 15.9% were projected assuming an ideal top electrode with 100% transmission, which highlights the potential for further

improvements.²⁶⁰ Detailed optical modeling and optimization for planar CIGS/hybrid perovskite tandems claims possible PCEs as high as 29% without any antireflection (AR)-coating or light scattering structures.²⁶²

2.3. PSC/PSC tandem devices

Tandem solar cells based on two perovskite subcells are receiving increasing attention due to their high potential for achieving high performance at very low cost and energy pay-back time.^{95,263} Simulations show that PSC/PSC devices could attain efficiencies of over 35%, which would be competitive to tandems with other bottom cell technologies.²⁶⁴ The main hurdle for PSC/PSC tandems so far has been the absence of stable low-bandgap perovskite compositions. Hao *et al.* presented lead-free compositions by substituting Pb with Sn that achieved up to 5.73% PCE.²⁶⁵ It was shown that MASn(I,Br)₃ absorbers can cover a band-gap range from 2.15 eV down to 1.30 eV for pure bromide and iodide compositions, respectively. Liao *et al.* investigated (FA,MA)PbSnI₃ absorbers and achieved PCEs of up to 15.0% with a perovskite band-gap as low as 1.2 eV.²⁶⁶ Sn-based perovskites were reported to exhibit poor atmospheric stability as compared to their lead-based analog.²⁶⁵ However, several alternative low-bandgap compositions have since been explored with the addition of FA⁺, Cs⁺, Pb²⁺, and Cl⁻ that show improved performance and stability.^{263,264,266,267} Bottom cell absorbers with a band-gap of 1.2 eV are well matched with top cell absorbers with 1.75–1.85 eV and 1.6–1.9 eV in two-terminal and four-terminal architectures, respectively.²⁶³

Heo *et al.* presented mechanically-stacked PSC/PSC devices that were connected *via* a lamination technique. Wet poly(3-hexylthiophene) (P3HT) and PTAA top contact layers on MAPbI₃ devices were pressed onto the PCBM top contacts of MAPbBr₃ bottom devices to obtain two-terminal tandem cells with a V_{oc} of 2.25 V and up to 10.4% PCE.²⁶⁸ Eperon *et al.* reported remarkable four-terminal devices of up to 20.3% efficiency (see Fig. 9). In this work, (FA,Cs)(Sn,Pb)(I,Br)₃-based absorbers allowed bandgap tailoring and improved device stability. Bottom devices with 1.2 eV bandgap and up to 14.8% efficiency were combined with semi-transparent top cells of 1.6 eV bandgap and 15.8% efficiency to reach the highest efficiency tandems.²⁶³

Jiang *et al.* were the first to report on bottom up, solution-processed, two-terminal tandem devices. A multilayer of spiro-OMeTAD/PEDOT:PSS/PEI/PCBM:PEI (poly(ethyleneimine) is abbreviated to PEI) was thereby employed as a charge recombination layer. Monolithic tandem devices in the substrate configuration exhibited up to 1.89 V, but PCE (7.0%) and short circuit current density (J_{sc}) values were limited due to the use of two equal band-gap MAPbI₃ absorber layers with non-complementary absorption spectra.²⁶⁹ Eperon *et al.* combined 1.2 eV (FA,Cs)(Pb,Sn)I₃ bottom cell absorbers and 1.8 eV (FA,Cs)(Pb,Sn)(I,Br)₃ top cell absorbers to gain monolithic tandem efficiencies of up to 17.0% (see Fig. 9). It was seen that the top ITO contact of the bottom devices acted as a protection layer to avoid solvent damage from consecutive layer processing. Forgacs *et al.* deposited 1.55 eV MAPbI₃ bottom cells on 2.0 eV band-gap (FA,Cs)Pb(I,Br)₃ top cells.

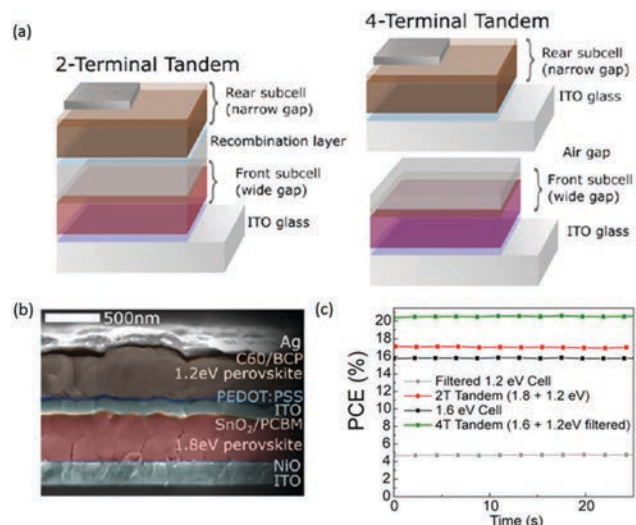


Fig. 9 (a) Two and four terminal tandem configuration that yielded up to 17.0% and 20.3% PCEs. (b) SEM micrograph of the two-terminal perovskite tandem device with 1.2 eV and 1.8 eV band-gap subcells. (c) Stabilized power output of the two- and four-terminal tandems and subcells. Reprinted with permission from ref. 263. Copyright 2016 AAAS.

Monolithic tandems in the superstrate configuration achieved up to 18.1% PCE in reverse scan (17.4% in forward scan) using small molecular weight organic semiconductors as selective charge transporting layers. Notably, all layers were vacuum evaporated, except for the wide-bandgap perovskite and the TiO₂ ETL.²⁷⁰

2.4. PSC/organic solar cell (OSC) tandem devices

Usually, solar radiation below a wavelength of about 800 nm can be utilized in most state-of-the-art PSCs with MAPbI₃ or FAPbI₃ whereas the majority of the NIR range cannot be efficiently used, which hinders the efficient harvest of photons and further advance in PCE. Therefore, one promising way to improve the cell's performance is to broaden the light absorption of the perovskite layer to the NIR spectral region (higher than 800 nm). Very successfully, the photo-response of hybrid halide perovskites as light harvesters for PSCs has been pushed to 950 nm (MASnI₃) and 1060 nm (MASn_{0.5}Pb_{0.5}I₃) by replacing Pb with Sn. However, the corresponding PCE (5.73% and 4.18%) and open circuit voltage (V_{oc}) (0.82 V and 0.42 V) of the MASn_xPb_{1-x}I₃ PSC with poor stability were much lower as compared with the typical MAPbI₃ PSC.^{265,271} Another alternative strategy is to broaden the light absorption to the NIR spectral region by integrating PSCs with other solar cells to enhance the PV performance of PSCs. As we reviewed above, the overwhelming majority of work has focused on integrating PSC with CIGS or SSCs. Here, we will highlight another type of integrated devices based on PSCs and OSCs.

The integration of PSCs and OSCs into one unit means to integrate both a perovskite and a bulk-heterojunction (BHJ) in an interlayer-free tandem cell. More exactly, some examples cannot be regarded as an integrated system; it is just the modification of PSCs. The BHJ is a photoactive layer composed of a NIR absorbing conjugated polymer and small molecule or a

fullerene derivative usually used as light absorbers in OSCs that have exhibited superior PV performance. The electrons and holes produced in perovskite films and BHJ films can be collected at each electrode based on their ambipolar charge transporting properties. It is highly desirable for capturing full-range solar light from ultraviolet-visible (UV-vis) to NIR solar spectrum by integrating a perovskite layer as a UV-vis absorber and a BHJ layer as a NIR absorber in an interlayer-free tandem cell. The PCE value of the as-fabricated integrated device can be expected to increase to the one approaching the Shockley–Queisser limit.^{272,273}

Until now, there have been several interesting reports that investigated integrated PSC/OSC devices, and their performances, including FF, J_{sc} , photo-response, and NIR harvesting, which are greatly improved by the integration pattern.^{274–278} These innovative designs present huge potential to achieve high PCEs in the development of new-generation PV technologies. Poly(diketopyrrolopyrrole-terthiophene) (PDPP3T) is a typical low-bandgap polymer with an optical bandgap of 1.33 eV, lower than that of MAPbI₃ (approximately 1.55 eV).^{67,279} Integrating PDPP3T into a PSC forms a structure of ITO/PEDOT:PSS/MAPbI₃/(PDPP3T-PC₆₁BM)/Ca/Al (PC₆₁BM stands for [6,6]-phenyl-C₆₁-butyric acid methyl ester), as illustrated in Fig. 10a, in which both perovskite and PDPP3T serve as the light absorber. The bilayer absorber film can efficiently enhance the light absorption of the

integrated cells, resulting in an expanded photo-response of the integrated cell to 970 nm, higher than that of the single BHJ cell or single PSC. The external quantum efficiency (EQE) spectrum (Fig. 10b) of the integrated cell in the 300–755 nm section mainly stems from the PSC due to the strong absorption of MAPbI₃ in that region while beyond 755 nm it mostly comes from the BHJ cell. Although the photo-response of the integrated cell has been greatly broadened, the average PCE (6.63%), FF (0.60) and V_{oc} (0.86 V) values of the integrated cell have not achieved an evident increase as compared with the single PSC (9.46%, 0.80, and 0.90 V) (Fig. 10c).²⁷⁴

Through introducing a wide-band gap, small-molecule DOR3T-TBDT as a donor into the BHJ film, and integrating perovskite with BHJ together, Y. Yang's group developed an integrated perovskite/BHJ device with a structure of ITO/TiO₂/perovskite/BHJ/MoO₃/Ag, as illustrated in Fig. 11a and b.²⁷⁶ This improved planar structure is an interlayer-free parallel tandem solar cell based on both PSC and OSC subcells for efficient light harvesting. The MAPbI_{3-x}Cl_x perovskite layer absorbs UV-vis light while the DOR3T-TBDT/PC₇₁BM or PBDTT-SeDPP/PC₇₁BM (PC₇₁BM stands for [6,6]-phenyl-C₇₁-butyric acid methyl ester) BHJ layer absorbs the light that has not been fully absorbed by the perovskite or NIR light. The efficient integrated PSC/OSC device using the PBDTT-SeDPP/PC₇₁BM BHJ film achieves a higher PCE (12%) and a higher

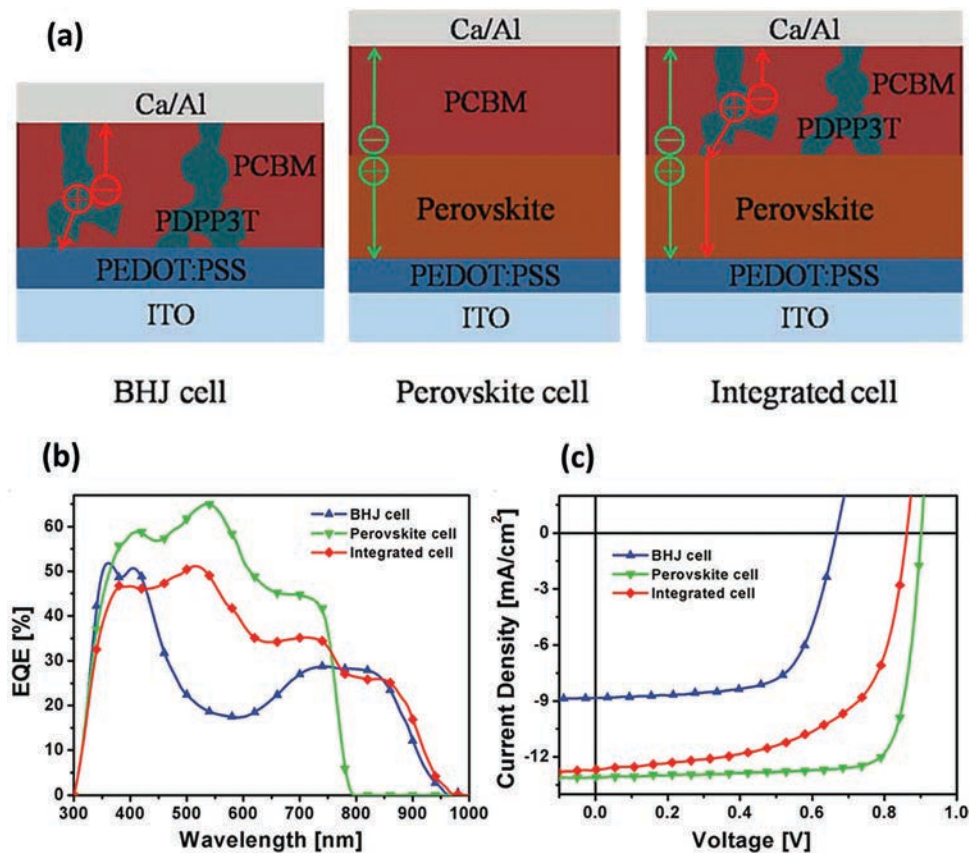


Fig. 10 Structures (a), EQE spectra (b), and $J-V$ curves (c) for the OSC (BHJ solar cell), PSC and the integrated PSC/BHJ cell. Reproduced with permission from ref. 274. Copyright 2015 RSC.

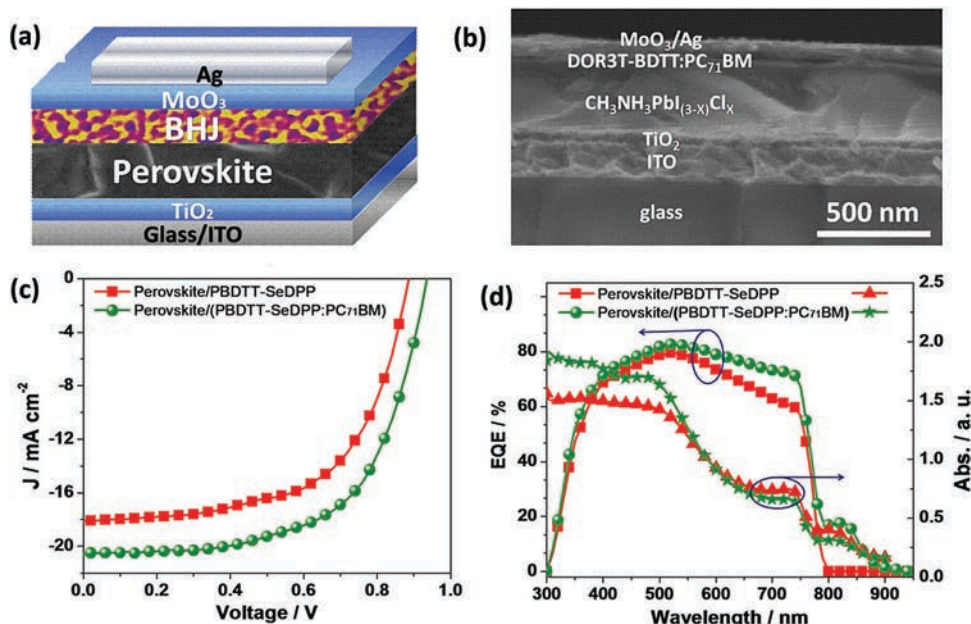


Fig. 11 (a) Schematic structure and (b) cross-sectional SEM image of the integrated PSC/OSC device. (c) J - V curves of the integrated PSC/OSC(perovskite/BHJ) device. (d) EQE spectra of the corresponding PV device and absorption spectra of the HTL (PBDTT-SeDPP) and BHJ (PBDTT-SeDPP/PC₇₁BM) film. Reproduced with permission from ref. 276. Copyright 2015 ACS.

J_{sc} (20.6 mA cm⁻²), compared with a PSC using PBDTT-SeDPP alone (9.7%, 18.1 mA cm⁻²) (Fig. 11c). The EQE data confirms that the photo-response of the integrated perovskite/BHJ device with a structure of ITO/TiO₂/MAPbI_{3-x}Cl_x/PBDTT-SeDPP/PC₇₁BM/MoO₃/Ag is extended to 900 nm whereas that of the PSC shows no photo-response higher than 800 nm (Fig. 11d). The extension to 900 nm can be attributed to the contribution of PBDTT-SeDPP which exhibits high light absorption in the UV-vis-NIR region. However, it should be noted that the neat small molecule or polymer HTM cannot contribute to the photocurrent whereas the PBDTT-SeDPP blended with PC₇₁BM acceptor in BHJ forming an integrated device structure with perovskite will generate higher photocurrent and higher PCE.

A full-range absorbing integrated solar cell composed of UV-vis absorbing MAPbI₃ perovskite layer and an NIR absorbing organic BHJ was recently developed by Lee and co-authors.²⁷⁷ As shown in Fig. 12a-c, the BHJ is composed of a diketopyrrolopyrrole (DPP)-based low-bandgap polymer DT-PDPP2T-TT, PC₇₁BM and N2200 (poly[*N,N'*-bis(2-octyl)dodecyl]-naphthalene-1,4,5,8-bis(dicarboximide)-2,6-diyl]-*alt*-5,5'-(2,2'-bithiophene) is abbreviated as N2200). Thereby, the DT-PDPP2T-TT acts as a donor whereas PC₇₁BM and N2200 serve as acceptors. The integrated device was fabricated based on a planar architecture with a structure of ITO/PEDOT:PSS/VO_x/MAPb(I_{1-x}Br_x)₃/BHJ/N-doped TiO_x/Al, where the PEDOT:PSS/VO_x layers are the hole transport/collection layers. A nitrogen-doped TiO_x layer was used to enhance the electron selectivity and decrease the contact resistance between the BHJ film and the Al electrode. By introducing a novel n-type polymer N2200 as an electron transport enhancer and diphenyl ether (DPE) as a solvent processing additive, the BHJ morphology was optimized.

The optimized integrated perovskite/BHJ devices generate a dramatically increased J_{sc} from 17.61 to 20.04 mA cm⁻² because of the additional NIR harvesting, retaining a higher FF of 0.77 and a V_{oc} of 1.06 V. As a result, a PCE of 16.36% was achieved in the integrated device based on PSC and OSC. This PCE value is so far the highest value for the reported integrated perovskite/BHJ devices, which is far higher than that value using the optimized reference PSCs (14.70%). In addition, a low-temperature-processable flexible integrated perovskite/BHJ device was also fabricated. Polyethylene terephthalate (PET)/ITO thereby served as flexible substrates. All of the processes were performed below 150 °C, and a PCE of 12.98% was achieved in the optimized flexible integrated perovskite/BHJ device (Fig. 12d).

Compared with the previous integrated PSC/OSC devices by Ding's group and Yang's group,^{274,276} Lee's group used the low-bandgap polymer DT-PDPP2T-TT to absorb NIR radiation up to 920 nm that is above the absorption edge of the perovskite (800 nm). Importantly, the optimized BHJ layers in Lee's work effectively provided additional light harvesting in the NIR without sacrificing V_{oc} and FF of the PSCs.²⁷⁷ Similarly, an extended PV response up to 900 nm has been demonstrated by Sun's group in the integrated perovskite/BHJ device with a structure of FTO/c-TiO₂/m-TiO₂/(FAPbI₃)_{0.85}(MAPbBr₃)_{0.15}/BHJ/V₂O₅/Au using a small molecule/PC₇₁BM BHJ layer. Through careful interface engineering, the (FAPbI₃)_{0.85}(MAPbBr₃)_{0.15}/HTM/PC₇₀BM (PC₇₀BM stands for [6,6]-phenyl-C₇₀-butyric acid methyl ester) integrated devices showed an optimized PCE of 16.2%.²⁷⁸ Sun group's work is based on the narrow band-gap acceptor-donor-acceptor (A-D-A) type small molecule HTM and PC₇₀BM as the BHJ layer in the PSC/OSC integrated device,

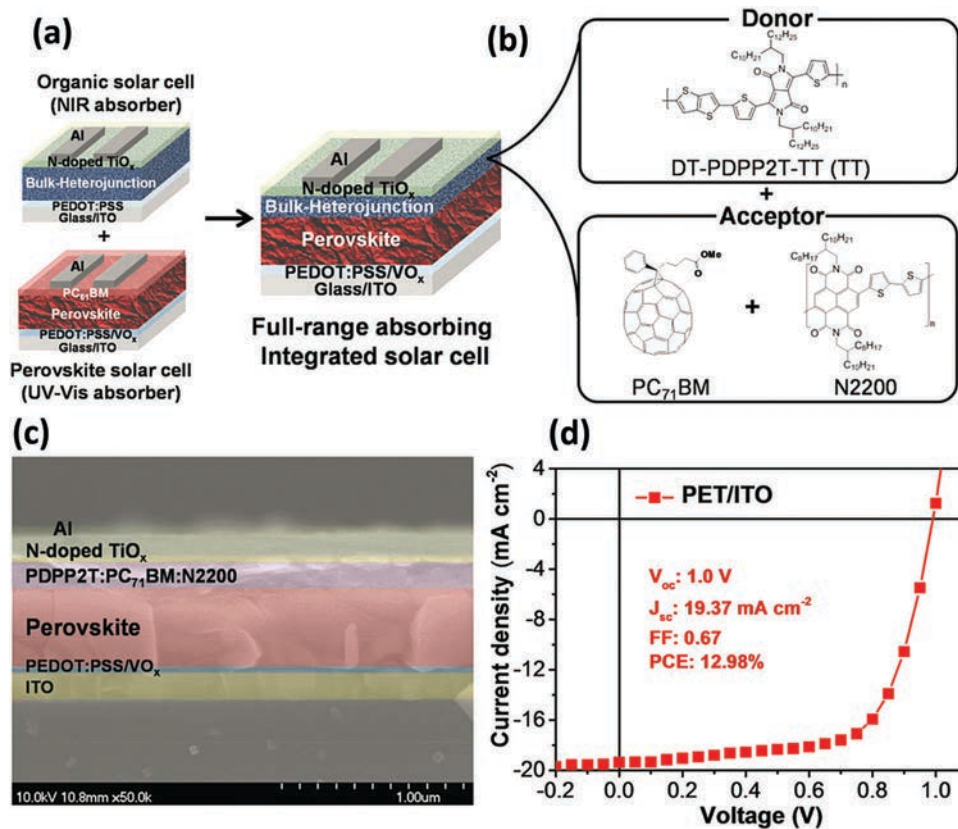


Fig. 12 (a) Device architecture of the integrated PSC/OSC device. (b) Chemical structures of DT-PDPP2T-TT, PC₇₁BM, and N2200. (c) Cross-sectional SEM image of the integrated PSC/OSC device. (d) *J*-*V* curve of a flexible integrated PSC/OSC device. Reproduced with permission from ref. 277. Copyright 2016 Wiley-VCH.

generating an improved photo-response. Note that the photo-response of the PSC/OSC integrated device with an architecture of ITO/PEDOT:PSS/MAPbI₃/PC₆₁BM/C₆₀-SB/Ag/MoO₃/Polymer BHJ/C₆₀-N/Ag (C₆₀-SB stands for tris(sulfobetaine)-substituted fulleropyrrolidine, and C₆₀-N stands for tertiary amino-fulleropyrrolidine) is not broadened even though a PCE of 16%, including a maximum V_{oc} of 1.80 V and a maximum FF of 0.77, has been achieved, which can be attributed to an efficient graded recombination layer.²⁷⁵

It is clear from the above-mentioned results that the integration of a UV-vis absorbing PSC layer with a NIR absorbing BHJ layer into a tandem solar cell is an effective strategy for extending the absorption bandwidth of the perovskite, thus advancing the PCE of the integrated PSC-based devices. Those results show the feasibility and potential for integrated devices to improve cell efficiency, meanwhile, provides significant design principles for this novel PV architecture. It should be stressed again that, in terms of the commercialization of solar cells, the development of the integrated PSC/OSC device has three advantages: one is the achievement of high PCEs by broadening absorption to the NIR region; the second is the reduction of the thermalization losses resulting from the current and/or voltage mismatch among subcells; and the third is that it is much easier to manufacture the device by monolithically stacking the perovskite layer and the BHJ layer. These advantages

for such an interlayer-free parallel tandem cell are among others similar to integrated devices for energy harvesting and storage, which is discussed in the next section.

3. Integrated solar cell devices for energy harvesting and storage

3.1. DSSC and LIB integrated devices

Solar cells are devices to convert sunlight into electricity (energy harvesting), while LIBs can convert electricity into chemical energy (energy storage). The fabrication of an integrated power system that hybridizes energy harvesting and storage, such as solar cells and LIBs, is a growing field of research and especially important for mobile electronics, as the supply of electric energy can be bridged over the intermittent periods of light harvesting. Typically, these energy harvesting and storage devices are developed as independent technologies but ultimately combined by the user to create a power system. Traditionally, this system is based on commercial silicon-based solar panels and solid-state LIBs, and with both independent parts usually being rather large, heavy, and inflexible. In order to satisfy the special needs in some fields such as mobile electronics, integrated power packs with properties such as small size, light-weight, and high energy density have to be developed. In particular,

with advancements in nanomaterial science and technology, various nanostructures have been developed and widely applied in energy harvesting, conversion, and storage devices due to their superior efficiency and reduced weight.

Guo *et al.* demonstrated the successful fabrication of an integrated power pack consisting of tandem DSSCs and a LIB on the same Ti foil that employed double-sided TiO₂ nanotube (NT) arrays.¹³³ As illustrated in Fig. 13, the upper part used solar cells based on TiO₂ NTs, while the lower part is a LIB for storing the generated energy by the DSSCs, utilizing TiO₂ NTs as the anode and LiCoO₂ as the cathode. When sunlight is irradiated on the DSSCs, the photo-generated electrons will be injected into the conduction band of TiO₂ NTs from dye molecules and transported along the Ti foil to the TiO₂ anode of the LIB, while the photo-generated holes accumulate at the Pt electrode. Thus, the LIB is in a charging process during which the electrons produced by DSSCs will promote the anode reaction of $\text{TiO}_2 + x\text{Li}^+ + xe^- \rightarrow \text{Li}_x\text{TiO}_2$. Simultaneously, the cathode reaction of $\text{LiCoO}_2 \rightarrow \text{Li}_{1-x}\text{CoO}_2 + x\text{Li}^+ + xe^-$ releases free electrons, which will flow to the Pt CE of the DSSC through an external circuit and combine with the holes there. Thus the entire process for charge generation, separation, and storage is complete. In order to provide a high enough voltage for charging the LIB with the solar cells, tandem solar cells are needed. An open-circuit voltage of 3.39 V and a short-circuit current density of 1.01 mA cm⁻² have been reached, and the power pack can be charged to about 3 V in around 8 min, exhibiting a discharge capacity of about 38.89 $\mu\text{A h}$ under the discharge density of 100 μA . However, the total energy conversion and storage efficiency for this system is still very low (only 0.82%) and further improvements are needed, especially with respect to the conversion efficiency of DSSCs, the energy density of LIBs, as well as the integration mode design.

As promising alternatives for conventional lithium ion batteries, lithium–oxygen (Li–O₂) and lithium–sulfur (Li–S) batteries have recently received considerable attention owing

to their high specific energy density.^{282,283} The latter provide a new platform for developing integrated devices *via* photocharging to directly convert solar to electrochemical energy.^{282–284} In Li–O₂ batteries, charge is stored at the cathode by the reversible formation/decomposition of Li₂O₂ on discharge/charge.²⁸⁴ However, the insulating Li₂O₂ and the sluggish kinetics of the Li₂O₂ oxidation reaction hinder the efficient electrochemical decomposition of Li₂O₂, which leads to a severe charging overpotential issue. Wu *et al.* proposed a new concept of a “photoassisted charging process” by integrating a triiodide/iodide redox-coupled dye-sensitized TiO₂ photoelectrode with a Li–O₂ battery.²⁸⁰ As shown in Fig. 14a–c, upon charging under illumination, the reduced form of the redox shuttle (M^{red}) is first converted to M^{ox} on the oxygen electrode, which in turn oxidizes the Li₂O₂. Owing to the generation of photovoltage and the efficiently shuttling charges between Li₂O₂ particles and the oxygen electrode surface, the oxidation of Li₂O₂ is facilitated and the charging overpotential is greatly reduced. More importantly, the use of a redox shuttle to couple a photoelectrode and an oxygen electrode offers a unique strategy to address the overpotential issue of non-aqueous Li–O₂ batteries and also a distinct approach for integrating solar cells and batteries.

In Li–S batteries, charge is stored at the S cathode by the reversible formation/decomposition of Li₂S on discharge/charge. However, the reduction of S into the final Li₂S product is accompanied by a series of intermediate species: Li₂S_x ($2 \leq x \leq 8$) and insulating S.²⁸⁵ Note that the sulfide/polysulfide electrolytes are widely used in quantum dot solar cells (QDSCs), and the S²⁻/S_n²⁻ redox species are able to strongly adsorb at the metal chalcogenide quantum dot surface, which can efficiently scavenge holes from quantum dots.²⁸⁶ As a consequence, Zhou *et al.* designed a new prototype of a solar-driven chargeable Li–S battery, in which the capture and storage of solar energy was realized by oxidizing S²⁻ ions to polysulfide ions in aqueous solution with a Pt-modified CdS photocatalyst, whose working principle is as shown in Fig. 14d and e.²⁸¹ This device delivered a specific capacity of 792 mA h g⁻¹ during the 2 h photocharging process with a discharge potential at 2.53 V (vs. Li⁺/Li). Moreover, the charging process could proceed under natural sunlight irradiation. The developed device realized the direct storage of solar energy in a Li–S battery without using PV cells while also being accompanied by hydrogen generation.

3.2. DSSC, SSC, and NG integrated devices

Harvesting solar energy *via* solar cells is an important way to respond to the energy crisis and environmental pollution. However, in some circumstances, such as a cloudy day or for indoor applications, solar energy may be very weak or even impossible to access. In contrast to this, mechanical energy is ubiquitous. Taking advantage of a solar cell and a NG to form a hybrid cell is a promising way for energy harvesting. In 2009, Xu *et al.* developed a hybrid cell composed of a piezoelectric nanogenerator (PENG) and a DSSC on a common substrate as shown in Fig. 15a–c.²⁸⁷ As for the PENG, a ZnO vertical NW array was grown on a GaN substrate by the vapor deposition

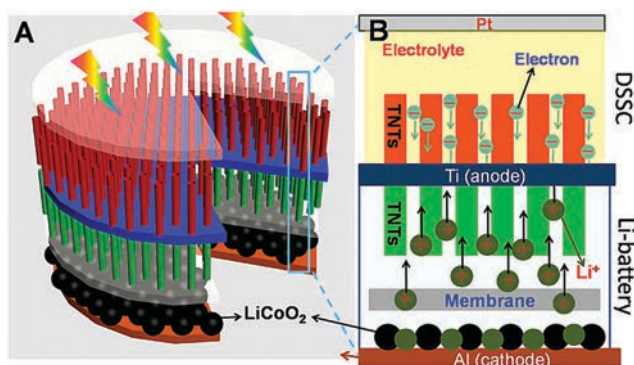


Fig. 13 Design and principle of an integrated power pack system based on double-sided TiO₂ NT arrays. (A) TiO₂ NT arrays grown on the Ti foil substrate by anodization in fluoric ethylene glycol solution. The top segments of the Ti foil are tandem DSSCs which are utilized to harvest sunlight from the environment, and the bottom segment is a typical LIB which is used to store energy converted from DSSCs. (B) Detailed structure and working principle of the integrated power pack system. Reprinted with permission from ref. 133. Copyright 2012 ACS.

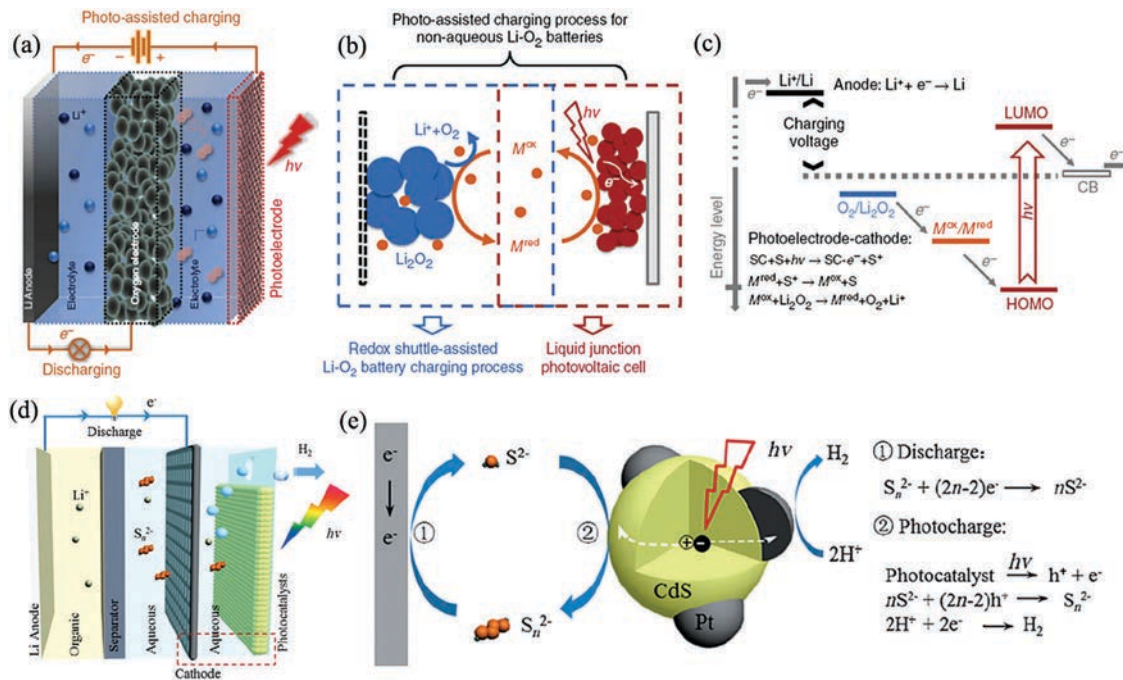


Fig. 14 (upper row) The photoassisted charging process of a solar battery. (a) Schematic drawing of a three-electrode solar battery consisting of a Li anode, an oxygen electrode and a photoelectrode. On charging, the photoelectrode and Li anode are connected to the outside circuit, while on discharging, the oxygen electrode and Li anode are connected to the outside circuit. (b) The proposed photoelectrochemical mechanism of the photoassisted charging process: on charging under illumination, the redox shuttle (M^{red}) is oxidized to M^{ox} on the photoelectrode and then diffuses to the Li_2O_2 particles that are deposited on the oxygen electrode. By oxidizing the Li_2O_2 to O_2 and Li^+ , the M^{ox} is reduced back to M^{red} . (c) Corresponding energy diagram of a solar battery ('SC' stands for semiconductor and 'S' stands for sensitizer). The photoassisted charging voltage is determined by the energy difference between the Li^+/Li redox potential and the quasi-Fermi level of electrons in the semiconductor electrode (at best close to its conduction band (CB) edge). Reprinted with permission from ref. 280. Copyright 2014 NPG. (lower row) (d) In a different setup, the battery consists of a Li anode with an organic electrolyte, a Li-ion conductive LTP ($\text{Li}_{1.35}\text{Ti}_{1.75}\text{Al}_{0.25}\text{P}_{2.7}\text{Si}_{0.3}\text{O}_{12}$) glass ceramic separator, and an aqueous Li_2S_n ($1 \leq n \leq 4$) alkaline catholyte containing the Pt/CdS photocatalysts (coated on Ti mesh). (e) The discharging process is the same as that of a common aqueous Li-S battery while the charging process is different: The discharged S^{2-} ions are oxidized to polysulfide ions by photoexcited holes from the CdS photocatalyst driven by light irradiation. Meanwhile the photoexcited electron, freed from the Coulomb attraction of the hole, transfers to the Pt particle, where it then reduces protons to hydrogen. Reprinted with permission from ref. 281. Copyright 2015 Wiley-VCH.

process as the working component, while the ZnO continuous film deposited simultaneously with the ZnO NW array was used as the bottom electrode. A Pt-coated silicon substrate, with one side possessing the zig zag structure, was used as the top electrode of the PENG. The flat side of the silicon was used as the cathode of the DSSC. The ITO substrate acted as the anode of the DSSC while the dye-decorated ZnO NW array was used as the working component. This hybrid cell can harvest the solar energy and ultrasonic wave energy simultaneously or individually. By integrating these two cells in series or parallel, the hybrid cell can either enhance the output voltage from 0.591 V to 0.60 V or output current from $44 \mu\text{A cm}^{-2}$ to $45 \mu\text{A cm}^{-2}$. However, the utilization of a liquid electrolyte may cause the DSSC to suffer from evaporation and leakage as the back to back physical integration of these two cells on the same substrate was not a compact design. In order to solve these problems, Xu *et al.* developed a solid-electrolyte-based compact hybrid cell as shown in Fig. 15d.²⁸⁸ The ZnO NWs are grown *via* the hydrothermal method on the ITO substrate. After the dye was decorated on the ZnO NWs, the solid electrolyte was spun on the dye sensitized ZnO NWs followed by a baking procedure to remove the organic solution in the electrolyte. After depositing

a layer of Au, a cone-shaped cathode, which can also be used as the top electrode of the PENG, was prepared. By stacking a GaN substrate with a ZnO NW array onto the DSSC, a compact teeth-teeth hybrid cell was fabricated. After incorporating the PENG into the device, the cell's optimum power could be enhanced by 6%. In order to harvest solar energy for remote locations, Pan *et al.* developed an optical fiber based hybrid cell as shown in Fig. 16.²⁸⁹ The ITO layer and ZnO seed layer were deposited on the optical fiber in sequence. After growing the ZnO NW array on it, the fiber was placed in a Pt-coated stainless steel capillary tube. The liquid electrolyte was introduced between the tube and the optic fiber *via* a capillary effect. ITO and Pt functioned as the photoanode and photocathode, respectively. On the outer side of the stainless steel tube, a densely packed ZnO NW textured film was fabricated by a wet chemical method while on top of it a conductive carbon tape was used as the electrode of the PENG. The hybrid cell's voltage was dominated by the PENG while its current was dominated by the DSSC which benefited the power output of the hybrid cell. With the development of wearable electronics, the development of lightweight, flexible, and sustainable power sources is highly desirable. Pu *et al.* developed a wearable power textile by

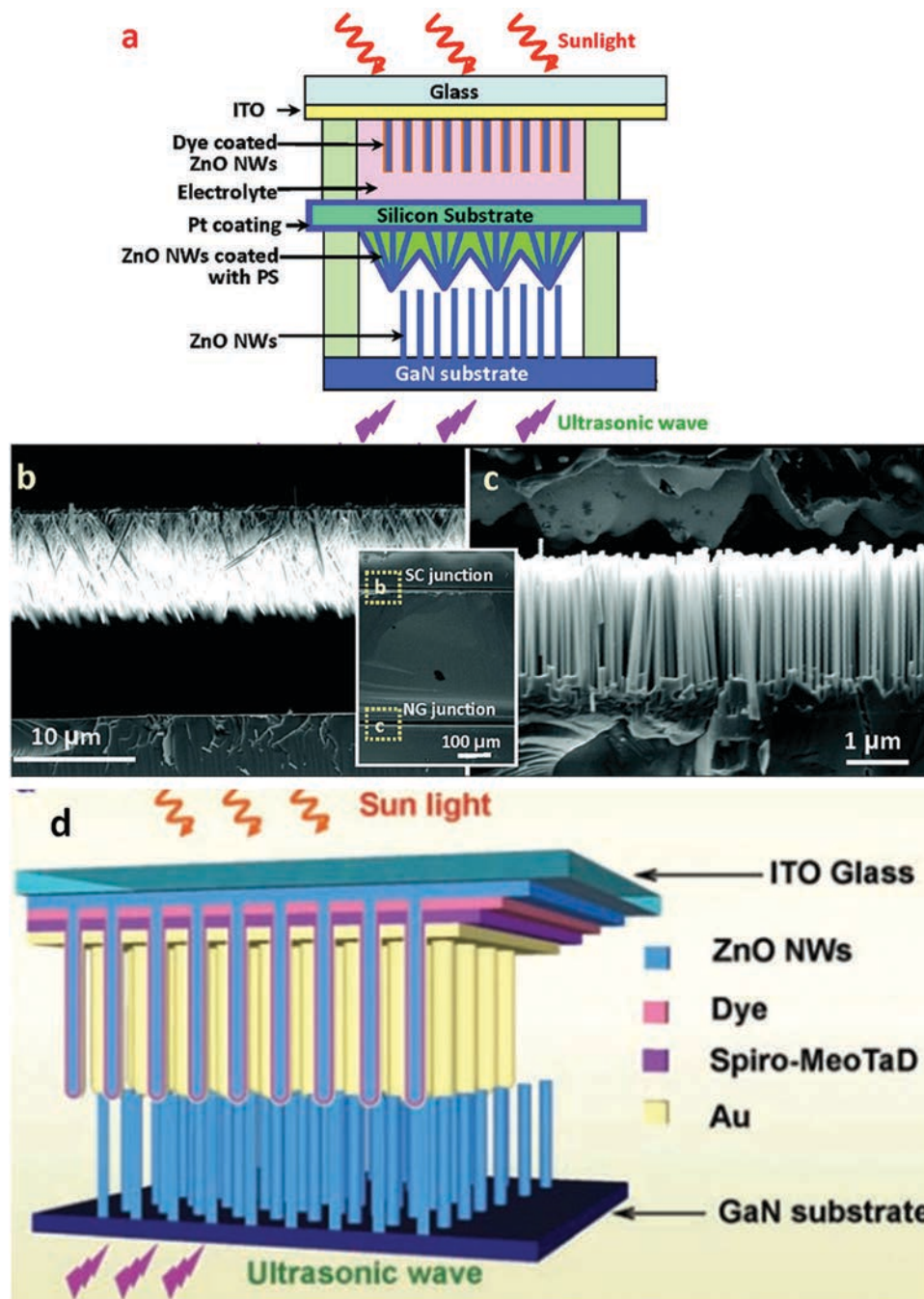


Fig. 15 (a) Schematic structure of a serially integrated hybrid cell. (b) SEM image of the DSSC unit. (c) SEM image of the PENG unit. The SEM image inserted between (b) and (c) is a low-magnification cross-section view of the hybrid cell. Reproduced with permission from ref. 287. Copyright 2009 ACS. (d) Schematic illustration of a hybrid cell consisting of a solid-state DSSC and a vertically aligned ZnO NW array grown on a GaN substrate using the high-temperature vapor deposition method for fabricating the PENG. Reproduced with permission from ref. 288. Copyright 2011 Wiley-VCH.

integrating a grating-structured textile-based triboelectric nanogenerator (TENG) and a fiber-based DSSC into a cloth as shown in Fig. 17a.²⁹⁰ The TENG, aimed to harvest the swing energy of arms during walking and running, was made up of a slider fabric located at the sleeve and a stator fabric located underneath the arm (Fig. 17b). Both interdigitated electrodes on the stator and parallel striped electrode on the slider were

fabricated by a route of laser-scribed masking and subsequent electroless deposition. For the stator fabrics, an additional layer of parylene used as an electrification layer was deposited on the top of Ni *via* chemical vapor deposition. The relative sliding between the slider and stator fabric can generate alternative electricity between the interdigitated electrodes in the stator fabric. The fiber-based DSSC was fabricated by winding the Pt

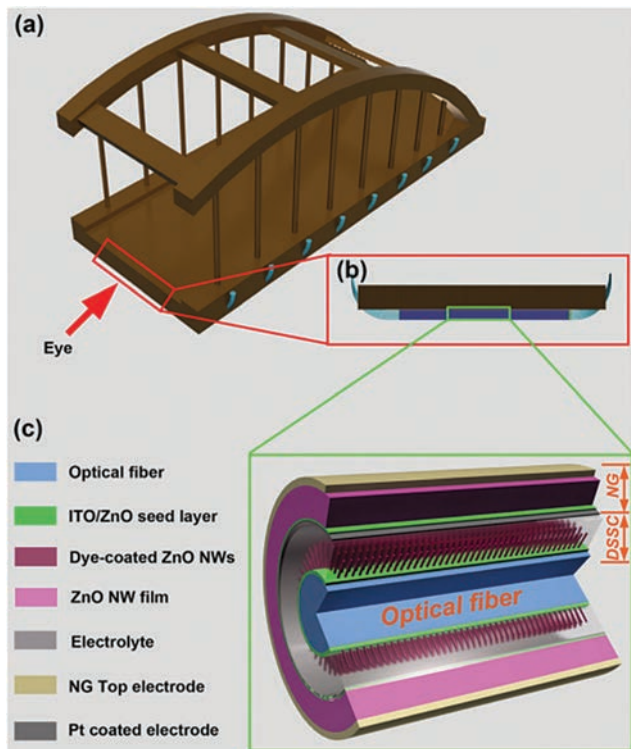


Fig. 16 (a) A demonstration of using the hybrid cell beneath a bridge. (b) Enlarged view of the hybrid cells mounted beneath the bridge. (c) The 3D HC is composed of an optical fiber-based DSSC with a capillary tube as the counter electrode. Reproduced with permission from ref. 289. Copyright 2012 Wiley-VCH.

wire around the TiO_2 coated Ti wires in a flexible plastic tube (Fig. 17c). After combining the TENG and DSSC *via* a bridge rectifier (Fig. 17d), the hybrid power textile can generate an additional short circuit current as shown in Fig. 17e. Chen *et al.* developed a compact hybrid textile composed of a TENG and DSSC.²⁹¹ In this design, Cu-coated polymer polytetrafluoroethylene (PTFE) stripes, and a wire-shaped photoanode were woven on an industrial weaving machine to form the hybrid cell *via* a shuttle-flying process. By this hybridization, next to the enhanced output power, the load range can be tailored, which is useful for powering small electronics with varying resistance.

Abide by the DSSC/NG integrated device, Wang *et al.* developed a hybrid integrated device based on a silicon solar cell (SSC) and a NG in 2016 that was designed for simultaneously or individually harvesting solar and wind energy.²⁹² The structure of the hybrid NG is shown in Fig. 18a. A Si-based solar cell was fixed on the top surface of a TENG. The TENG was composed of a middle vibrating Kapton/Cu/FEP film, top and bottom acrylic substrates with Cu electrodes. The TENG's operation was based on the middle film's periodic contact and separation with the top/bottom electrodes under the wind. The solar cell reached its optimal output power of 8 mW under an external resistance of 600 Ω , while the TENG achieved its optimal output power of 26 mW under an external resistance of 1 M Ω . After solving this

impedance mismatch problem *via* a transformer, the hybridized NG exceeded the output current of the individual solar cell or TENG, as shown in Fig. 18b. Finally, four hybrid NGs were integrated together to power a temperature–humidity sensor, as shown in Fig. 18c.

3.3. DSSC and SC integrated devices

In recent years, the solar rechargeable SCs have been designed for the efficient utilization of solar energy by integrating the solar cells and SCs.^{18,293–295} Combining the energy storage devices with solar cells to generate on-grid and off-grid systems can provide the temporal flexibility to balance local power generation and consumption, and improve the overall energy utilizations.^{296–298} Electrochemical SCs,^{299–302} as mentioned previously, are promising candidates to sustain the power stability management for on-grid applications. Generally, the photo-energy conversion and energy storage devices are operated independently and are connected externally,^{303–305} resulting in additional space and energy consumption from the external connection systems and consequently a lower energy storage efficiency. The direct integration of the solar cells and SCs into individual units is a prospective way to develop highly efficient, light-weight, and portable rechargeable solar SC devices, which can convert solar energy *in situ* into electrochemical energy.^{306,307}

Most of the solar rechargeable SC research is based on the DSSCs, since DSSCs are very powerful even under diffuse and low intensity light conditions. An integrated DSSC/SC device generally comprises a DSSC photoanode, shared CE, and current collector of the SC in conjunction with two electrolytes. Under light illumination of the photoanode, the photo-active material is excited to form an electron–hole pair. The electrons move to the charge storage electrode where they are retained. The holes in the photoanode are counterbalanced by the electrons of the CE when the whole device is under the charged state. The electrons move back from the charge storage electrode to the CE during the discharging process. The overall efficiency of the integrated devices is dependent on both the energy conversion and storage materials, and the connection between solar cells and SCs. Firstly, the energy conversion and storage parts should be matched ideally for an efficient electron transfer, *e.g.* the voltage match and the geometrical size match. For example, organic PV systems can offer a voltage of about 800 mV, requiring a corresponding battery with fitting voltage. Also, geometrical restrictions limit the efficiency of the devices. The size of the DSSC and the SC determines the size of the corresponding counterpart, resulting in a possible capability mismatch. Secondly, the connection structure of the energy conversion and storage device should be designed for the optimal overall efficiency.

Early integrated DSSC/SC systems are based on a two-electrode configuration. In 2004, Miyasaka *et al.* developed a two-electrode integrated device with activated carbon as the storage material (Fig. 19a).²⁹⁴ The photo-generated positive and negative charges at the semiconductor–electrolyte interface are directly stored as double layer charges on the surface of active

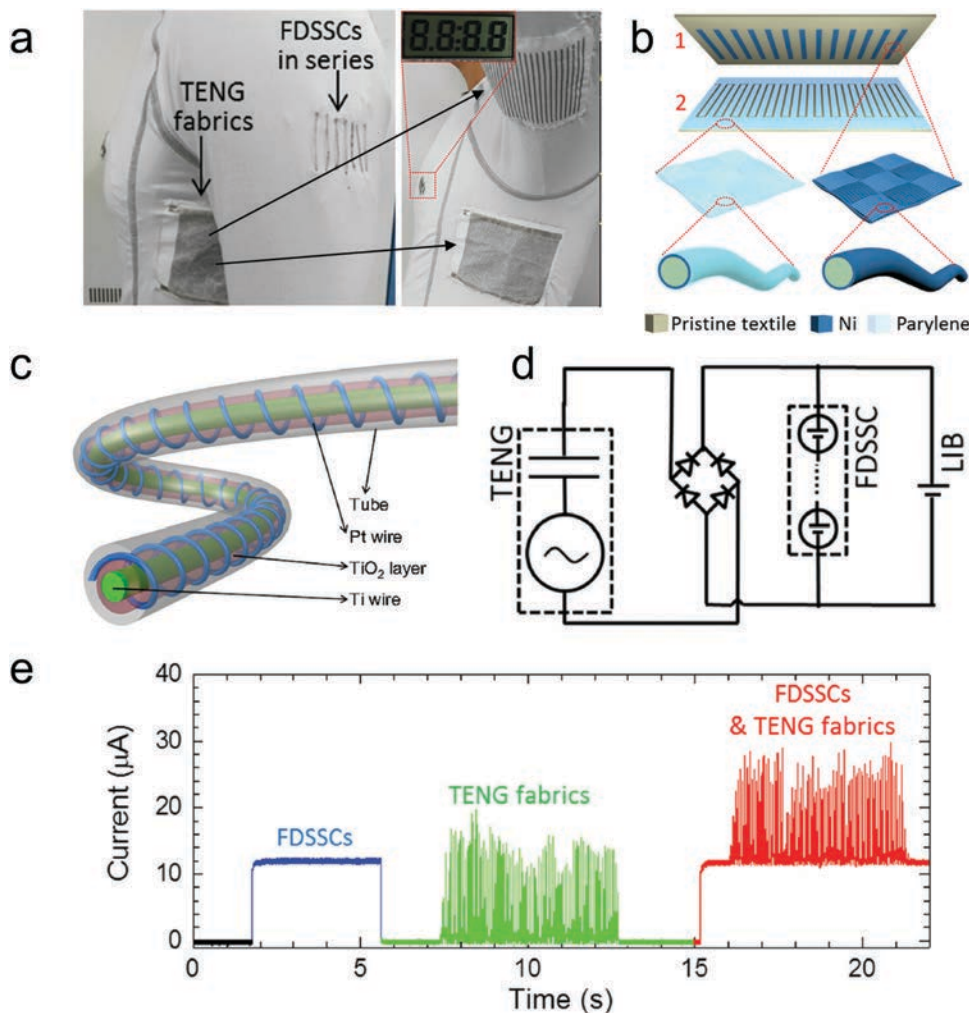


Fig. 17 (a) A photo of a power-textile with a pair of TENG fabrics and seven fiber-based DSSCs in series on the shoulder. (b and c) Are the scheme of textile TENG and fiber-based DSSC, respectively. (d) An equivalent circuit of a self-charging system. (e) The short circuit current of fiber-based DSSCs, TENG fabrics, and the hybrid power textile. Reproduced with permission from ref. 290. Copyright 2016 Wiley-VCH.

carbon. A problem of this method is a high internal resistance that slows the discharge process as electrons returning to the photo-electrode are supposed to go through the space charge Schottky barrier at the TiO_2 layer. The device achieved a voltage of 0.45 V in the charged state, and a discharge capacity of 75 mC cm^{-2} . Nagai and Segawa have developed a bridging three-electrode system that used an additional electrode for operation of efficient discharge by a redox reaction (Fig. 19b).³⁰⁸ Subsequently, researchers proposed a new configuration; further advancements were reported for a high-voltage DSSC/SC integrated system by introduction of an internal bifunctional electrode between the photoelectrode and CE, which conducts the redox electron transfer on one side and charge storage on the other side (Fig. 19c).³⁰⁹ This three-electrode configuration fabricated by Miyasaka *et al.* achieved a charge-state voltage of 0.8 V and high energy density per area of $47 \mu\text{W h cm}^{-2}$, which is five times larger than those of the previous two-electrode system.²⁹⁵ Because the planar format in such stacked devices has only limited application, other structures, such as wire-like

integration (Fig. 19d), have been developed to enhance the flexibility and lightweight of the integrated devices.³¹⁰ Such wires can be potentially woven into textiles or other deformable structures for self-powering applications, such as medical bio-monitoring devices or implants, or safety and construction gear like illuminated vests and wearable electronics.

Many reports of the three-electrode integrated DSSC/SC devices were devoted to the development of electrode materials for SC counterparts. A highly popular material for integrated DSSC/SC devices is the carbon nanotube (CNT). A DSSC/SC integrated device using a CNT film as the CE shows a PCE of 6.1%, a specific capacitance of 48 F g^{-1} , and a storage efficiency of about 84%, with an entire photoelectric conversion and storage efficiency of about 5.12% (Fig. 20a).¹⁴¹ To enhance the flexibility and lightweight of the integrated devices, Peng *et al.* utilized CNT/Ti wire composites and developed an integrated energy wire-shaped device, where the Ti wire was modified with TiO_2 NTs.³¹⁰ One part of the Ti wire was coated with a N719 dye, and the other part was covered with the electrolyte.

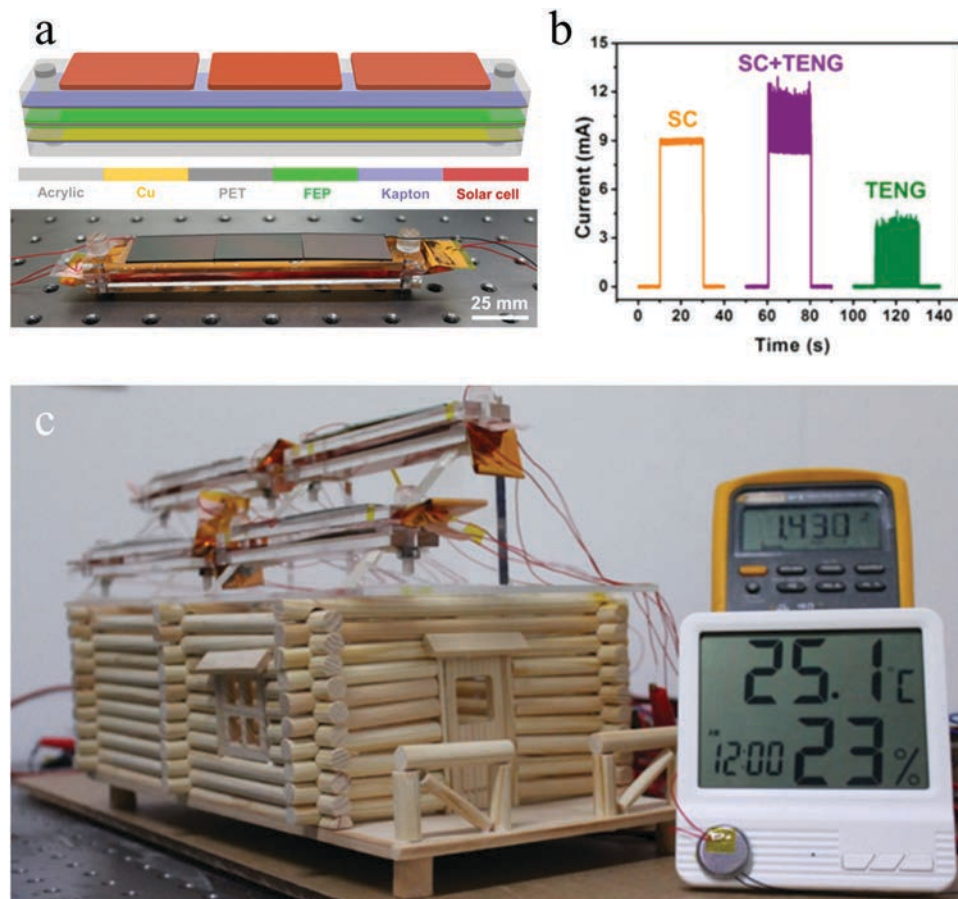


Fig. 18 (a) Schematic diagram of the hybrid NG. (b) The output current of the TENG, solar cell and the hybrid NG. (c) Photograph of a temperature–humidity sensor powered by the hybrid NG at room-light illumination and a wind speed of $\sim 15 \text{ m s}^{-1}$. Reproduced with permission from ref. 292. Copyright 2016 ACS.

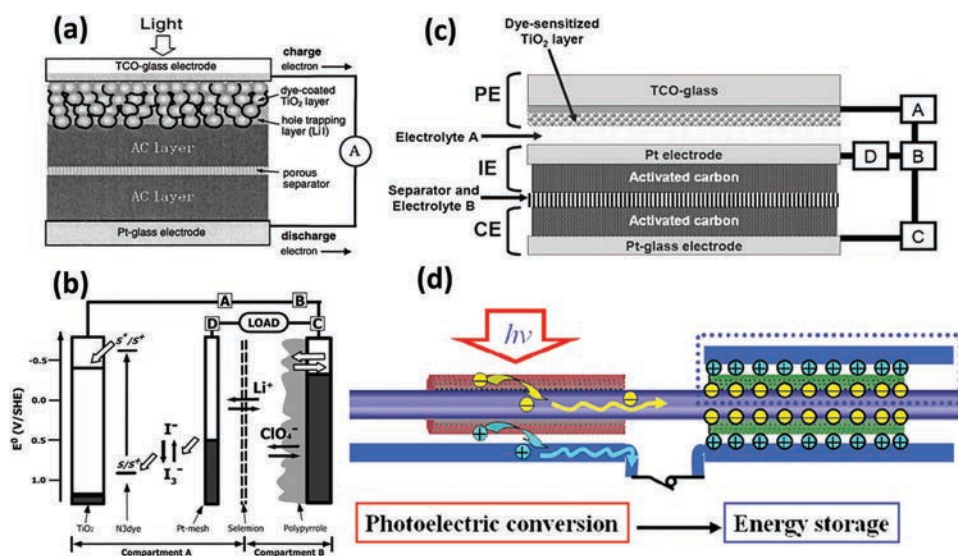


Fig. 19 (a) Schematic illustration of an integrated DSSC/SC device employing the two-electrode system, (b) a bridging three-electrode system, (c) the three-electrode system and (d) the wire-shaped system. Reproduced with permission from ref. 132, 294, 295 and 308. Copyright 2004 AIP; Copyright 2004 RSC; Copyright 2005 RSC; Copyright 2012 Wiley-VCH.

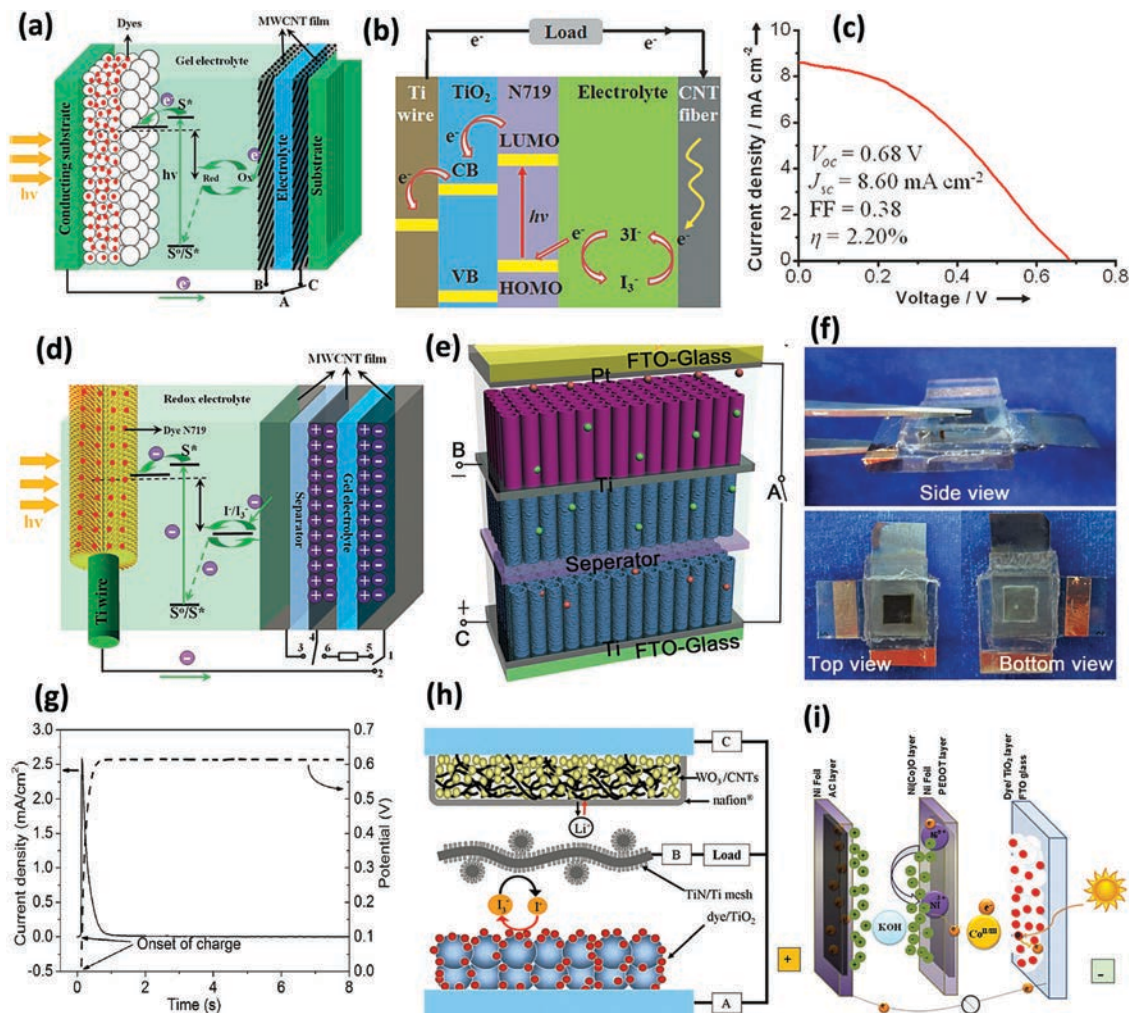


Fig. 20 (a) Schematic illustration of an integrated DSSC/SC device based on aligned multi-wall CNT films as electrodes. Reproduced with permission from ref. 141. Copyright 2013 RSC. (b) Device based on the CNT/Ti wire as electrodes and (c) typical current density/voltage curve under the illumination of AM 1.5. Reproduced with permission from ref. 132 Copyright 2012 Wiley-VCH. (d) DSSC/SC device employing Ti/TiO₂ coaxial and aligned structured electrodes in the sheath and storage. Reproduced with permission from ref. 312. Copyright 2014 Wiley-VCH. (e) Based on bi-polar TiO₂ NT arrays, (f) photograph of an integrated DSSC/SC device from side, top (DSSCs part) and bottom view (SC part), and (g) the current density and voltage transients of SC during photocharge. Reproduced with permission from ref. 306. Copyright 2014 Wiley-VCH. (h) Device based on WO₃ coated CNTs as electrodes. Reproduced with permission from ref. 314. Copyright 2012 ECS. (i) DSSC/SC based on Co-doped NiO electrode. Reproduced with permission from ref. 316. Copyright 2014 Elsevier.

The wire achieved an entire photoelectric conversion and storage efficiency of 1.5% (PCE is 2.2%) with a wire thickness of 10–30 μm (Fig. 20b and c).¹³² Peng *et al.* modified the Ti substrate with perpendicularly aligned TiO₂ NTs on the surface and horizontally aligned CNT, which served as two electrodes in the fiber device.³¹¹ The aligned NTs thereby offered a high performance and an effective pathway for the charge transport. The PCE reached 2.73% with an energy storage efficiency of 76%.²⁹³ Further, a self-powered energy fiber with energy conversion in the sheath and storage in the core was developed by using Ti/TiO₂ as the photoanode within the energy-storage component while the electrolyte was sandwiched between two aligned CNT sheets (Fig. 20d). The CNTs remained highly aligned after being wound around the fiber substrate. This alignment enabled high photoelectric

conversion and storage performance under bending and stretching of 10% and 20%, respectively, despite a slight decrease in the photovoltage when the fiber was stretched beyond 30%.³¹²

Other charge conversion-storage systems employ photo- and electro-active materials like some metal oxides. Bi-polar anodic TiO₂ NT arrays and a selective plasma-assisted hydrogenation treatment were employed to construct integrated DSSC/SC devices with improved SC performance (Fig. 20e–g).³⁰⁶ The optimized integrated device exhibited an overall photoelectric conversion and storage efficiency of 1.64%, with a fast response and superior cycling capability for more than 100 photocharge/galvanostatic discharge cycles without any decay. Compared with TiO₂, WO₃ exhibits a lower conduction band and unique optical/electrical performance.³¹³ Gao *et al.* utilized WO₃ coated

CNTs as the electron storage electrode, common DSSC photoanodes with N719 dye, and an electrocatalytic CE consisting of a TiN/Ti mesh for the reduction of I_3^- to I^- to take place (Fig. 20h).³¹⁴ The photo-charge efficiency of the three-electrode integrated DSSC/SC device can reach 69.5% compared with the electrochemical charge process.³¹⁵ In addition, an integrated DSSC/SC device reported a specific capacitance of 46 F g^{-1} for a single SC device. By studying the individual electrodes, redox peaks were observed in the voltammogram of the cobalt-doped NiO electrode, ensuring the effective energy storage within the electrode/electrolyte interface ascribed to the redox transition. Nevertheless, a 14 F g^{-1} capacitive reduction of the asymmetric SC was observed, resulting in a capacitance of 32 F g^{-1} and an efficiency of 0.6% for the integrated device (Fig. 20i).³¹⁶

Apart from carbon materials and transition metal compounds, organic conjugated polymers such as polypyrrole (PPy) were utilized by Segawa *et al.* as capacitor materials in a three-electrode integrated conversion-storage system. The PPy films on an indium tin oxide (ITO) slide were used as a charge-storage electrode to achieve capacitances of up to 1.91 mC cm^{-2} and charge storage efficiencies of up to 22%.³⁰⁸ Gao *et al.* utilized the dye-sensitized $\text{TiO}_2/\text{PEDOT}$ photoanode as positive charge storage while a p-doped PPy CE acted as electron storage in LiClO_4 electrolyte. The total photoelectric conversion and storage efficiency was about 0.1%.²⁹⁶ Another conducting polymer film-based integrated device was fabricated by using a

poly(3,4-(2',2'-diethyl)-propylenedioxythiophene) (PProDOT-Et₂) conducting polymer thick film as an energy storage material and an N_3 dye- TiO_2 DSSC as an energy conversion device, which showed an energy storage efficiency of 0.6%.³¹⁷

Notably, in a hydrogenated single crystal ZnO@amorphous ZnO doped MnO_2 core shell nanocable (HZM), flexible SC showed a specific capacitance of 1260.9 F g^{-1} under inductively coupled plasma atomic emission spectroscopy when the loading of MnO_2 reached 0.11 mg cm^{-2} . Furthermore, a stand-alone self-powered system was composed of their newly fabricated all solid-state SC, DSSC, and light emitting diode (LED). This novel, self-powered system successfully lit up a blue LED using three series-connected SCs. A red LED was lit for more than 30 min by a SC after being charged for 2 min using four series-connected DSSCs (Fig. 21a).³¹⁸ The three series-connected SCs were charged at 0.5 mA to a potential of 2.4 V and kept at 2.4 V for 5000 s (the current profile), indicating a small leakage current (Fig. 21b). It attained $\sim 2.3 \text{ V}$ after 120 s of charging when it was charged by four in-series-connected DSSCs (the voltage profile).

Further, an all silicon electrode integrated DSSC/SC device for integrated energy storage and conversion was developed by Pint's group (Fig. 21c and d).³¹⁹ Authors demonstrated a simple wafer-scale process by which an individual silicon wafer could be processed into a multifunctional platform where one side was adapted to replace Pt and enable triiodide reduction in a

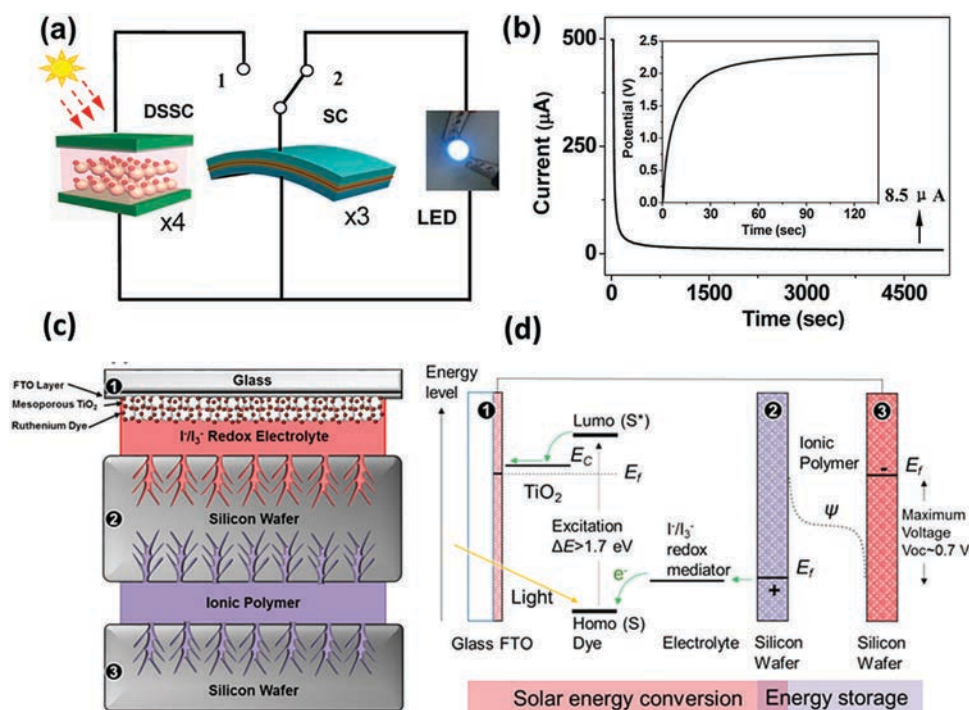


Fig. 21 (a) Schematic illustration of integrated four series-connected DSSC and three series-connected flexible SC devices based on hydrogenated single crystal ZnO@amorphous ZnO doped MnO_2 core shell nanocable (HZM), and (b) leakage current curve of three series-connected SCs. The inset is the voltage profile for three SCs in series. Reproduced with permission from ref. 318. Copyright 2013 ACS. (c) Scheme of the integrated device configuration, showing the three-electrode architecture utilized in testing of the integrated solid-state DSSC/SC system with the porous silicon layer responsible for both the energy storage and conversion active materials. (d) Band diagram of the integrated device and charge transport processes occurring under illumination. Reproduced with permission from ref. 319. Copyright 2015 ACS.

DSSC, while the other side provided on-board charge storage as an electrochemical SC. The utilization of this silicon multi-functional platform as a combined energy storage and conversion system yielded a total device efficiency of 2.1%.

3.4. DSSC and SC and NG integrated devices

Bae *et al.* integrated a DSSC, SC, and NG simultaneously on a single micro sized fiber to realize solar and mechanical energy harvesting and subsequent storing, as shown in Fig. 22.³²⁰ The NG, SC, and DSSC share a common substrate which is an Au-coated polymethylmethacrylate (PMMA) fiber of diameter ~ 220 μm . The Au layer serves as the common inner electrode. Then, ZnO NWs were radially grown on the fiber as the active piezoelectric material of the NG, core material of the DSSC, and large surface area SC. As for the NG, graphene coated copper meshes were wrapped around the fiber to serve as the outer electrode. Under a shear stress driven by a push action at 5 Hz, the peak output current and voltage were 2 nA and 7 mV, respectively. To facilitate the SC, a PVA/H₃PO₄ gel electrolyte was filled in after the graphene-coated copper meshes were wrapped around. The fabricated SC has a capacitance per unit length of 0.025 mF cm⁻¹. As for the DSSC, the grown ZnO NWs were sensitized with a N719 dye solution, a ZnO NW-grown graphene sheet was wrapped around the fiber as the outer electrode, and

finally a liquid electrolyte was filled in. The J_{sc} , V_{oc} , FF and PCE of the DSSC were 0.35 mA cm⁻², 0.17 V, 0.39, and 0.02%, respectively.

3.5. PSC and SC integrated devices

For the integrated energy conversion-storage systems, one of the critical issues that needs to be addressed is the enhancement of the PCE of current solar cells. In this regard, the recent availability of high-performance PSCs could not only facilitate the development of highly efficient (up to 20%) and low-cost solar cells for practical applications but also allow for the integration of PSCs into various energy systems. Some efforts were devoted to the connection between PSCs and SCs. In 2015, Wang's group integrated MAPbI₃-based PSC and PPy-based SC as an energy pack (Fig. 23) and realized a high output voltage of 1.45 V and an overall output efficiency of 20% when the voltage of SC was set at 0.6 V. This system affords continuous output of electric power by using MAPbI₃-based solar cells as an energy source, mitigating transients caused by light intensity fluctuations or the diurnal cycle.³²¹ In 2016, Chai *et al.* developed a perovskite photo-voltachromic supercapacitor (PVCS) with all-transparent electrodes.³²² They integrated the semitransparent PSC and electrochromic WO₃ SC into the PVCS in a vertically stacked configuration, which improved the integration level, achieved widely and automatically tunable optical transmittance of the

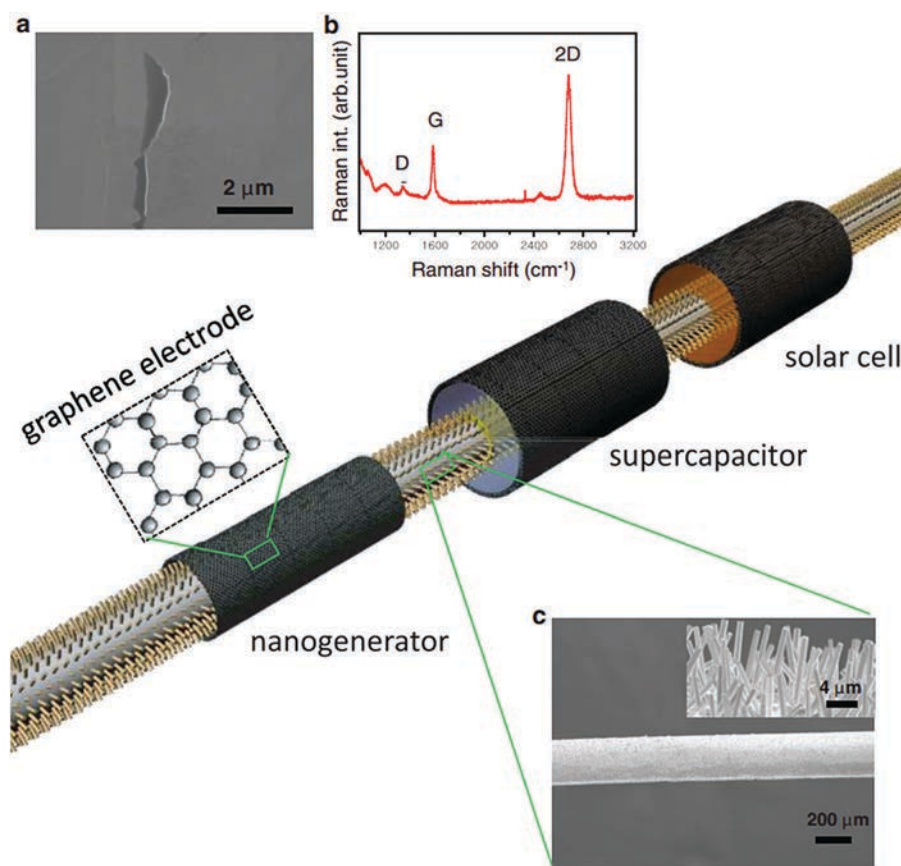


Fig. 22 (a) SEM image of graphene. (b) Raman spectra of the graphene film. (c) The schematic diagram of the hybrid power cell and the SEM image of Au-coated PMMA fiber covered with ZnO NWs. Reproduced with permission from ref. 320. Copyright 2011 Wiley-VCH.

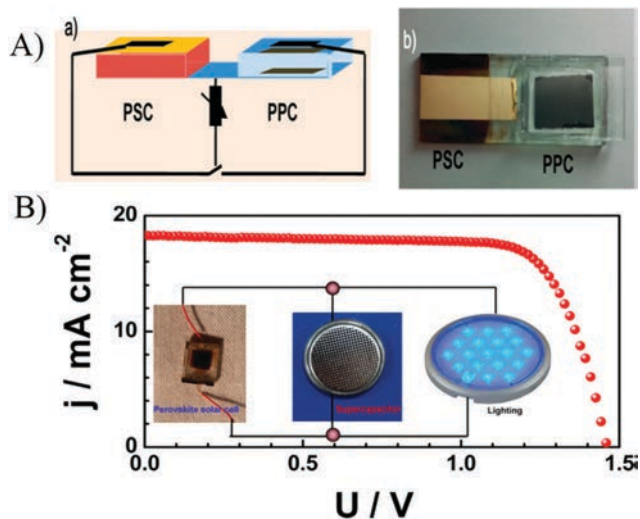


Fig. 23 (A) Structural scheme and photograph of an integrated energy pack containing a MAPbI₃-based PSC and a PPy-based SC, and (B) the performance of the integrated device. Reproduced with permission from ref. 321. Copyright 2015 ACS.

integrated device, and could store the electrochemical energy accompanied by a color change. The power conversion efficiency of the PV component in the co-anode (co-cathode) PVCS was 8.25% (11.89%), while the energy density, average power density, and areal capacitance of the integrated device were 35.9 mW h m⁻², 461.5 mW m⁻², and 459.6 F m⁻², respectively. Peng *et al.* presented a fusible device, where the SCs and PSC are fused to integrated devices by connecting the composite electrode from a SC with the composite electrode from a PSC.³²³ The energy storage was based on CNT/polyaniline (PANI) composites while the energy conversion was based on TiO₂, MAPbI₃, and spiro-OMeTAD. Compared with

the traditional connection by external conducting wires, these fusible energy devices can be fused into various patterns at room temperature with high stability, high efficiency and low cost.

3.6. SSC and SC integrated devices

The most well-known and established solar cell device is the crystalline silicon solar cell (SSC).^{324,325} This technology still dominates the field of commercial PV modules despite its inflexibility, high weight, and high production cost.^{326,327} SSCs are generally suitable for an integrated energy storage system. As depicted in Fig. 24, a direct integration of a SC into the backside of a SSC has been demonstrated by Pint *et al.*³²⁸ First, a commercial polycrystalline SSC panel (400 mA, 22 W, 14.8% cell efficiency) was pre-treated with a 1 M KOH solution to remove the Al current collector from the silicon absorbing layer. Following that, electrochemical etching using a 3 : 7 v/v HF and ethanol solution was performed directly into the backside of the polycrystalline SSC to fabricate porous silicon SC with 84% Coulombic efficiency. A mixture composed of polyethylene oxide (PEO), 1-ethyl-3-methyl imidazolium tetrafluoroborate (EMIBF₄), and propylene carbonate (PC) in a 1 : 1 : 8 ratio by weight was subsequently cast onto the SC electrode, and was sandwiched with an equivalently prepared single crystalline porous silicon counter-electrode. Finally, an integrated solid-state SC and SSC was fabricated by removing the PC in a vacuum oven for 24 h at 50 °C. The porous silicon SC coupled with solid-state polymer electrolytes was used to achieve a solid-state architecture that sustained mechanical integrity and required no external electrolyte packaging. This design demonstrated that the SSC can charge the SC under an external load and that a constant current load can be maintained through periods of intermittent illumination, showing the feasibility of this integration concept as a way to advance the

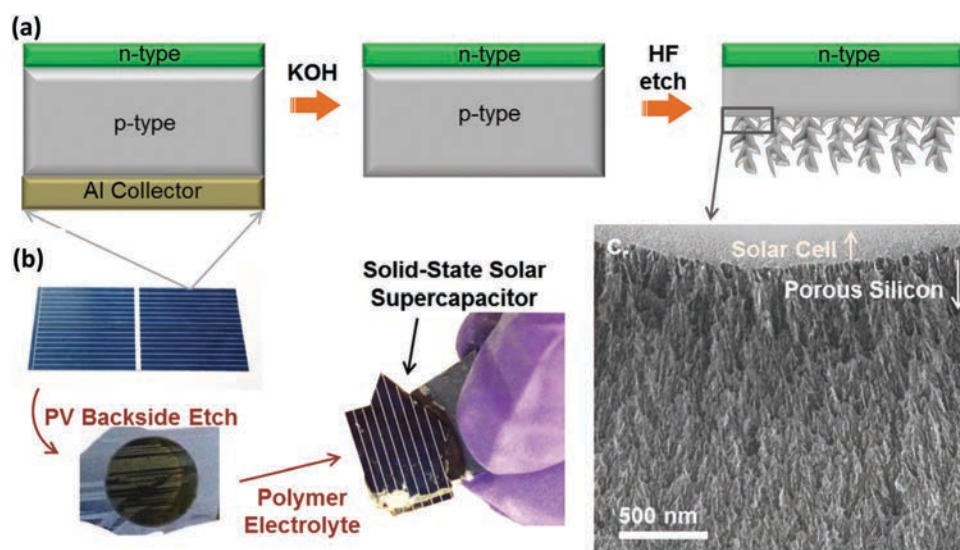


Fig. 24 (a) Scheme demonstrating key steps for fabrication of a solid-state integrated SC with a commercial SSC, including KOH dissolution of the Al collector material, and HF electrochemical etching to produce porous silicon. (b) Photographs of the polycrystalline SSC after HF etching showing the dark circular porous silicon material, (c) SEM image of the interface of the porous silicon energy storage material and the absorbing layer of the solar cell. Reproduced with permission from ref. 328. Copyright 2014 AIP.

device performance and a practical scheme for integrated solar storage and application.

Since present solid-state PV cells and traditional PEC cells cannot directly store the converted energy, a kind of direct solar energy conversion and storage by coupling between PEC and ferroelectric effects has been developed by Jiang *et al.*³²⁹ In this paper, solar energy could be converted to electrical energy and directly stored in the form of mobile charge in a single structure by using an intrinsic coupling between the PEC material of Si and ferroelectric material of poly(vinylidene fluoride) (PVDF). The device consisted of a transparent electrode, a current collector, a LiPF₆ containing electrolyte, and ferroelectric PVDF particles, which were bound on silicon particles and a ferroelectric PVDF membrane. The integrated device configuration was photo-charged under 1000 W m⁻² of white light to reach a V_{oc} of 0.47 V with a capacity of 37.62 mC cm⁻². The open-circuit output voltage was seen to be stable over 24 hours while its mobile charge was stable for more than 8 h in a dark environment. This new type of integrated device is based on the PEC and ferroelectric effects that holds the dual roles of solar energy harvesting and storage, and can be applied in a broad range of applications.

3.7. Organic solar cell (OSC) and SC integrated devices

The development of a number of modern portable devices and sensors requires the realization of flexible devices and long term off-grid power. In this respect, devices that are capable of performing different functions in a single unit, simultaneously realizing energy conversion and storage would be advantageous. OSCs are solution-processable, potentially low-cost, and suitable for ubiquitous deployment. SCs exhibit high power densities (15 kW kg⁻¹) with rapid charge–discharge cycles, and are inherently safe while posing a relatively low environmental impact. Polymer OSCs and electrochemical SCs, being promising options for energy harvesting and storage devices, have been realized as flexible films which expands their application in various portable electronic areas. Similar to other integrated devices, such as DSSC/SC, PSC/SC, or SSC/SC, integrated OSC/SC devices can also offer energy on demand for off-grid applications. As illustrated in Fig. 25a–d, an integrated OSC/SC device can be realized by eight-series connected OSCs based on P3HT:PC₆₀BM (P3HT stands for poly(3-hexylthiophene), and PC₆₀BM stands for [6,6]-phenyl-C60-butyric acid methyl ester) BHJ with Al electrodes and SCs based on graphene ink on a single substrate, using graphene as a common platform. The series-connected OSCs provide the energy harvesting capability and achieve a V_{oc} of about 5 V and a PCE of approximately 1.6%. The SCs provide the energy storage capability and generate approximately 2.5 mF cm⁻² capacitance. Together, the integrated OSC/SC device yields an overall system voltage of up to 4 V, which is suitable for driving red, green, and blue LEDs. The design of a graphene-based integrated OSC/SC device realizes a lighter and more flexible power pack with a mass of 0.35 g (including the substrate) for low-cost, self-powered electronic systems. The solution-processable, integrated device can be envisioned to be printed onto a single flexible

substrate, which makes the process compatible with roll-to-roll manufacturing.

Since integrated devices with a conventional planar structure cannot meet the ongoing demand in the modern electronics of being lightweight, small, and weaveable in the modern electronics, it is highly desirable to develop flexible integrated devices. As mentioned in the previous sections, wire-shaped DSSCs can be integrated with SCs. However, as the wire-shaped DSSC part was sealed separately, the resulting devices were still planar. Sealing DSSCs and SCs together was seen to render devices ineffective and contribute to poor mechanical stability. This means that at this point in time the flexible integration of DSSCs for lightweight, fiber-like, and portable devices cannot be realized. In contrast, an all solid-state, coaxial, and self-powered “energy fiber” has been developed based on polymer OSCs without liquid electrolytes while integrated electrochemical SCs have been developed, which can simultaneously convert solar energy into electrical energy and store it in the SC part (Fig. 25e and f).³³¹ The coaxial structure in flexible devices can provide a much higher effective contact area that favors a rapid charge transport as well as stable performance, while the use of flexible, transparent, strong, and conductive CNT sheets can greatly improve the photoelectric conversion and energy storage. The combined photoelectric conversion and storage efficiency of the integrated fiber-shaped OSC/SC device reached 0.82%, which remained nearly unchanged with further increasing of the CNT layer thickness. This promising flexible fiber-shaped integrated device can be further scaled up for practical application in flexible electronics and in combination with the well-developed textile technology.

4. Integrated photoelectrochemical cells (PECs) based on DSSCs and PSCs

The application of dye-sensitized electrodes for the direct generation of solar fuels is a relatively new aspect of photoelectrochemical cell (PEC) research while substantial progress has been achieved in the last ten years. This technology has still a long way before reaching a higher PCE comparable to the one achieved in electricity-generating regenerative DSSCs. Such chemical-producing cells can be termed as dye-sensitized photoelectrosynthesis cells (PESCs) as distinguished from the well-known electricity-generating regenerative DSSCs. More information on the basic principles and the detailed operation of the various dye-sensitized PESCs as well as the underlying molecular chemistry concepts is available in a number of reviews.^{332–349} With respect to photooxidation reactions at n-type dye-sensitized PESCs, the reaction attracting most attention is water oxidation to oxygen. Another aspect is the dye-sensitized photooxidation of organic compounds; effluent water remediation is a related application aspect. With respect to photoreduction reactions at dye-sensitized PESCs, two reactions attracting substantial interest are the H₂O reduction to H₂ and the CO₂ reduction, the latter targeted at both the generation of useful carbonaceous fuels and the reduction of the

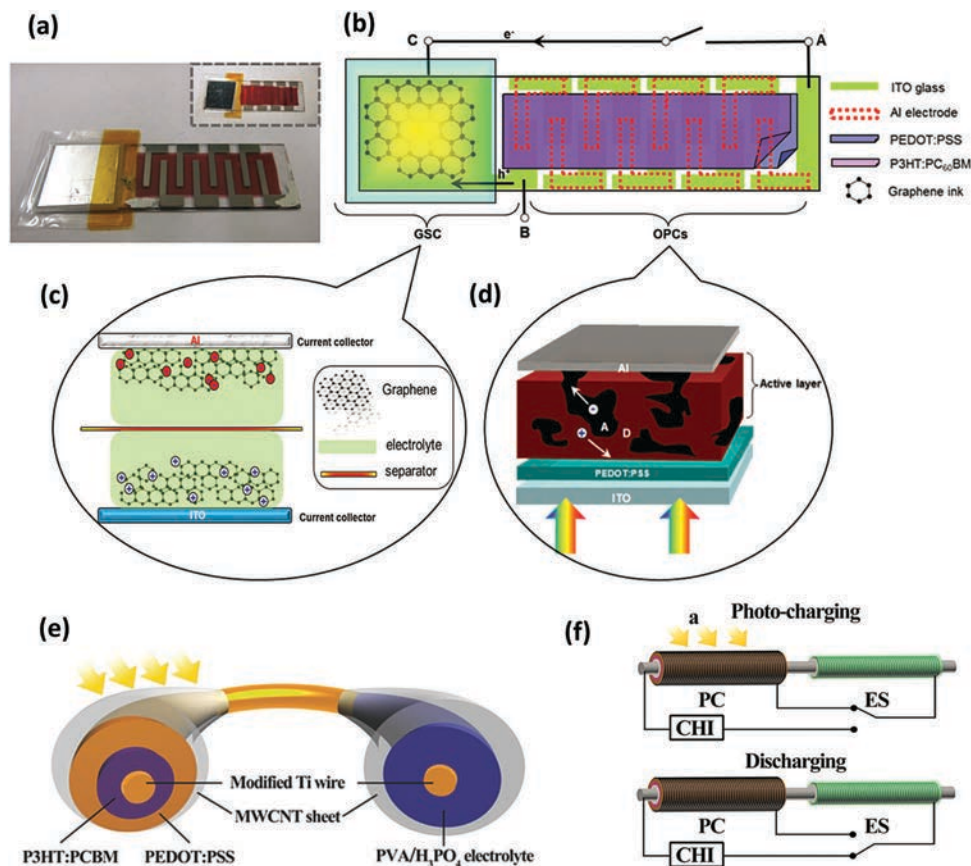


Fig. 25 The front (a) and the back (the inset) view of an integrated OSC/SC device photograph. (b) Schematic illustration of an integrated device based on a graphene ink SC with ITO/glass and Al foil current collectors. (c) A graphene ink SC with ITO/glass and Al foil current collectors. (d) OSCs with a structure of ITO/PEDOT:PSS/P3HT:PC₆₀BM/Al. Reproduced with permission from ref. 330. Copyright 2015 Wiley-VCH. (e) Schematic illustration of an integrated OSC/SC device in a flexible and stable fiber format and (f) the circuit connection state of an integrated OSC/SC device in the process of charging and discharging. Reproduced with permission from ref. 331. Copyright 2014 Wiley-VCH. OPC: organic PV cells; GSC: graphene ink supercapacitor; PC: photovoltaic conversion; ES: energy storage.

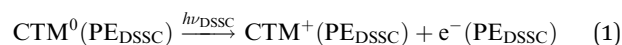
amount of CO₂ in the atmosphere. In addition to dye-sensitized PESC, two alternative options, to which the present section is devoted, consist of either (a) coupling one or more electricity-generating DSSCs or a PSC to a PESC needing an additional bias potential or (b) coupling one or more PSCs to an electro-synthetic cell with dark electrodes.

4.1. DSSC/PESC coupled cells for hydrogen generation

To date, dye-sensitized PESC incorporating direct water oxidation to hydrogen and/or reduction to hydrogen at the dye/semiconductor interface are at best by one order of magnitude less efficient than DSSCs converting light to electricity. Therefore, a preferable solution, from the efficiency point of view, is to couple two or three DSSCs, the number depending on the DSSC voltage, to a traditional electrolysis cell. However, at present, DSSCs would not be mature enough for this technology-oriented approach in terms of reaching simultaneously both a high PCE (exceeding 10%) and long-term stability. There is interest in investigating the combination of PESC, needing an external bias voltage, and DSSCs providing this voltage. Such PESC can be based on the direct irradiation

of semiconductor materials, e.g. n-Fe₂O₃, n-WO₃, n-BiVO₄, or p-Cu₂O. Alternatively, a PESC with an n- or p-type PE and a dark CE can be coupled to a DSSC in order to cover the external voltage bias requirement. First, the basic principles of the coupling of a DSSC to a PESC will be discussed, and then literature examples will be presented. For the sake of brevity, the case of a PESC based on direct semiconductor excitation will be considered but the analysis can be readily extended to an alternative option of a PESC with dye-sensitized electrodes. Additionally, CE and conductive semiconductor substrates with electrons, not holes, as carriers of electricity will be considered. Several reviews present the basic concepts of coupling DSSCs to PESC.^{350–354}

The overall photoelectrode (PE) reaction at the DSSC can be written as

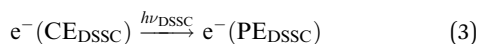


where CTM (PE_{DSSC}) is the charge-transport species between the photoelectrode and CE in the DSSC, which can be a redox mediator in a liquid electrolyte or a solid-state hole conductor.

The CE reaction of the DSSC part of the tandem cell is



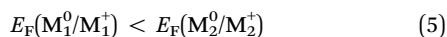
The overall DSSC process can be written by adding the last two equations as



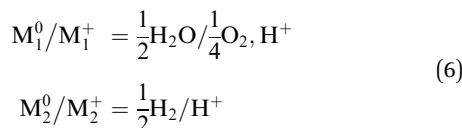
The two redox couples in the PESC interacting with the anode (oxidation electrode) and cathode (reduction electrode) will be termed M_1^0/M_1^+ and M_2^0/M_2^+ , respectively, with the corresponding half-reactions summarily formulated as one-electron reactions, as explained in the section devoted to n-PESCs:



Additionally,



For water electrolysis in acidic solutions

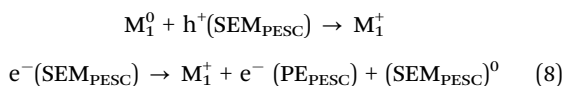


Here, H^+ means the generation of hydronium ions as the product.

First, the case of an n-type PESC, henceforth to be designated as n-PESC, will be considered. If SEM_{PESC} is the directly irradiated semiconductor electrode of the PESC, then the photoexcitation reaction generating an electron in the conduction band and a hole in the valence band is



Holes are driven to the surface and react with M_1^0 toward M_1^+ , while electrons are driven to the conductive PE support



The overall n-PESC photoelectrode reaction is



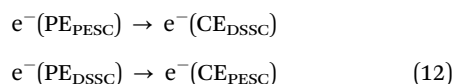
The n-PESC CE reductive reaction is



By adding the last two equations, the overall n-PESC reaction is derived:



The processes coupling the DSSC and the n-PESC are



In this respect, the photoelectrode of the PESC is short-circuit connected to the CE of the DSSC, and the CE of the PESC to the photoelectrode of the DSSC.

By adding together the last three equations, the overall tandem cell reaction consisting of a DSSC coupled to an n-PESC is derived as

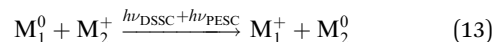
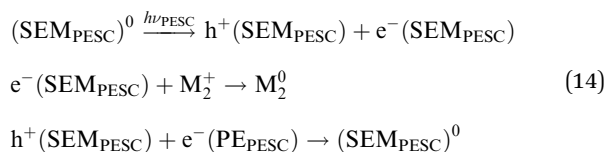


Fig. 26 shows the energy diagram for the coupling of an n-PESC and an n-DSSC. The case of a DSSC coupled to a p-type PESC photoelectrode can be similarly described, with the essential difference that photo-generated electrons are driven toward the electrolyte and holes toward the semiconductor bulk



with 0 in the last equation indicating the hole originating from SEM_{PESC} being annihilated by an electron $e^{-}(\text{PE}_{\text{PESC}})$ originating from the conductive support of the PESC.

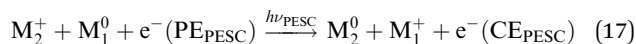
The overall p-PESC photoelectrode reaction is derived by adding the last three relations:



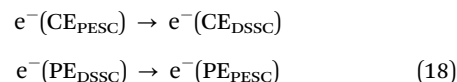
The p-PESC CE oxidative reaction is



By adding the last two equations the overall p-PESC reaction is derived:

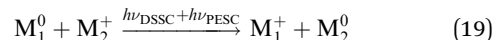


The processes coupling the DSSC and the p-PESC are



In this respect, the photoelectrode of the p-PESC short-circuit is connected to the photoelectrode of the DSSC, and the CE of the p-PESC to the CE of the DSSC.

By adding together the last three equations to that for the overall DSSC process the overall tandem cell reaction consisting of a DSSC coupled to a p-PESC is derived as



which is identical to eqn (13) derived for the n-PESC/DSSC hybrid system. As regards the practical aspects of connecting the two devices, the PESC can be totally separated from the DSSC, being connected in series with the DSSC as indicated above. However, in principle a more compact configuration is desired. The first configuration is the so-called artificial leaf (see Fig. 27) in which the photoelectrode and the CE of the PESC are placed at the outside of the DSSC, directly on top of the CE

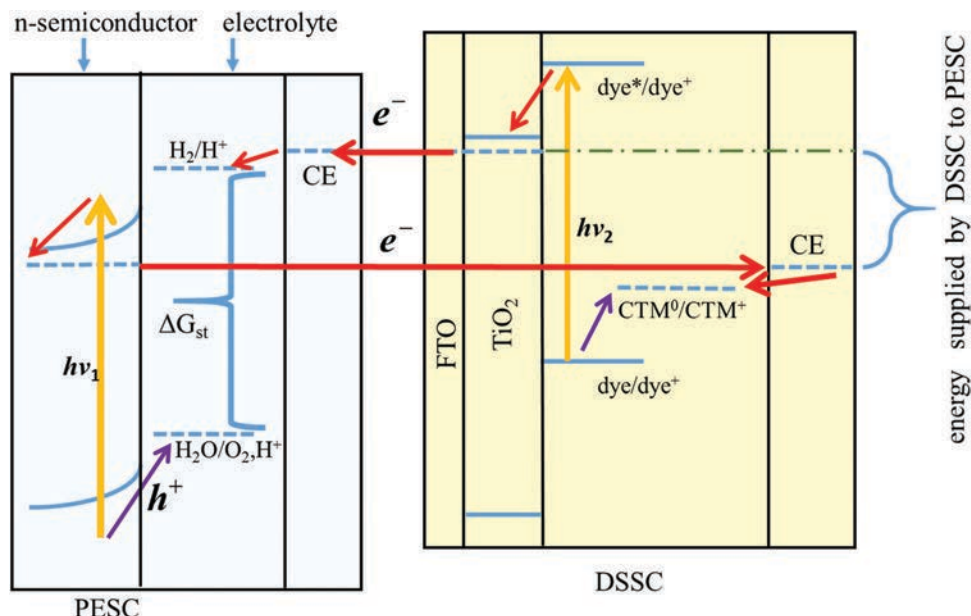


Fig. 26 Schematic of the DSSC/PESC tandem cell with an n-type PESC in series to a DSSC. The energy was supplied by DSSC to PESC. The long horizontal arrow pointing to the right indicates electrons flowing from the PESC's photoelectrode to the short circuit-connected DSSC's CE. The short horizontal arrow lying above the long arrow and pointing to the left indicates electrons flowing from the DSSC photoelectrode to the short-circuited PESC CE.

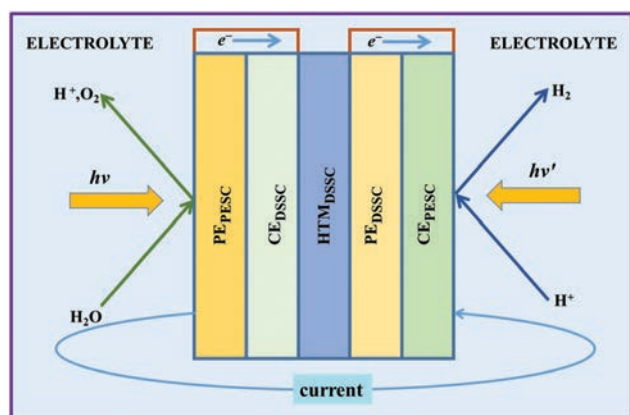


Fig. 27 Schematic of an artificial leaf-type compact n-PESC/DSSC tandem cell. Illumination from the PESC may be sufficient in the case of transparent CE_{DSSC} . Alternatively, in the case of transparent CE_{PESC} illumination from both sides is possible, *i.e.* by means of a beam splitter.

and photoelectrode of the DSSC, respectively. The assembly is dipped into a single external compartment of an electrolyte, which wets both the CE_{PESC} and PE_{PESC} . The DSSC charged-transport medium is prevented from contacting the external electrolyte by appropriate sealing.

The assembly can be illuminated from one side or from both sides. In the latter case all electrodes should be deposited on TCO glass. One possibility is to use a glass plate coated on both sides with TCO layers which are appropriately connected by a short circuit, *e.g.* by means of conductive Ag paint. Alternatively two single-sided-coated TCO-supported electrodes are brought into contact, with the uncoated sides touching

one another, while the conductive sides are short-circuit connected.

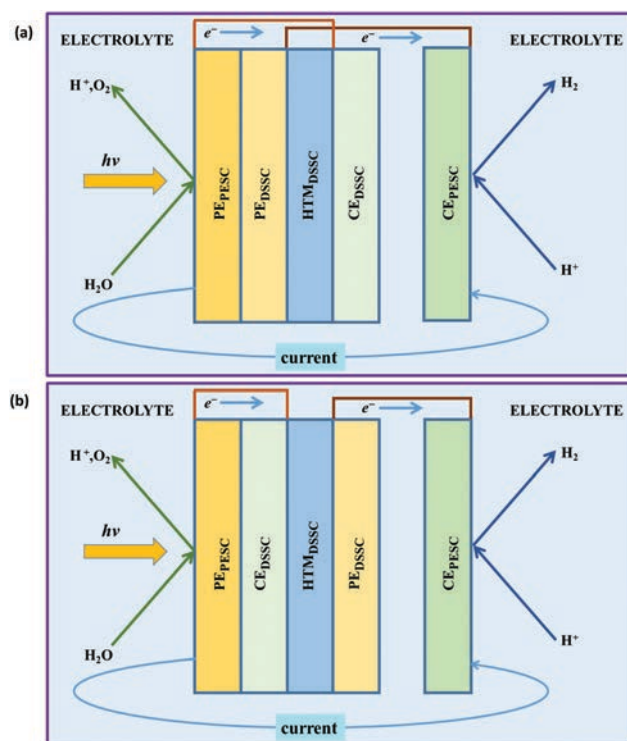
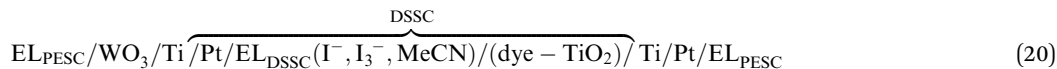


Fig. 28 Schematic of the modification of the cell in Fig. 27 with CE_{PESC} detached from the compact assembly of DSSC and PE_{PESC} and with PE_{DSSC} positioning (a) either immediately next to PE_{PESC} or (b) next to a sufficiently transparent CE_{PESC} .

In the case of one-side illumination, the properties of the materials between the photoelectrodes should be adjusted so that minimal light absorption takes place in the interior of the tandem assembly. In the case of two side illumination, two

Park and Bard described an artificial-leaf type cell of the general configuration of Fig. 27.³⁵⁵ A weakly acidic aqueous electrolyte was in contact with a WO₃ photoelectrode and a Pt CE according to the configuration was



approaches can be considered. Each of the photoelectrodes can be exposed to full sunlight. Alternatively, a beam splitter is used to appropriately divide the incident light into two parts so that the spectrum of each part matches the absorption properties of the photoactive substrate to which it is directed.

A modified artificial leaf assembly is depicted in Fig. 28a, with sunlight impinging only on the PE_{PESC}. For practical reasons, the CE of the PESC unit is kept at some distance from the photoelectrode of the DSSC unit, being separated from the DSSC electrode by an electrolyte layer. Another variety of the above cell involves the order of placement of PE_{DSSC} and CE_{DSSC} reversed, as indicated in Fig. 28b with the light emerging from PE_{PESC} directed first through CE_{DSSC} and then through PE_{DSSC}. It should be noted that the configuration of the electrode connections is thereby somewhat different from the previous case.

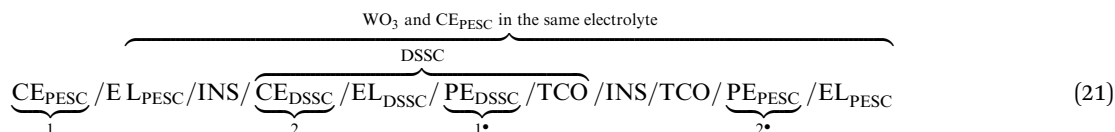
In the following paragraphs of this section the literature examples of tandem DSSC/PESC systems will be classified according to the type of the photoactive electrode.

(a) WO₃ and hematite Fe₂O₃. Both Fe₂O₃ and WO₃ semiconductors absorb a substantial amount of light in the 400–500 nm region, Fe₂O₃ being a stronger light absorber (band gap 2.1 eV) compared to WO₃ (2.6 eV). Polycrystalline WO₃ attracted a lot of attention for PESC applications in the polycrystalline form back in the 1980s. Contrarily, substantial efforts have been devoted in the last 20 years toward the synthesis of polycrystalline Fe₂O₃ in the hematite form to produce materials with desirable photocurrent density values in PESCs, *i.e.* exceeding 1 mA cm⁻² under full sun. Therefore, systematic work in the latter started appearing in the literature only from the year 2000 onward. The main disadvantage of both materials is that the conduction band edge (E_{cb}) lies significantly below $E_{\text{F}}(\text{H}_2/\text{H}^+)$. Additionally, at electrode potentials positive of the photocurrent onset, the photocurrent increases gradually due to substantial recombination reactions, competing favourably with O₂ evolution, so that a substantial difference $E_{\text{F}}(\text{H}_2/\text{H}^+) - E_{\text{F}}(\text{PE})$, larger than that accounted of the E_{cb} position, is needed. Therefore for photocurrents exceeding 1 mA cm⁻² the applied bias potential may exceed 0.5 V so that two DSSC cells could be needed.

with EL_{PESC} indicating the electrolytes in the DSSC and PESC subunits. The composition of EL_{PESC} was 0.25 M Na₂SO₄ at pH = 4 (fixed with HClO₄). Under illumination provided by a Xe lamp of 100 mW cm⁻² the photocurrent onset was +0.33 V/RHE (*vs.* a reversible hydrogen electrode in the same solution). The energy storage efficiency was 1.9% for a DSSC based on the well-known N719 dye, of the Ru(bpy)₂(SCN)₂-type, and the I⁻/I₃⁻ mediator; the current density was 1.6 mA cm⁻². A higher η_{st} of 2.6% was obtained by applying an external bias potential of 0.2 V, to the tandem solar cell. In fact, the output of the traditional I⁻/I₃⁻-based DSSCs is not sufficient for a single DSSC cell to cover the voltage requirements of the PESC under consideration. A similar system was investigated by Kim *et al.* with the tandem cell having the modified artificial leaf configuration of Fig. 28a.³⁵⁶ In a 1 M H₂SO₄ electrolyte the onset of photocurrent was 0.6 V/RHE. The unbiased tandem cell achieved a current density of 0.4 mA cm⁻² under irradiation with a 150 W Xe lamp-based solar simulator, which increased to above 2 mA cm⁻² under additional bias voltage.

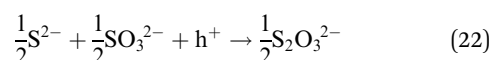
Arakawa *et al.* investigated a tandem system with a WO₃-based PESC in series with two DSSCs; the sensitizer was a Ru(terpyridine)(SCN)₃-based dye, known as “black dye”, with significant absorption in the NIR of the solar spectrum. The energy conversion efficiency was 2.6% under simulated solar light irradiation.³⁵⁷ A tandem system with a Fe₂O₃-based PESC and two DSSCs, with chromophores having complementary light absorption spectra, has been proposed by Brillet, Cornuz *et al.*³⁵⁸ One of these dyes was the well-known sensitizer N749, of the Ru(bpy)₃(SCN)₂-type, and the other a squaraine-type dye (SQ1).³⁵⁹ The tandem Fe₂O₃/SQ1 dye/N749 dye illuminated from the Fe₂O₃ side produced an energy storage efficiency of 1.36%.

Brillet *et al.* investigated a tandem cell based on WO₃ or Fe₂O₃ as a PESC photoelectrode in series with a DSSC based on a cyclopentadithiophene-bridged charge-transfer organic metal-free dye (Y123) and a Co(bpy)₃-type complex as a redox mediator.³⁶⁰ This type of DSSC was seen to exhibit higher photovoltages, approaching 1 V at open-circuit, than cells with I⁻/I₃⁻ as the mediator. Their configuration was analogous of the modified artificial leaf in Fig. 28a and 29. In sum, the cell configuration was

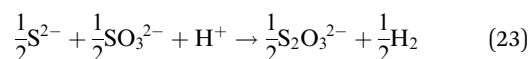


where 1 was short-circuit connected to 1* and 2 to 2*. INS indicates a transparent insulating phase (*i.e.* glass) separating the PE_{DSSC} layer from the electrolyte wetting the CE_{PESC}. The EL_{PESC} was 1 M NaOH for the Fe₂O₃ and 1 M HClO₄ for the WO₃ photoanode. Under irradiation of a 450 W Xe lamp with appropriate filters to simulate sunlight, a η_{st} of 3.1% and 1.2% was obtained for the WO₃- and the Fe₂O₃-based system, respectively, with respective photocurrents for the tandem connection of 3.1 and 1.2 mA cm⁻², respectively.

(b) CdS quantum dots on TiO₂. An alternative photoelectrode option is that of a TiO₂ electrode decorated with CdS quantum dots which is coupled to a H₂-evolving dark electrode. This electrode operates with a sulfur-based sacrificial donor system. The related photoelectrode reaction is



and the overall PEC reaction is



with a standard free enthalpy of 0.21 eV per absorbed photon. This system was studied by Gonzales-Pedro *et al.* and by Shin *et al.* in the tandem PESC/DSSC configuration.^{361,362}

In the study of Gonzales-Pedro *et al.* CdS dots were deposited on colloidal TiO₂, with the additional feature of a ZnS overlayer. The light source on the PESC was a Xe lamp providing 100 mW cm⁻² light, and the aqueous electrolyte composition was 0.25 M Na₂SO₃-0.35 M Na₂S. The DSSC was fabricated with a N719 sensitizer and a I⁻/I₃⁻ mediator in an acetonitrile-based electrolyte. The cell configuration is depicted in Fig. 28a. For the tandem system η_{st} was 0.8%, based on the free energy of the overall reaction as stated above, and the corresponding current density was 3.8 mA cm⁻². These values compare very favourably with η_{st} = 0.3% and short-circuit current of 1.6 mA cm⁻² for the stand-alone short-circuited PESC.

In the study of Shin *et al.* the substrate was in the form of a TiO₂ nanorod array; both the PESC cell electrolyte and the DSSC was the same as in the report by Gonzales-Pedro *et al.* The cell configuration is shown in Fig. 28b, with a double-side-coated TCO plate supporting both the PESC photoelectrode and the DSSC CE layer. A short-circuit photocurrent of 5.5 mA cm⁻² was

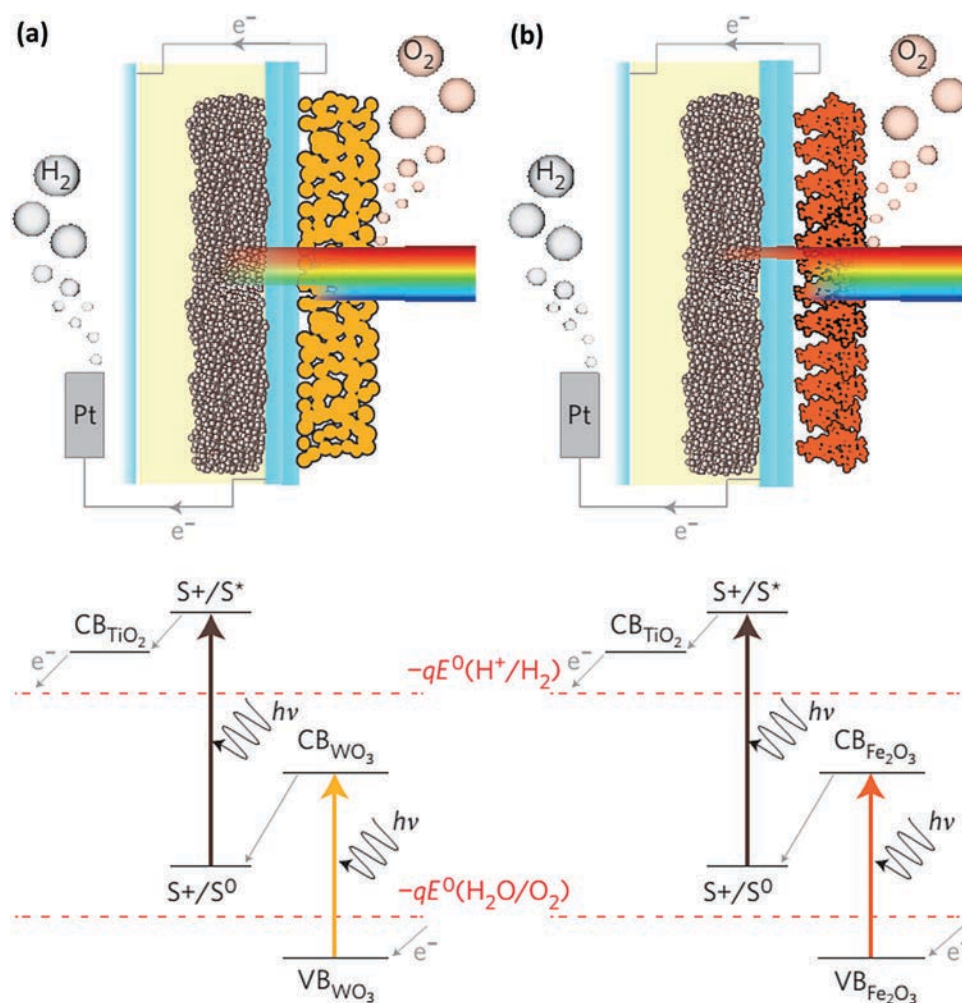


Fig. 29 Schematic of the tandem DSSC/PESC coupled cells with (a) WO₃ and (b) Fe₂O₃ photoanode. Reproduced with permission from ref. 360. Copyright 2014 Wiley-VCH.

generated. The DSSC was based on the N719 sensitizer and the I^-/I_3^- mediator in an acetonitrile-based electrolyte.

(c) **BiVO₄/WO₃**. In the article by Shi *et al.*³⁶³ the photoelectrode of a PEC generating hydrogen and oxygen was a BiVO₄/WO₃ bilayer electrode, with the BiVO₄ layer generated on top of a previously deposited WO₃ on TCO. Additionally, a FeOOH–NiOOH oxygen evolving catalyst was overlaid. The configuration was that of Fig. 28b, with a double-coated TCO plate supporting both the PESC composite photoelectrode and the DSSC CE layer. The PESC electrolyte was 0.5 M Na₂SO₄ at pH = 7 fixed with phosphate buffer. The DSSC was based on a donor–acceptor metal-free chromophore (JK-306) and a Co(bpy)₃-based redox mediator-containing electrolyte. Under illumination by a solar simulator, a η_{st} of 5.7% was obtained for the tandem cell corresponding to a short-circuit photocurrent of 5.7 mA cm⁻².

(d) **PESC coupled to DSSC**. As already discussed previously, PESCs based on direct semiconductor excitation usually require an additional external bias voltage for efficient operation, which can be supplied by an electricity-generating DSSC placed in series. Two related studies have been published by Sherman, Bergkamp *et al.*³⁶⁴ and by Sherman, Sheridan *et al.*³⁶⁵

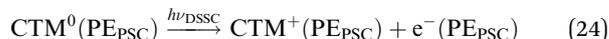
In the article by Sherman, Bergkamp *et al.* the electron-donating reaction at PE_{PESC} is not oxygen evolution but the oxidation of hydroquinone (H₂Q) to benzoquinone (BQ). The PESC electrolyte was 0.1 M Na₂SO₄ buffered at pH = 5.8 with Na₂SiF₆ containing 20 mM H₂Q in the PE compartment while the photoelectrode and CE compartments were separated by a Nafion ion-exchange. With regard to photooxidation, $E_F(H_2Q/BQ)$ was seen to be higher by 0.15 eV compared to $E_F(H_2O/O_2, H^+)$ at pH = 5.8. The chromophore of the PE_{PESC} was a metal-free porphyrin attached onto SnO₂ *via* –COOH. The DSSC was based on a Si-centered porphyrin on TiO₂ attached *via* –COOH, and the

I^-/I_3^- mediator in an acetonitrile-based electrolyte. The tandem cell configuration is depicted in Fig. 30, analogous to Fig. 28a, with the difference that light is directed to the glass side and not the electrolyte side of the photoelectrode while the DSSC is placed between PE_{PESC} and CE_{PESC}.

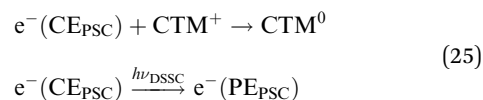
In the article by Sherman *et al.*, as indicated in Fig. 30, the PE_{PESC} reaction was O₂ evolution. The chromophore was a Ru(bpy)₃-based complex attached *via* the phosphonated groups on TiO₂. The substrate of PE_{PESC} was of the SnO₂ and TiO₂ core–shell configuration. The catalyst for O₂ evolution was of the (bipyridine)bis(isoquinoline)Ru-type, electrodeposited onto the PE_{PESC}. In the DSSC two dye–mediator combinations were considered: N719 sensitizer with the I^-/I_3^- mediator in an acetonitrile-based electrolyte and a metal-free donor–acceptor organic dye (D35) with a Co(bpy)₃ mediator, also dissolved in acetonitrile. The same configuration as used by Sherman, Bergkamp *et al.*, as depicted in Fig. 30 (upper part), was employed.³⁶⁴ Under white-light illumination of 100 mW cm⁻², H₂ evolution was detected in both cases; however, η_{st} was below 0.1%.

4.2. PSC/PESC coupled cells for H₂ evolution

For the description of tandem systems involving PSCs two options can be distinguished. On the one hand, a PSC can be coupled with a PESC in need of an external bias potential. On the other hand, one or, usually, two perovskite cells can provide the voltage needed for the operation of an electrolysis with dark electrodes (not needing illumination for their operations). In this respect, several equations discussed earlier in this section with respect to the photoelectrochemical DSSC applications can be applied, with dye (D) replaced by perovskite in the kinetic equations; the overall equation at the PE will be



where CTM is the charge-transport medium, alternatively denoted as the hole conductor. The subscript PSC now replaces DSSC, and correspondingly, the CE and overall PSC reactions are expressed as



The above formalism applies to all PSCs mentioned in this section apart from one case, based on the inverted planar architecture. The latter system is kinetically analogous to the p-DSSC described previously. The essential features of the tandem PSC-based systems appearing in the literature are presented below, classified according to the type of the PESC coupled to the PSCs.

(a) **PESC based on n-BiVO₄ and n-BiVO₄-composites**. The most efficient system in this category was reported by Qiu *et al.* As illustrated in Fig. 31a, the tandem PSC/PESC cell consists of separate PESC and PSC cells connected by cables. The PE_{PESC} was a specially structured Mo-doped BiVO₄ layer deposited on top of a SnO₂/SiO₂ truncated microcone substrate layer.³⁶⁶ The

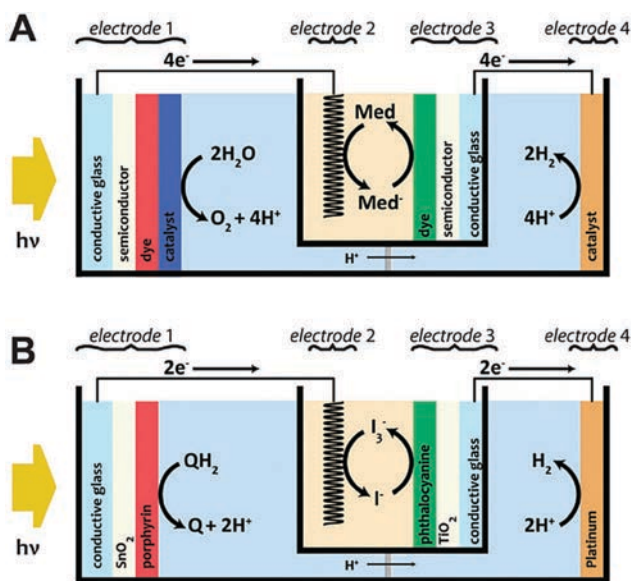


Fig. 30 Schematic of the tandem DSSC/PESC coupled cells consisting of a DSSC and a PESC with back irradiation of the PESC photoelectrode. Reproduced with permission from ref. 364. Copyright 2014 Wiley-VCH.

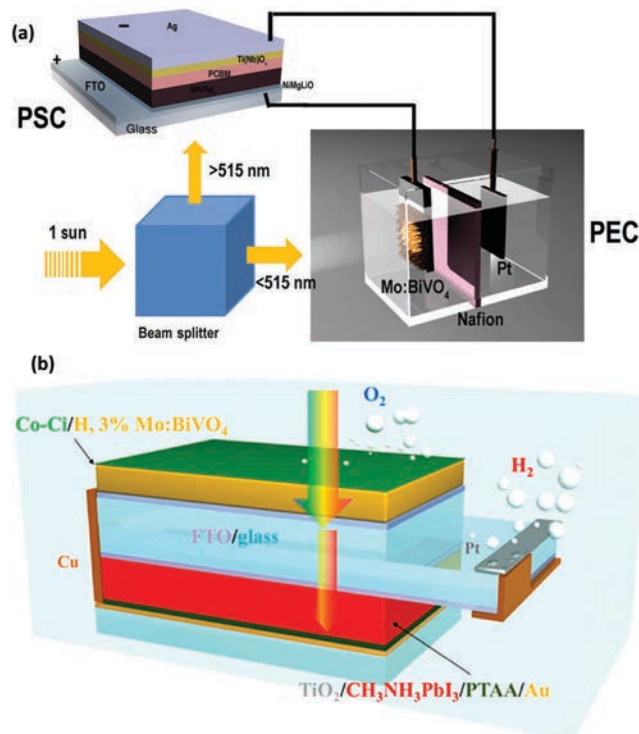


Fig. 31 (a) Schematic of the configuration of the PSC/PESC tandem cell. Reproduced with permission from ref. 366. Copyright 2016 AAAS. (b) Schematic of the tandem PSC/PESC coupled cell based on an n-PESC coupled to a PSC. Reproduced with permission from ref. 367. Copyright 2015 ACS.

latter substrate was generated by first creating a SiO₂ layer on FTO and then covering it with a thin SnO₂ coating. This particular electrode structure facilitates the separation of photo-generated electrons and holes. A Fe(Ni)OOH O₂-evolution catalyst was deposited on top of Mo-BiVO₄ while the CE was Pt. In a 0.5 M (pH = 7) phosphate buffer electrolyte, the maximum photocurrent for the PE_{PESC} at 1.23 V_{RHE} was 4.3 mA cm⁻² under simulated AM1.5 irradiance. The PSC was employing the inverted (p-i-n) planar device architecture, based on CH₃NH₃PbI₃ as the photoactive material, which is connected on the one side to NiMgLiO as the hole-accepting contact and on the other side to a PC₆₁BM layer as the electron-acceptor CTM, with the configuration of glass/FTO/NiMgLiO/CH₃NH₃PbI₃/PCBM/Ti(Nb)O_x/Ag. This type of PESC is different from the ones described in the rest of this section by the fact that it is based on a CTM of the electron-conductor rather than the hole-conductor type.

The incident simulated AM1.5 beam was divided by a beam splitter into two portions, each appropriate to the cell to which it is directed, with wavelength below 515 nm for the PESC and above 515 nm for the DSSC. The energy storage efficiency was 6.2% corresponding to a maximal operating current density for the tandem cell $j_{\text{ph(tandem)}} = 5.01 \text{ mA cm}^{-2}$. The $j_{\text{ph(tandem)}}$ is the current density obtained by series-connecting the PESC and PSC, without any external resistance in the circuit, and corresponds to the intersection of the DSSC and the PESC current-voltage curves.

Two other systems in the 3–5% efficiency range were investigated by Baek *et al.*³⁶⁸ and by Kim *et al.*³⁶⁷ In the former report, the PESC was based on a triple-junction BiVO₄/WO₃/WO₃ + SnO₂ triple-layer planar heterojunction (TPH) photoanode (PE_{PESC}) for O₂ evolution and a Pt CE for H₂ evolution. The PE_{PESC} was constructed by first depositing a porous SnO₂ layer and then a WO₃ layer penetrating into the pores of the SnO₂ layer. The amount of WO₃ was adjusted so that an overstanding layer was formed above the mixed layer WO₃ + SnO₂ layer. Finally, a BiVO₄ layer was added on top of the WO₃ + SnO₂ layer. The TPH layer was covered with a cobalt oxide-based (CoO_x) catalyst for O₂ evolution. The electrolyte was 0.5 M phosphate buffer at pH = 7. In the PSCs, the photoelectrode was based on the CH₃NH₃PbI₃/mp-TiO₂/ul-TiO₂/TCO, with mp-TiO₂ denoting the mesoporous TiO₂ support, ul-TiO₂ denoting the TiO₂ ultrathin compact layer (blocking layer or underlayer), and TCO the transparent conducting oxide support. The CTM was spiro-OMeTAD and the CE_{PSC} was an Au layer. Hence, this PSC configuration will be termed the “standard configuration”. The tandem cell comprising one PSC cell in series with the PESC cell was based on the configuration in Fig. 28a. Under simulated AM 1.5 irradiation at 100 mW cm⁻², a $j_{\text{ph(tandem)}}$ of 3.1 mA cm⁻² and an energy storage efficiency (O₂) of 3.5% were obtained (being based on evolved oxygen measurement energy storage efficiency (O₂) and accounting for the lower than unity faradaic efficiency). An alternative configuration with the single PSC cell being replaced by two smaller area PSCs in series gave a higher $j_{\text{ph(tandem)}}$ of 3.9 mA cm⁻² and energy storage efficiency (O₂) of 4.5%.

In the system by Kim *et al.*³⁶⁷ the photoelectrode was a dual-doped BiVO₄ (H₂-treated and Mo-doped) coated with a Co catalyst, which was Co carbonate (Co-Ci) in the most efficient system. Two different configurations were used: the wireless, compact-type, with the CE_{PESC} placed adjacently to PE_{PESC}, as indicated in Fig. 28a, or the wired type, with CE_{PESC} connected by an external long cable to PE_{PESC}, as shown in Fig. 31b. The PSC was of the standard configuration apart from the fact that the CTM was poly-triarylamine (PTAA) in the place of spiro-OMeTAD. For the wireless configuration and the wired configuration, energy storage efficiencies of 3.0% and 4.3% were obtained under simulated one sun illumination, with the latter improvement being due to the lower ohmic resistance in the wired configuration.

Chen *et al.*³⁶⁹ presented a similar system with a photoelectrode based only on BiVO₄, coated by a cobalt phosphate-based (CoPi)O₂-evolution catalyst. The electrolyte was 0.1 M phosphate buffer and the configuration was analogous to Fig. 28a. The PSC was of the standard configuration. Under simulated AM1.5 irradiation, an energy storage efficiency of 2.5% was achieved.³⁶⁸ In the publication by Zhang *et al.*³⁷⁰ the PE_{PESC} was based on a TiO₂ and BiVO₄ core-shell construction, with BiVO₄ surrounding an array of TiO₂ nanotubes. The cell configuration was analogous to Fig. 28a. The electrolyte was 0.1 M phosphate-buffer-saline (PBS, based on H₂PO₄⁻/HPO₄²⁻ and Cl⁻) at pH = 7. In the PSCs the photoelectrode was based on the CH₃NH₃PbI₃/TiO₂ configuration without the addition of a CTM and with a carbon layer CE_{PSC}. The perovskite material played the role of a hole

conductor. An Al_2O_3 layer was interposed between PBS at pH = 7. In the PSC the photoelectrode was based on the $\text{CH}_3\text{NH}_3\text{PbI}_3$ and carbon CE so as to prevent photoinjected recombination. Under simulated AM1.5 irradiation, an energy storage efficiency of 1.4% was achieved for the tandem device.

(b) PESC based on n- Fe_2O_3 . In the publication of Gurudayal *et al.* the PE_{PESC} was hematite in the form of NWs deposited on FTO glass, both in the undoped and the Mn-doped state.³⁷¹ The cell configuration was analogous to Fig. 28a, with a Pt electrode placed far away from the tandem assembly. The PSC was of the standard configuration ($\text{CH}_3\text{NH}_3\text{PbI}_3$ -spiro-OMeTAD-Au). In a 1 M NaOH electrolyte (pH = 13.6) under simulated AM1.5

irradiation of 100 mW cm^{-2} the tandem assembly achieved a η_{st} of 2.4% for the Mn- Fe_2O_3 PESC variant.

(c) PESC based on p- Cu_2O . Dias *et al.* tested a tandem system consisting of a p-type PESC and a PSC, connected as indicated in Fig. 32.³⁷² The PESC was based on a p- Cu_2O photocathode and a dark IrO_2 oxygen evolution anode. The PE_{PESC} was of a quite elaborate construction, with thin metal underlayer and several overlayers, *i.e.* FTO/Au/p- Cu_2O /Al:ZnO/ TiO_2 /RuO₂/Electrolyte, to ensure optimal electrocatalytic activity toward H_2 evolution together with protection from corrosion. The PSC was of the standard configuration. In a 0.5 M Na_2SO_4 and 0.1 M phosphate (pH = 5) electrolyte under simulated AM1.5

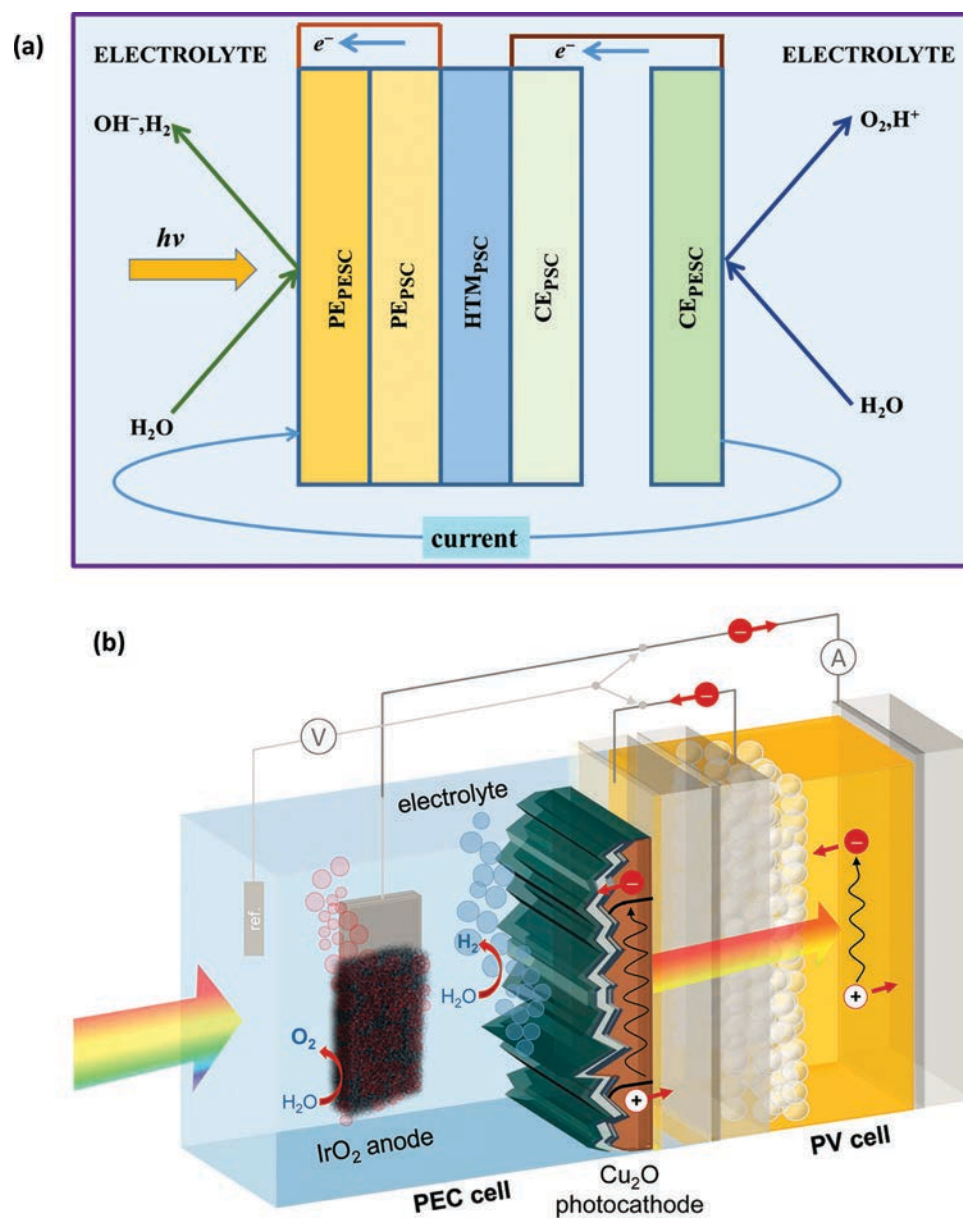


Fig. 32 (a) Schematic of the tandem PESC/PESC coupled cell, with a p-type photocathode of a PESC placed adjacently to the photoelectrode of a PSC. This configuration is analogous to that depicted in Fig. 28a, but with different interelectrode connections. (b) Schematic of the PESC/PESC coupled cell with a Cu_2O -perovskite- IrO_2 tandem cell during operation. Reproduced with permission from ref. 372. Copyright 2015 Wiley-VCH.

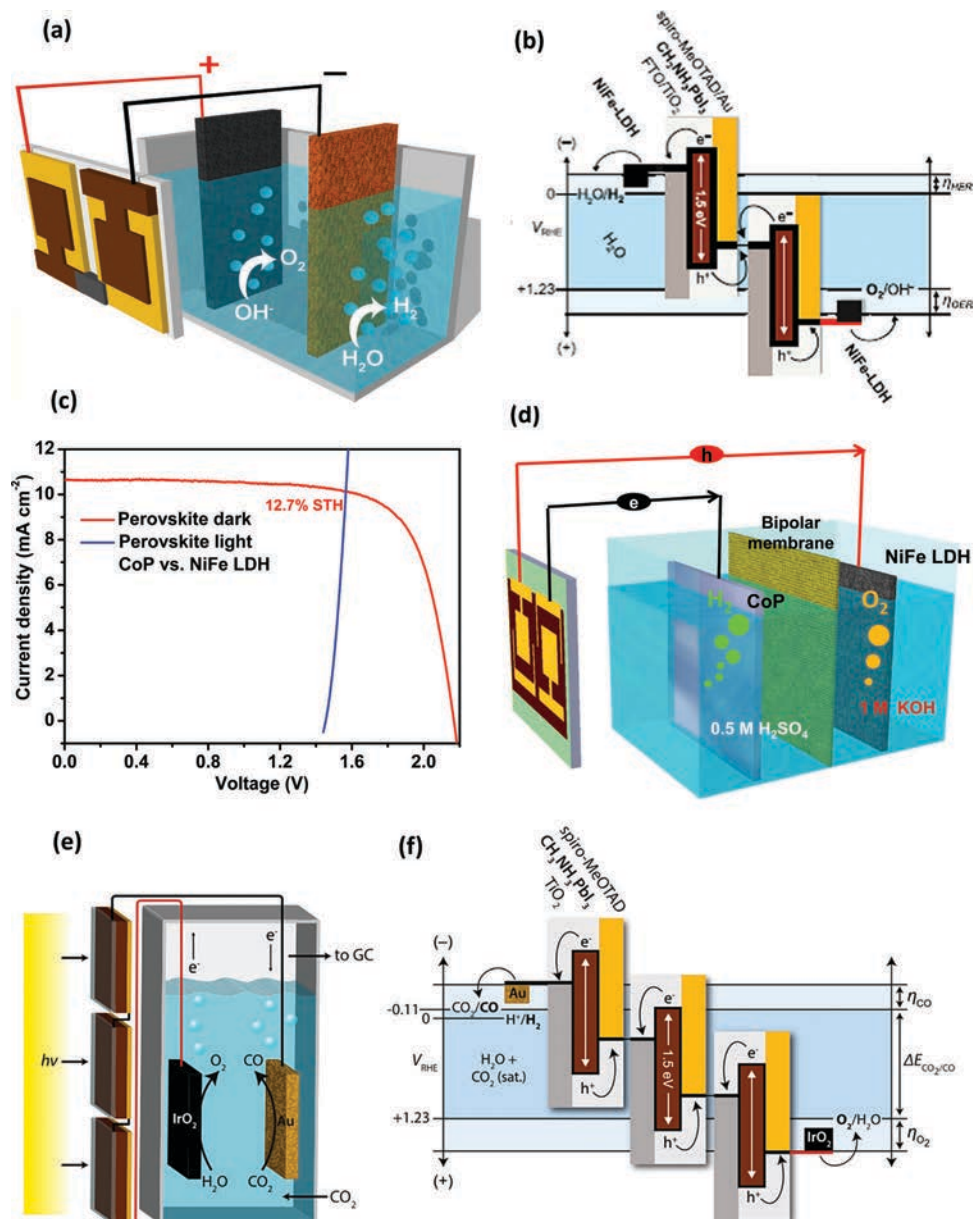


Fig. 33 (a) Schematic of the PSC/ELC coupled cell with NiFe LDH/Ni foam electrodes for H₂ evolution. (b) A generalized energy schematic of the PSC/ELC coupled cell with two PSCs. (c) *J*-*V* curves of the PSC/ELC coupled cell in the dark and under simulated AM 1.5G 100 mW cm⁻² illumination, and the NiFe/Ni foam electrodes in a two-electrode configuration. Reproduced with permission from ref. 136. Copyright 2014 AAAS. (d) Schematic diagram of the PSC/ELC coupled cell composed of perovskite light harvesters, earth-abundant catalysts, and a bi-polar membrane. Reproduced with permission from ref. 373. Copyright 2016 Wiley-VCH. (e) Schematic of the PSC/ELC coupled cell with three PSCs. (f) Generalized energy diagram for converting CO₂ into CO with three PSCs. Reproduced with permission from ref. 374. Copyright 2015 NPG.

irradiation of 100 mW cm⁻² the tandem assembly yielded a η_{st} of 2.4% and a corresponding $j_{ph(tandem)}$ of 2 mA cm⁻².

4.3. PSC/ELC coupled cells for H₂ evolution and CO₂ reduction

(a) **Water electrolysis.** In contrast to the cases discussed up to now, the following section involves the coupling of PSCs and electrolysis cells (ELCs) with two dark electrodes or PSCs. The system of Luo *et al.*¹³⁶ consisted of an alkaline (1 M NaOH OH) water ELC coupled to two series-connected PSCs based on the

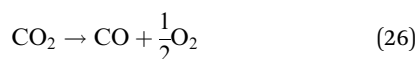
CH₃NH₃PbI₃-Spiro-OMeTAD-Au configuration (Fig. 33a-c). The catalytic electrodes of the ELC consisted of earth abundant materials, *i.e.* Ni foam for H₂ evolution and Ni-Fe-layered double hydroxide (NiFe LDH) for both hydrogen and oxygen evolution.

Luo *et al.*³⁷³ studied the coupling of two PSCs and a ELC with electrocatalysts based on two compartments, separated by a bipolar ion-exchange membrane (*i.e.* a cation-exchange membrane laminated together with an anion-exchange membrane) with 0.5 M H₂SO₄ for the H₂-evolution electrode and an alkaline

solution 1 M KOH for the O₂-evolution electrode, as illustrated in Fig. 33d. The particular reason for use of this electrolyte and separator is as follows: H₂SO₄ is useful for H₂ evolution whereas KOH is useful for O₂ evolution, and thus result in the long-term stability of both electrodes. In fact several earth-abundant electrocatalysts for H₂-evolution are seen to be unstable in bases, as is the case with the cobalt phosphate (CoP) used in the present case. Similarly, the stability of several earth abundant electrocatalysts for O₂ in acids is problematic, as seen for the NiFe LDH used in the present case.

The PSCs were based on MAPbBr₃-stabilized FAPbI₃ perovskite phase light harvester ((FAPbI₃)_{1-x}(MAPbBr₃)_x). Under simulated AM 1.5G irradiation a η_{st} of 12.7% was obtained (Fig. 33c), corresponding to a $j_{\text{ph(tandem)}}$ of 10.33 mA cm⁻². Under this current, the ELC operated at 1.6 V while the thermodynamic potential of the cell in the absence of liquid-junction potential was 0.40 V, with the major part of the total cell overpotential appearing across the membrane.

(b) CO₂ reduction. The reduction of CO₂ to CO was studied by Schreier *et al.* in a tandem ELC-PSC system, as illustrated in Fig. 33e and f.³⁷⁴ The electromotive force (emf) of the reaction



is 1.34 V, as compared to the 1.23 V emf for water decomposition to H₂ and O₂. This corresponds to an electrode potential of -0.11 V/RHE for the half-reaction



However, the overpotential for the above reaction is substantial so that three PSC are required for the ELC. The latter was composed of a porous Au cathode for CO₂ reduction and an IrO₂ anode for O₂ evolution in a CO₂-saturated NaHCO₃ electrolyte. A tandem cell constructed this way produced a $j_{\text{ph(tandem)}}$ of 5.8 mA cm⁻². The faradaic efficiency for CO generation was 80–90%, with the formation of H₂ as by-product accounting for the rest. On the basis of the aforementioned 1.34 V emf for CO generation, η_{st} lies in the range 6–7%, or above 7% including H₂ generation in the storage efficiency calculation.

5. Summary and future outlook

General summary and outlook

The present Review has summarized the recent progress in integrated solar cells based on DSSCs and PSCs for energy harvesting/conversion and storage. Researchers have designed different integrated devices for PV power generation and storage systems by using various technologies and materials. However, this field is still at a very early stage. For example, the J_{sc} and V_{oc} of an integrated device are strongly affected by the band structure and the surface/interface characteristics of the connected PV unit. The solar cells, however, require operation at the maximum power point to make full use of the incident light. In addition, the photon-charge formation is a dynamic process. In this regard, it is better to introduce a smart power-conversion unit into the integrated device, which could

extract more power from solar cells to be stored in the energy storage devices.

The revolutionary new technologies of generating usable energy from sustainable and non-polluting sources must have the flexibility to meet the energy demands of both consumers and users, while producing fewer carbon emissions than current energy systems. With regard to new-generation integrated solar cell devices comprising alternative PV technologies, improvements of DSSCs and PSCs in performance, durability, and scalability play a critical role in order to meet the high quality demand of the market. Continued research in that direction will enhance the production and sales of durable and highly efficient integrated solar cell devices in the future.

There is large interest in integrating solar cells in buildings utilizing their different colors, shapes, and transparencies to provide a competitive edge for this new-generation integrated solar energy technology. To promote the use of large-scale DSSCs in integrated systems in the future, new ionic liquid electrolytes (ILEs) have to be developed to achieve higher PCEs and provide the high stability and transparency that is greatly demanded for BIPV applications. Novel solid-state ILEs comprising gel-binding agents and inorganic nano-fillers will ascertain market prospects for large scale applications in the electric power generating glass panels. To meet the efficiency demand for DSSCs in commercial application, a J_{sc} of 20 mA cm⁻² is expected to be achieved and maintained by controlling and modifying the pore size, quantity, and shape of the novel nanostructured TiO₂ films that are used in conjunction with improved ILEs. To respond to the commercial demand for DSSC panels in specific colors (in particular green and blue), a novel class of high-stability and low-cost sensitizers, such as ruthenium complexes, blue organic dye, and green porphyrin dye, need to be designed and explored. Additionally, new alternative materials should meet the expectation of both lower cost and long-lived population of charge carriers that is required to reach the ambitious cell efficiency goals. The practical application and large-area fabrication for each material in DSSC and PSC will face many great challenges in future.^{5,375–377}

A tremendous advance in PCE for the PSCs has been made, reaching a current certified level of 22.1% that has stunned the PV community. Nevertheless, this path-breaking PV technology is still in its infancy and there remains a big challenge of long-term stability. To date, the instability of PSCs has posed a hurdle for implementation and commercialization. The main source of instability for PSCs was found to stem from the degradation of MAPbI₃ perovskite materials. The release of volatile iodine vapor was found to be inevitable for PSCs in practical applications due to their subjection to moisture, oxygen, light illumination, thermal stress, and applied electric fields. In addition, the use of toxic Pb is still a big problem for PSCs. Therefore, alternative perovskite materials need to be explored to achieve long-term stable PSCs that are considerable for practical applications.

In general, integrated devices based on DSSC and PSC technology have the potential to excel through a myriad of inherent advantages such as low-temperature and low-cost

processing, mechanical flexibility and choice of rigid or flexible substrate, low-toxicity (in the case of DSSCs), excellent low-light performance, and tunability of color and transparency. It can be expected that taking advantage of the above properties will enable exciting novel integrated products and applications as well as wide-spread use of the technology.

Integrated tandem devices

The benefit of using wide-bandgap PSCs as top cells in integrated solar devices becomes increasingly enticing. Integrated tandem devices with silicon bottom cells and PSC top cells have resulted in up to 26.4% efficiency, close to the single junction silicon record of 26.6%.^{6,199–201} For monolithic devices, silicon bottom cells are often adjusted to accompany PSC top cells, thereby reducing their performance. Novel means of light trapping structures and passivation layers need to be explored that are compatible with the tandem architecture. Most reports to date have focused on high PCE HJT and PERC cells while the biggest economic advantage and impact might arise from the combination of perovskites with the market-leading polycrystalline Si technology, which should therefore receive more research focus. The limitation of silicon's bandgap to 1.12 eV further demands the improvement of wide-bandgap perovskite compositions around 1.7–1.8 eV, which can be achieved by the addition of bromide.⁹⁴ The long lifetime of commercial silicon modules under operating conditions will have to be met by perovskite top-cells to allow for the market entry of integrated PSC/silicon tandem devices.

The combination of PSCs with thin film chalcopyrite bottom cells is particularly promising due to the tunability of the chalcopyrite's bandgap to values as low as 1.0 eV, which is not possible with silicon. Moreover, both chalcopyrite and perovskite absorbers can be fabricated on flexible substrates with low-cost solution methods which could facilitate roll-to-roll processing of flexible, monolithically integrated tandem modules. Efficiencies of up to 22.1% have been reported to date for integrated CIGS/PSC tandem devices, which is already close to the CIGS single-junction record efficiency at 22.6%.^{222,245} Further performance improvements and/or the use of economical deposition methods will be needed, however, to justify the additional cost and effort for the tandem fabrication. Albrecht *et al.* recently projected that tandem devices with Si or CIGS bottom cells could reach 30% PCE in 2020 and 35% by 2030, which would change the economics for these devices.

Attention has also been directed to the fabrication of CIGS absorbers *via* low-cost solution deposition methods and use of flexible substrates which could further reduce module costs as well as capital expenditure of new manufacturing plants by enabling roll-to-roll printing methods.^{223,226,378} In terms of tandem performance, further research should be focused on the improvement of low-bandgap CuInSe₂-based devices that are predicted to lead to highest theoretical tandem efficiencies when used as bottom cells with high efficiency PSCs.^{229–231} Earth-abundant alternatives to CIGS might also be explored, such as low-bandgap Cu₂ZnSnSe₄ kesterite absorbers.³⁷⁹ Other topics of interest for the realization of monolithic devices are

the improvement of high-PCE perovskite top-cells in inverted architecture and substrate configuration, the reduction of PSC processing temperatures, and the planarization of CIGS devices. Before a commercial implementation can be achieved, however, crucial points for the top cell have to be addressed such as long-term stability of PSCs or the technology's feasibility for large-scale processing.

Integrated all-perovskite tandem cells have a tremendous low-cost potential due to their thin film nature that enables monolithic integration and flexible substrates, ability to use solution methods with high material yield and low thermal budget, and ease of manufacturing. The integrated PSC/PSC tandem devices have achieved up to 20.3% stabilized power output, approaching the technology's single junction record at 21.7%.^{233,380} The development of low-bandgap perovskite absorbers down to 1.2 eV is still very recent and should trigger further improvements in device efficiency and even lower bandgap compositions that are more optimal for bottom devices. The large tunability range of the perovskite bandgap from 1.2–2.3 eV should further be exploited to realize multi-junction tandem devices with three or more junctions for efficiencies over 50%.^{229,381} High PCE tandem devices in the substrate configuration might enable flexible tandem devices on opaque or low transmittance metal or polymer foils.

In contrast to SSCs, whose production is comparatively expensive due to the technology's high energy and material demand, the use of DSSC and PSC based devices could allow for a more efficient fabrication and decrease costs significantly. Additional benefits of the DSSC and PSC technology arise under low light conditions. While the J_{sc} of typical solar cells is reduced under weak-light illumination, thin film solar cells such as PSCs and DSSCs possess improved PCE retention compared with their silicon counterpart. This in turn, however, might lead to challenges in current-matched tandem devices. As a result, more research should be focused on real operation conditions when designing tandem devices or multi-junction solar cells.

Integrated energy harvesting and storage devices

With the continuing development of PV and energy storage devices, the integrated devices are expected to feature some exciting new breakthroughs. Different energy storage devices could be widely integrated with PV to simultaneously realize the energy harvesting/conversion and storage and utilization. In terms of energy storage units, SCs exhibit high power densities while LIBs show high energy densities, which allow the integrated energy storage side to be configured for different applications. It should be noted that the operating voltage of a LIB is generally constant while the voltage of a SC will mostly change during the charge and discharge process, which can add difficulty when improving the efficiency of the whole device. The revised strategy therefore needs to be targeted towards circuit and device to achieve constant voltage charging and discharging for the SC unit. Moreover, the energy storage components are not limited to SC and LIB, as discussed in this Review, and other exciting types of energy storage devices, such as sodium-ion

batteries, zinc–air batteries, *etc.*, are heavily researched in the integrated solar cell systems.

To date, the majority of integrated photo-energy conversion and energy storage integrated devices have been based on DSSC and PSC technologies. The integration of DSSC/SC device has reached the highest efficiency of 5.12% by using CNTs as CEs. Other combinations of PV systems with storage systems also show the high potential of this area of research. In particular, the emergence of the PSCs has garnered considerable attention. It is noteworthy that the theoretical overall output efficiency of an integrated device (PSC/SC) can reach 20% with an output voltage of 1.46 V when the voltage of the SC is set at 0.6 V.³²¹ PSCs are envisioned to be a great substitute for DSSCs due to their low processing cost and high efficiencies. Additionally, SCs can also be improved by integration with organic radical batteries, resulting in a fast charging, high capacity storage device. In terms of integrated systems, a four-electrode setup is a good means to optimize the solar re-chargeable SCs, as the solar cell and the SC part can be improved separately. Despite vast optimization requirements, solar-rechargeable energy storage systems based on DSSCs and PSCs have a high potential for efficient and direct storage of solar energy due to their inherent advantages compared to common inorganic devices such as exceptional low-light performance which enables use for indoor applications, and tunability of color and transparency which allows for the tailoring of the integrated device design to the customers' individual preference.

Vast success has been achieved in the field of portable electronics; however, traditional LIBs are encountering growing challenges in the emerging applications (*e.g.* smart grid) as well as in flexible/micro-electronics due to their relatively low energy and power densities. Alternative lithium–oxygen and lithium–sulfur batteries with higher specific energy density are promising but rely on the breakthrough of electrode materials, electrolytes, and the cell structure design. Integrated devices are capable of realizing multiple functions by combining different energy units. The integration of DSSCs or PSCs and LIBs allows for simultaneous energy harvesting and storage in a single device, while the integration of LIBs and SCs can provide electronics with both high energy and high power densities, which are of importance for small sized, lightweight, and high-density energy systems.

Regarding the integration of NGs and solar cells, two major fields of research are apparent. The first is how to use NGs or their mechanism to increase the PCE of solar cells. Three key steps can be distinguished during the conversion of photo-energy to electricity in a solar cell: the incidence of solar light onto the solar cell, the conversion of photons into electron–hole pairs, and the separation of electron–hole pairs to the two opposing electrodes. How to employ the voltage of NGs or the piezoelectric field to effectively separate the electron–hole pairs is a very important field of research, which can contribute to the enhancement of solar cells' PCEs. The second key research direction is how to effectively adapt integrated NGs and solar cells for different operating conditions to maximize the simultaneous harvesting of mechanical energy and solar energy. There

are four modes for TENGs, which are lateral sliding mode, single electrode mode, vertical contact mode, and freestanding triboelectric layer mode, and two modes for PENGs, which are uniaxial compression mode and lateral bent mode.³⁸² According to the specific operating condition, choosing the individual or complementary modes of the NG is also a very important field of research which can contribute to the overall system's power generation ability.

Many advances have been achieved by improving the architecture, stability, and performance of flexible integrated devices. However, there are still some critical problems that need further be overcome for their practical applications. First, the PCE of the employed solar cells can be further increased. Second, the sealing processes of typically used DSSCs to avoid electrolyte leaking during use can be further improved. Third, the scale-up production of integrated devices based on solar cells for practical applications still face a great challenge.

In general, integrated devices based on DSSCs exhibit a very poor performance, much smaller than the typical PCE value of DSSCs (*i.e.* 10%) due to the lack of optimization and match of cell components within the integrated devices. As mentioned above, future research of energy harvesting/conversion and energy storage devices (DSSCs, LIBs, SCs, NGs, *etc.*), improvements in the performance of the integrated units, through optimizing device architecture, substrates, materials design, matching, stability, tenability, cost, scalable manufacturing process, module, encapsulation, and *etc.*, are highly desirable for integrated devices based on DSSCs to increase PCEs beyond current levels to real applications.

Integrated photoelectrochemical cells

In the past ten years, dye-sensitized electrodes have attracted a lot of interest as photoanodes or photocathodes for electro-synthetic applications, mainly for hydrogen evolution, oxygen evolution, and CO₂ reduction, and usually in combination with catalysts. Despite the achieved substantial progress, the resulting photocurrents are substantially lower compared to those based on directly photoexcited semiconductors such as p-Cu₂O, n-Fe₂O₃, n-WO₃, and n-BiVO₄. A substantial challenge is the matching between the energy levels of dye ground and excited states, the semiconductor conduction band or valence band, and the energy levels of the molecules injecting holes or electrons into the photoexcited dye. Additionally, the involved complex, multi-electron reactions in solution involved requires the judicious choice of catalysts. Therefore, the progress of this field is intimately linked to advances in the molecular chemistry of reactions such as water oxidation to oxygen, water reduction to hydrogen, and CO₂ reduction. From the experimental point of view, an often encountered problem is the lack of standardization conditions for performing experiments, which would improve the comparison of results obtained by various laboratories. In particular, a variety of white or monochromatic light sources of intensity comparable to that of sunlight are used in addition to a multitude of solution compositions and pH values. Therefore, it is desirable that the same level of standardization is achieved as in the research on solar cells.

In conclusion, more fundamental research is needed in order to reach a definite conclusion about whether the direct dye-sensitized photoanode and photocathode option is viable and, upon decision, which particular system should be the focus of further optimization.

A further field of interest is that of tandem systems comprising electricity-producing DSSCs and either ELCs with dark electrodes or PESC s needing additional bias potential. In both cases a prerequisite for advancement is the further optimization of DSSCs with respect to all three goals: PCE in the 10–20% range, extended long-term stability, and manufacturing on the basis of earth-abundant, inexpensive and non-volatile materials. Alternatively, the recently emerged PSCs, exhibiting higher PCEs, approaching those of traditional solid-state inorganic solar cells, are attracting increased attention in tandem PESC research, in particular the field of water decomposition to hydrogen and oxygen, and CO₂ reduction. Provided that stability, low-price, and environment-compatibility criteria are fulfilled, PCEs could prove to be the solar cells of choice in chemical solar energy applications.

Abbreviations

AR	Antireflection	FA	HC(NH ₂) ₂ ⁺
ALD	Atomic layer deposition	FTO	Fluorine-doped tin dioxide
BQ	Benzoquinone	GNP	Graphene nanoplatelet
BHJ	Bulk-heterojunction	HTM	Hole-transporter materials
cb	Conduction band	HTL	Hole transport layer
CE	Counter electrode	HJT	Heterojunction technology
CNT	Carbon nanotube	H ₂ Q	Hydroquinone
CTM	Charge-transport material	IBC	Interdigitated back contact
CIS	CuIn(S,Se) ₂	ITO	Indium tin oxide
CIGS	CuInGaSe ₂	IZO	Indium zinc oxide
C ₆₀ -SB	Tris(sulfobetaine)-substituted fulleropyrrolidine	IEC	International electrotechnical commission
C ₆₀ -N	Tertiary amino-fulleropyrrolidine	<i>J</i> _{sc}	Short circuit current density
DPE	Diphenyl ether	LIB	Lithium ion battery
DSSC	Dye-sensitized solar cell	LED	Light emitting diode
n-DSSC	DSSC with n-type photoanode and dark counter electrode (cathode)	LATP	Li _{1.35} Ti _{1.75} Al _{0.25} P _{2.7} Si _{0.3} O ₁₂
p-DSSC	DSSC with p-type photocathode and dark counter electrode (anode)	LiTFSI	Lithium bis(trifluoromethane sulfonimide)
DMSO	Dimethyl sulfoxide	MA	CH ₃ NH ₃ ⁺
n-PESC	PESC with n-type photoanode and dark counter electrode (cathode)	MAPbI ₃	Methylammonium-lead iodide
p-PESC	PESC with n-type photocathode and dark counter electrode (anode)	NW	Nanowire
<i>E</i> _{cb}	Conduction band edge	NT	Nanotube
EQE	External quantum efficiency	NG	Nanogenerator
ELC	Electrolysis cell	NIR	Near-infrared
emf	Electromotive force	N2200	Poly[<i>N,N'</i> -bis(2-octyldodecyl)-naphthalene-1,4,5,8-bis(dicarboximide)-2,6-diyl]- <i>alt</i> -5,5'-(2,2'-bithiophene)
<i>η</i> _{st}	Energy storage efficiency	OSC	Organic solar cell
ETL	Electron transport layer	PE	Photoanode
EMIBF ₄	1-Ethyl-3-methyl imidazolium tetrafluoroborate	PC	Propylene carbonate
FF	Fill factor	PSC	Perovskite solar cell
		PEC	Photoelectrochemical cell
		PCE	Power conversion efficiency
		PBS	Phosphate-buffer-saline
		PEO	Polyethylene oxide
		PSS	Poly(styrenesulfonate)
		PPy	Polypyrrole
		PEI	Poly(ethyleneimine)
		PET	Polyethylene terephthalate
		PVA	Polyvinyl acetate
		P3HT	Poly(3-hexylthiophene)
		PESC	Photoelectrosynthetic cell
		PTFE	Polytetrafluoroethylene
		PMMA	Polymethylmethacrylate
		PVCS	Photovoltachromic supercapacitor
		PERC	Passivated emitter rear contact
		PENG	Piezoelectric nanogenerator
		PEDOT	Poly(3,4-ethylenedioxythiophene)
		PANI	Polyaniline
		PVDF	Poly(vinylidene fluoride)
		PDPP3T	Poly(diketopyrrolopyrrole-terthiophene)
		PC ₆₀ BM	[6,6]-Phenyl-C ₆₀ -butyric acid methyl ester
		PC ₆₁ BM	[6,6]-Phenyl-C ₆₁ -butyric acid methyl ester
		PC ₇₀ BM	[6,6]-Phenyl-C ₇₀ -butyric acid methyl ester
		PC ₇₁ BM	[6,6]-Phenyl-C ₇₁ -butyric acid methyl ester
		PProDOT-Et ₂	Poly(3,4-(2',2'-diethyl)-propylenedioxythiophene)
		QDSC	Quantum dot solar cell

SC	Supercapacitor
SEM	Scanning electron microscope
tBP	<i>tert</i> -Butylpyridine
TCO	Transparent conducting tin oxide
TPH	Triple-layer planar heterojunction
TENG	Triboelectric nanogenerator
UV-vis	Ultraviolet-visible
vb	Valence band
V_{oc}	Open circuit voltage
ZTO	Zinc tin oxide

Author contributions

S. Yun designed the outline of the review manuscript. S. Yun wrote the Abstract and Sections 1.1–1.4. A. R. Uhl wrote Sections 2.1–2.3. S. Yun wrote Section 2.4. X. Han wrote Section 3.1. Y. Qin wrote Sections 3.2 and 3.4. D. Li, M. Yin and S. Yun wrote Section 3.3. D. Li and M. Yin wrote Section 3.5. S. Yun, D. Li and M. Yin wrote Section 3.6. S. Yun wrote Section 3.7. N. Vlachopoulos, A. Hagfeldt and S. Yun wrote Sections 4.1–4.3. All authors wrote Section 5 Summary and future outlook. S. Yun and A. R. Uhl provided final revisions for all sections. All authors reviewed the manuscript and proof-read the final manuscript.

Conflicts of interest

There are no conflicts to declare.

Acknowledgements

Financial support from NSFC (51672208), Sci-Tech R&D Program of Shaanxi Province (2011JM6010 and 2015JM5183), and Shaanxi Provincial Department of Education (2013JK0927) is greatly acknowledged. The project was partly sponsored by SRF for ROCS, SEM. ARU acknowledges the financial support from the Swiss National Science Foundation (SNSF) under the project number P300P2_164660.

References

- M. Perez and R. Perez, *IEA-SHCP-Newsletter*, 2015, **62**, 1–4.
- R. Perez and M. Perez, *International Energy Agency SHCP Solar Update*, 2009, **50**, 1–3.
- D. M. Chapin, C. Fuller and G. Pearson, *J. Appl. Phys.*, 1954, **25**, 676–677.
- K. Yoshikawa, H. Kawasaki, W. Yoshida, T. Irie, K. Konishi, K. Nakano, T. Uto, D. Adachi, M. Kanematsu, H. Uzu and K. Yamamoto, *Nat. Energy*, 2017, **2**, 17032.
- A. Polman, M. Knight, E. C. Garnett, B. Ehrler and W. C. Sinke, *Science*, 2016, **352**, aad4424.
- M. A. Green, K. Emery, Y. Hishikawa, W. Warta, E. D. Dunlop, D. H. Levi and A. W. Y. Ho-Baillie, *Prog. Photovoltaics Res. Appl.*, 2017, **25**, 3–13.
- C. Grätzel and S. M. Zakeeruddin, *Mater. Today*, 2013, **16**, 11–18.
- M. Grätzel, *Acc. Chem. Res.*, 2017, **50**, 487–491.
- K. Kakiage, Y. Aoyama, T. Yano, K. Oya, J.-i. Fujisawa and M. Hanaya, *Chem. Commun.*, 2015, **51**, 15894–15897.
- X. Li, D. Bi, C. Yi, J.-D. Décoppet, J. Luo, S. M. Zakeeruddin, A. Hagfeldt and M. Grätzel, *Science*, 2016, **353**, 58–62.
- B. O'Regan and M. Grätzel, *Nature*, 1991, **353**, 737–740.
- M. Grätzel, *Acc. Chem. Res.*, 2009, **42**, 1788–1798.
- A. Hagfeldt, G. Boschloo, L. Sun, L. Kloo and H. Pettersson, *Chem. Rev.*, 2010, **110**, 6595–6663.
- M. Grätzel, *Nature*, 2001, **414**, 338–344.
- S. Yun, J. N. Freitas, A. F. Nogueira, Y. Wang, S. Ahmad and Z.-S. Wang, *Prog. Polym. Sci.*, 2016, **59**, 1–40.
- H. J. Snaith and L. Schmidt-Mende, *Adv. Mater.*, 2007, **19**, 3187–3200.
- T. Zhang, S. Yun, X. Li, X. Huang, Y. Hou, Y. Liu, J. Li, X. Zhou and W. Fang, *J. Power Sources*, 2017, **340**, 325–336.
- T. Zhang, Y. Liu and S. Yun, *Isr. J. Chem.*, 2015, **55**, 943–954.
- S. Yun, P. D. Lund and A. Hinsch, *Energy Environ. Sci.*, 2015, **8**, 3495–3514.
- S. Yun, Y. Liu, T. Zhang and S. Ahmad, *Nanoscale*, 2015, **7**, 11877–11893.
- S. Yun, H. Pu, J. Chen, A. Hagfeldt and T. Ma, *ChemSusChem*, 2014, **7**, 442–450.
- S. Yun, A. Hagfeldt and T. Ma, *Adv. Mater.*, 2014, **26**, 6210–6237.
- S. Yun, A. Hagfeldt and T. Ma, *ChemCatChem*, 2014, **6**, 1584–1588.
- S. Yun, H. Zhou, L. Wang, H. Zhang and T. Ma, *J. Mater. Chem. A*, 2013, **1**, 1341–1348.
- S. Yun, H. Zhang, H. Pu, J. Chen, A. Hagfeldt and T. Ma, *Adv. Energy Mater.*, 2013, **3**, 1407–1412.
- S. Yun, M. Wu, Y. Wang, J. Shi, X. Lin, A. Hagfeldt and T. Ma, *ChemSusChem*, 2013, **6**, 411–416.
- S. Yun, L. Wang, C. Zhao, Y. Wang and T. Ma, *Phys. Chem. Chem. Phys.*, 2013, **15**, 4286–4290.
- S. Yun, L. Wang, W. Guo and T. Ma, *Electrochem. Commun.*, 2012, **24**, 69–73.
- B. O'Regan and M. Grätzel, *Nature*, 1991, **353**, 737–740.
- C. J. Barbé, F. Arendse, P. Comte, M. Jirousek, F. Lenzenmann, V. Shklover and M. Grätzel, *J. Am. Ceram. Soc.*, 1997, **80**, 3157–3171.
- M. K. Nazeeruddin, F. De Angelis, S. Fantacci, A. Selloni, G. Viscardi, P. Liska, S. Ito, B. Takeru and M. Grätzel, *J. Am. Chem. Soc.*, 2005, **127**, 16835–16847.
- C. Yasuo, I. Ashraful, W. Yuuki, K. Ryoichi, K. Naoki and H. Liyuan, *Jpn. J. Appl. Phys.*, 2006, **45**, L638–L640.
- C.-Y. Chen, M. Wang, J.-Y. Li, N. Pootrakulchote, L. Alibabaei, C.-h. Ngoc-le, J.-D. Decoppet, J.-H. Tsai, C. Grätzel, C.-G. Wu, S. M. Zakeeruddin and M. Grätzel, *ACS Nano*, 2009, **3**, 3103–3109.
- Q. Yu, Y. Wang, Z. Yi, N. Zu, J. Zhang, M. Zhang and P. Wang, *ACS Nano*, 2010, **4**, 6032–6038.

- 35 L. Han, A. Islam, H. Chen, C. Malapaka, B. Chiranjeevi, S. Zhang, X. Yang and M. Yanagida, *Energy Environ. Sci.*, 2012, **5**, 6057–6060.
- 36 T. Horiuchi, H. Miura, K. Sumioka and S. Uchida, *J. Am. Chem. Soc.*, 2004, **126**, 12218–12219.
- 37 S. Ito, S. M. Zakeeruddin, R. Humphry-Baker, P. Liska, R. Charvet, P. Comte, M. K. Nazeeruddin, P. Péchy, M. Takata, H. Miura, S. Uchida and M. Grätzel, *Adv. Mater.*, 2006, **18**, 1202–1205.
- 38 S. Ito, H. Miura, S. Uchida, M. Takata, K. Sumioka, P. Liska, P. Comte, P. Pechy and M. Grätzel, *Chem. Commun.*, 2008, 5194–5196.
- 39 W. Zeng, Y. Cao, Y. Bai, Y. Wang, Y. Shi, M. Zhang, F. Wang, C. Pan and P. Wang, *Chem. Mater.*, 2010, **22**, 1915–1925.
- 40 A. Yella, R. Humphry-Baker, B. F. E. Curchod, N. Ashari Astani, J. Teuscher, L. E. Polander, S. Mathew, J.-E. Moser, I. Tavernelli, U. Rothlisberger, M. Grätzel, M. K. Nazeeruddin and J. Frey, *Chem. Mater.*, 2013, **25**, 2733–2739.
- 41 W. M. Campbell, K. W. Jolley, P. Wagner, K. Wagner, P. J. Walsh, K. C. Gordon, L. Schmidt-Mende, M. K. Nazeeruddin, Q. Wang, M. Grätzel and D. L. Officer, *J. Phys. Chem. C*, 2007, **111**, 11760–11762.
- 42 T. Bessho, S. M. Zakeeruddin, C.-Y. Yeh, E. W.-G. Diau and M. Grätzel, *Angew. Chem.*, 2010, **122**, 6796–6799.
- 43 A. Yella, H.-W. Lee, H. N. Tsao, C. Yi, A. K. Chandiran, M. K. Nazeeruddin, E. W.-G. Diau, C.-Y. Yeh, S. M. Zakeeruddin and M. Grätzel, *Science*, 2011, **334**, 629–634.
- 44 S. Mathew, A. Yella, P. Gao, R. Humphry-Baker, F. E. Curchod, N. Ashari-Astani, I. Tavernelli, U. Rothlisberger, K. Nazeeruddin and M. Grätzel, *Nat. Chem.*, 2014, **6**, 242–247.
- 45 M. K. Nazeeruddin, A. Kay, I. Rodicio, R. Humphry-Baker, E. Mueller, P. Liska, N. Vlachopoulos and M. Grätzel, *J. Am. Chem. Soc.*, 1993, **115**, 6382–6390.
- 46 A. Fakharuddin, R. Jose, T. M. Brown, F. Fabregat-Santiago and J. Bisquert, *Energy Environ. Sci.*, 2014, **7**, 3952–3981.
- 47 S. Ahmad, E. Guillen, L. Kavan, M. Grätzel and M. K. Nazeeruddin, *Energy Environ. Sci.*, 2013, **6**, 3439–3466.
- 48 M. Ye, X. Wen, M. Wang, J. Iocozzia, N. Zhang, C. Lin and Z. Lin, *Mater. Today*, 2015, **18**, 155–162.
- 49 L. M. Peter, *J. Phys. Lett.*, 2011, **2**, 1861–1867.
- 50 R. F. Service, *Science*, 2014, **344**, 458.
- 51 S. Yun and X. Wang, *Mater. Lett.*, 2006, **60**, 2211–2213.
- 52 S. Yun, X. Wang, B. Li and D. Xu, *Solid State Commun.*, 2007, **143**, 461–465.
- 53 S. Yun and X. Wang, *J. Electroceram.*, 2008, **21**, 585–588.
- 54 S. Yun, X. Wang and D. Xu, *Mater. Res. Bull.*, 2008, **43**, 1989–1995.
- 55 S. Yun, X. Wang, J. Li, J. Shi and D. Xu, *Mater. Chem. Phys.*, 2009, **116**, 339–343.
- 56 S. Yun, X. Wang, J. Li and D. Xu, *Phys. Status Solidi A*, 2009, **206**, 303–310.
- 57 S. Yun, X. Wang, J. Shi and D. Xu, *J. Alloys Compd.*, 2009, **485**, 610–615.
- 58 S. Yun, X. Wang, J. Shi and D. Xu, *J. Mater. Res.*, 2009, **24**, 3074–3077.
- 59 S. Yun, X. Wang, J. Shi, J. Zhu and D. Xu, *Mater. Lett.*, 2009, **63**, 1883–1885.
- 60 M. Grätzel, *Nat. Mater.*, 2014, **13**, 838–842.
- 61 M. A. Green, A. Ho-Baillie and H. J. Snaith, *Nat. Photonics*, 2014, **8**, 506–514.
- 62 S. Kazim, M. K. Nazeeruddin, M. Grätzel and S. Ahmad, *Angew. Chem., Int. Ed.*, 2014, **53**, 2812–2824.
- 63 J. Xia and S. Yanagida, *Sol. Energy*, 2011, **85**, 3143–3159.
- 64 J. Shi, X. Xu, D. Li and Q. Meng, *Small*, 2015, **11**, 2472–2486.
- 65 M. Grätzel, R. A. Janssen, D. B. Mitzi and E. H. Sargent, *Nature*, 2012, **488**, 304–312.
- 66 Z. Yu and L. Sun, *Adv. Energy Mater.*, 2015, **5**, 1500213.
- 67 C. Zuo, H. J. Bolink, H. Han, J. Huang, D. Cahen and L. Ding, *Adv. Sci.*, 2016, **3**, 1500324.
- 68 I. Chung, B. Lee, J. He, R. P. H. Chang and M. G. Kanatzidis, *Nature*, 2012, **485**, 486–489.
- 69 M. M. Lee, J. Teuscher, T. Miyasaka, T. N. Murakami and H. J. Snaith, *Science*, 2012, **338**, 643–647.
- 70 L. Etgar, *J. Am. Chem. Soc.*, 2012, **134**, 17396–17399.
- 71 A. Mei, X. Li, L. Liu, Z. Ku, T. Liu, Y. Rong, M. Xu, M. Hu, J. Chen, Y. Yang, M. Grätzel and H. Han, *Science*, 2014, **345**, 295–298.
- 72 J. H. Heo, S. H. Im, J. H. Noh, T. N. Mandal, C.-S. Lim, J. A. Chang, Y. H. Lee, H.-j. Kim, A. Sarkar, K. Nazeeruddin, M. Grätzel and S. I. Seok, *Nat. Photonics*, 2013, **7**, 486–491.
- 73 J. Burschka, N. Pellet, S.-J. Moon, R. Humphry-Baker, P. Gao, M. K. Nazeeruddin and M. Grätzel, *Nature*, 2013, **499**, 316–319.
- 74 M. Liu, M. B. Johnston and H. J. Snaith, *Nature*, 2013, **501**, 395–398.
- 75 J.-Y. Jeng, Y.-F. Chiang, M.-H. Lee, S.-R. Peng, T.-F. Guo, P. Chen and T.-C. Wen, *Adv. Mater.*, 2013, **25**, 3727–3732.
- 76 L. Meng, J. You, T.-F. Guo and Y. Yang, *Acc. Chem. Res.*, 2016, **49**, 155–165.
- 77 W. S. Yang, J. H. Noh, N. J. Jeon, Y. C. Kim, S. Ryu, J. Seo and S. I. Seok, *Science*, 2015, **348**, 1234–1237.
- 78 H. Zhou, Q. Chen, G. Li, S. Luo, T.-b. Song, H.-S. Duan, Z. Hong, J. You, Y. Liu and Y. Yang, *Science*, 2014, **345**, 542–546.
- 79 N. J. Jeon, J. H. Noh, W. S. Yang, Y. C. Kim, S. Ryu, J. Seo and S. I. Seok, *Nature*, 2015, **517**, 476–480.
- 80 J. H. Noh, S. H. Im, J. H. Heo, T. N. Mandal and S. I. Seok, *Nano Lett.*, 2013, **13**, 1764–1769.
- 81 N. J. Jeon, J. H. Noh, Y. C. Kim, W. S. Yang, S. Ryu and S. I. Seok, *Nat. Mater.*, 2014, **13**, 897–903.
- 82 J. H. Im, *Nanoscale*, 2011, **3**, 4088–4093.
- 83 A. Kojima, K. Teshima, Y. Shirai and T. Miyasaka, *J. Am. Chem. Soc.*, 2009, **131**, 6050–6051.
- 84 J. Burschka, *J. Am. Chem. Soc.*, 2011, **133**, 18042–18045.
- 85 J. Krüger, R. Plass, L. Cevey, M. Piccirelli, M. Grätzel and U. Bach, *Appl. Phys. Lett.*, 2001, **79**, 2085–2087.
- 86 J. Krüger, R. Plass, M. Grätzel and H.-J. Matthieu, *Appl. Phys. Lett.*, 2002, **81**, 367–369.
- 87 L. Schmidt-Mende, U. Bach, R. Humphry-Baker, T. Horiuchi, H. Miura, S. Ito, S. Uchida and M. Grätzel, *Adv. Mater.*, 2005, **17**, 813–815.

- 88 M. Wang, S.-J. Moon, M. Xu, K. Chittibabu, P. Wang, N.-L. Cevey-Ha, R. Humphry-Baker, S. M. Zakeeruddin and M. Grätzel, *Small*, 2010, **6**, 319–324.
- 89 N. Cai, S.-J. Moon, L. Cevey-Ha, T. Moehl, R. Humphry-Baker, P. Wang, S. M. Zakeeruddin and M. Grätzel, *Nano Lett.*, 2011, **11**, 1452–1456.
- 90 U. Bach, *Nature*, 1998, **395**, 583–585.
- 91 H. S. Kim, C. R. Lee, J. H. Im, K. B. Lee, T. Moehl, A. Marchioro, S. J. Moon, R. Humphry-Baker, J. H. Yum, J. E. Moser, M. Grätzel and N. G. Park, *Sci. Rep.*, 2012, **2**, 591.
- 92 M. Saliba, T. Matsui, K. Domanski, J.-Y. Seo, A. Ummadisingu, S. M. Zakeeruddin, J.-P. Correa-Baena, W. R. Tress, A. Abate, A. Hagfeldt and M. Grätzel, *Science*, 2016, **354**, 206–209.
- 93 J. P. Correa Baena, L. Steier, W. Tress, M. Saliba, S. Neutzner, T. Matsui, F. Giordano, T. J. Jacobsson, A. R. Srimath Kandada, S. M. Zakeeruddin, A. Petrozza, A. Abate, M. K. Nazeeruddin, M. Grätzel and A. Hagfeldt, *Energy Environ. Sci.*, 2015, **8**, 2928–2934.
- 94 J.-P. Correa-Baena, A. Abate, M. Saliba, W. Tress, T. Jesper Jacobsson, M. Grätzel and A. Hagfeldt, *Energy Environ. Sci.*, 2017, **10**, 710–727.
- 95 G. Hodes, *Science*, 2013, **342**, 317–318.
- 96 N.-G. Park, *Mater. Today*, 2015, **18**, 65–72.
- 97 S. Wang, Y. Jiang, E. J. Juarez-Perez, L. K. Ono and Y. Qi, *Nat. Energy*, 2016, **2**, 16195.
- 98 T. Zhang, X. Meng, Y. Bai, S. Xiao, C. Hu, Y. Yang, H. Chen and S. Yang, *J. Mater. Chem. A*, 2017, **5**, 1103–1111.
- 99 B. Wu, Y. Zhou, G. Xing, Q. Xu, H. F. Garces, A. Solanki, T. W. Goh, N. P. Padture and T. C. Sum, *Adv. Funct. Mater.*, 2017, 1604818.
- 100 K. P. Marshall, M. Walker, R. I. Walton and R. A. Hatton, *Nat. Energy*, 2016, **1**, 16178.
- 101 T. Todorov, O. Gunawan and S. Guha, *Mol. Syst. Des. Eng.*, 2016, **1**, 370–376.
- 102 G. Abdeltameed, L. Jewell, K. Hellier, L. Seymour, B. Luo, F. Bridges, J. Z. Zhang and S. Carter, *Appl. Phys. Lett.*, 2016, **109**, 233905.
- 103 J. Chen, X. Cai, D. Yang, D. Song, J. Wang, J. Jiang, A. Ma, S. Lv, M. Z. Hu and C. Ni, *J. Power Sources*, 2017, **355**, 98–133.
- 104 X. Zhao and N.-G. Park, *Photonics*, 2015, **2**, 1139–1151.
- 105 D. Wang, M. Wright, N. K. Elumalai and A. Uddin, *Sol. Energy Mater. Sol. Cells*, 2016, **147**, 255–275.
- 106 G. Niu, X. Guo and L. Wang, *J. Mater. Chem. A*, 2015, **3**, 8970–8980.
- 107 G. Hodes and D. Cahen, *Acc. Chem. Res.*, 2012, **45**, 705–713.
- 108 C.-C. Chueh, C.-Z. Li and A. K. Y. Jen, *Energy Environ. Sci.*, 2015, **8**, 1160–1189.
- 109 P. Gao, M. Grätzel and M. K. Nazeeruddin, *Energy Environ. Sci.*, 2014, **7**, 2448–2463.
- 110 T. C. Sum and N. Mathews, *Energy Environ. Sci.*, 2014, **7**, 2518–2534.
- 111 T. Salim, S. Sun, Y. Abe, A. Krishna, A. C. Grimsdale and Y. M. Lam, *J. Mater. Chem. A*, 2015, **3**, 8943–8969.
- 112 H.-S. Kim, S. H. Im and N.-G. Park, *J. Phys. Chem. C*, 2014, **118**, 5615–5625.
- 113 J. Bisquert, *J. Phys. Chem. Lett.*, 2013, **4**, 2597–2598.
- 114 N.-G. Park, *J. Phys. Chem. Lett.*, 2013, **4**, 2423–2429.
- 115 H. J. Snaith, *J. Phys. Chem. Lett.*, 2013, **4**, 3623–3630.
- 116 S. Shi, Y. Li, X. Li and H. Wang, *Mater. Horiz.*, 2015, **2**, 378–405.
- 117 M. Grätzel and N.-G. Park, *Nano*, 2014, **9**, 1440002.
- 118 L. Sun, *Nat. Chem.*, 2015, **7**, 684–685.
- 119 S. D. Stranks and H. J. Snaith, *Nat. Nanotechnol.*, 2015, **10**, 391–402.
- 120 J. H. Rhee, C.-C. Chung and E. W.-G. Diau, *NPG Asia Mater.*, 2013, **5**, e68.
- 121 J. Fan, B. Jia and M. Gu, *Photonics Res.*, 2014, **2**, 111–120.
- 122 H. S. Jung and N.-G. Park, *Small*, 2015, **11**, 10–25.
- 123 H. Youn, H. J. Park and L. J. Guo, *Small*, 2015, **11**, 2228–2246.
- 124 M. Shahbazi and H. Wang, *Sol. Energy*, 2016, **123**, 74–87.
- 125 W. Yan, S. Ye, Y. Li, W. Sun, H. Rao, Z. Liu, Z. Bian and C. Huang, *Adv. Energy Mater.*, 2016, **6**, 1600474.
- 126 N. H. Tiep, Z. Ku and H. J. Fan, *Adv. Energy Mater.*, 2016, **6**, 1501420.
- 127 Y. Rong, L. Liu, A. Mei, X. Li and H. Han, *Adv. Energy Mater.*, 2015, **5**, 1501066.
- 128 R. Fan, Y. Huang, L. Wang, L. Li, G. Zheng and H. Zhou, *Adv. Energy Mater.*, 2016, **6**, 1600460.
- 129 Z. Wu, T. Song and B. Sun, *ChemNanoMat*, 2017, **3**, 75–88.
- 130 Z. Yang, J. Ren, Z. Zhang, X. Chen, G. Guan, L. Qiu, Y. Zhang and H. Peng, *Chem. Rev.*, 2015, **115**, 5159–5223.
- 131 X. Fang and H. Peng, *Small*, 2015, **11**, 1488–1511.
- 132 T. Chen, L. Qiu, Z. Yang, Z. Cai, J. Ren, H. Li, H. Lin, X. Sun and H. Peng, *Angew. Chem., Int. Ed.*, 2012, **51**, 11977–11980.
- 133 W. Guo, X. Xue, S. Wang, C. Lin and Z. L. Wang, *Nano Lett.*, 2012, **12**, 2520–2523.
- 134 N. J. Guilar, T. J. Kleeburg, A. Chen, D. R. Yankelevich and R. Amirtharajah, *IEEE Transactions on Very Large Scale Integration (VLSI) Systems*, 2009, **17**, 627–637.
- 135 T. Chen, L. Qiu, Z. Yang and H. Peng, *Chem. Soc. Rev.*, 2013, **42**, 5031–5041.
- 136 J. Luo, J.-H. Im, M. T. Mayer, M. Schreier, M. K. Nazeeruddin, N.-G. Park, S. D. Tilley, H. J. Fan and M. Grätzel, *Science*, 2014, **345**, 1593–1596.
- 137 C. Xu, C. Pan, Y. Liu and Z. L. Wang, *Nano Energy*, 2012, **1**, 259–272.
- 138 J. L. Xie, C. X. Guo and C. M. Li, *Energy Environ. Sci.*, 2014, **7**, 2559–2579.
- 139 X. Wang and G. Shi, *Energy Environ. Sci.*, 2015, **8**, 790–823.
- 140 F. Bonaccorso, L. Colombo, G. Yu, M. Stoller, V. Tozzini, A. C. Ferrari, R. S. Ruoff and V. Pellegrini, *Science*, 2015, **347**, 1246501.
- 141 Z. Yang, L. Li, Y. Luo, R. He, L. Qiu, H. Lin and H. Peng, *J. Mater. Chem. A*, 2013, **1**, 954–958.
- 142 F. Bonaccorso, L. Colombo, G. Yu, M. Stoller, V. Tozzini, A. C. Ferrari, R. S. Ruoff and V. Pellegrini, *Science*, 2015, 347.

- 143 H. Sun, J. Deng, L. Qiu, X. Fang and H. Peng, *Energy Environ. Sci.*, 2015, **8**, 1139–1159.
- 144 S. Pan, Z. Zhang, W. Weng, H. Lin, Z. Yang and H. Peng, *Mater. Today*, 2014, **17**, 276–284.
- 145 X. Fan, M. Zhang, X. Wang, F. Yang and X. Meng, *J. Mater. Chem. A*, 2013, **1**, 8694–8709.
- 146 P.-W. Liang, C.-Y. Liao, C.-C. Chueh, F. Zuo, S. T. Williams, X.-K. Xin, J. Lin and A. K. Y. Jen, *Adv. Mater.*, 2014, **26**, 3748–3754.
- 147 C. Wehrenfennig, G. E. Eperon, M. B. Johnston, H. J. Snaith and L. M. Herz, *Adv. Mater.*, 2014, **26**, 1584–1589.
- 148 Z. Xiao, C. Bi, Y. Shao, Q. Dong, Q. Wang, Y. Yuan, C. Wang, Y. Gao and J. Huang, *Energy Environ. Sci.*, 2014, **7**, 2619–2623.
- 149 L. Etgar, P. Gao, Z. Xue, Q. Peng, A. K. Chandiran, B. Liu, M. K. Nazeeruddin and M. Grätzel, *J. Am. Chem. Soc.*, 2012, **134**, 17396–17399.
- 150 S. D. Stranks, *Science*, 2013, **342**, 341–344.
- 151 G. Xing, *Science*, 2013, **342**, 344–347.
- 152 T. Ameri, G. Dennler, C. Lungenschmied and C. J. Brabec, *Energy Environ. Sci.*, 2009, **2**, 347–363.
- 153 A. Polman and H. A. Atwater, *Nat. Mater.*, 2012, 174–177.
- 154 P. T. Chiu, D. C. Law, R. L. Woo, S. B. Singer, D. Bhusari, W. D. Hong, A. Zakaria, J. Boisvert, S. Mesropian, R. R. King and N. H. Karam, 40th IEEE Photovoltaic Specialist Conference (PVSC), 2014, 0011.
- 155 S. De Wolf, J. Holovsky, S.-J. Moon, P. Löper, B. Niesen, M. Ledinsky, F.-J. Haug, J.-H. Yum and C. Ballif, *J. Phys. Chem. Lett.*, 2014, **5**, 1035–1039.
- 156 G. E. Eperon, T. Leijtens, K. A. Bush, R. Prasanna, T. Green, J. T.-W. Wang, D. P. McMeekin, G. Volonakis, R. L. Milot, R. May, A. Palmstrom, D. J. Slotcavage, R. A. Belisle, J. B. Patel, E. S. Parrott, R. J. Sutton, W. Ma, F. Moghadam, B. Conings, A. Babayigit, H.-G. Boyen, S. Bent, F. Giustino, L. M. Herz, M. B. Johnston, M. D. McGehee and H. J. Snaith, *Science*, 2016, aaf9717.
- 157 G. E. Eperon, S. D. Stranks, C. Menelaou, M. B. Johnston, L. M. Herz and H. J. Snaith, *Energy Environ. Sci.*, 2014, **7**, 982–988.
- 158 J. You, Z. Hong, Y. Yang, Q. Chen, M. Cai, T.-B. Song, C.-C. Chen, S. Lu, Y. Liu and H. Zhou, *ACS Nano*, 2014, **8**, 1674–1680.
- 159 E. T. Hoke, D. J. Slotcavage, E. R. Dohner, A. R. Bowring, H. I. Karunadasa and M. D. McGehee, *Chem. Sci.*, 2015, **6**, 613–617.
- 160 M. Freitag, Q. Daniel, M. Pazoki, K. Sveinbjornsson, J. Zhang, L. Sun, A. Hagfeldt and G. Boschloo, *Energy Environ. Sci.*, 2015, **8**, 2634–2637.
- 161 A. Steve, S. Michael, C.-B. Juan-Pablo, J. Klaus, K. Lars, H. Anders, G. Michael and R. Bernd, *J. Opt.*, 2016, **18**, 064012.
- 162 M. A. Green and T. Bein, *Nat. Mater.*, 2015, **14**, 559–561.
- 163 Z. Yu, M. Leilaieoun and Z. Holman, *Nat. Energy*, 2016, **1**, 16137.
- 164 M. H. Futscher and B. Ehrler, *ACS Energy Lett.*, 2016, **1**, 863–868.
- 165 S. Albrecht, M. Saliba, J.-P. Correa-Baena, K. Jäger, L. Korte, A. Hagfeldt, M. Grätzel and B. Rech, *J. Opt.*, 2016, **18**, 064012.
- 166 W. Zhu, C. Bao, F. Li, X. Zhou, J. Yang, T. Yu and Z. Zou, *Chem. Commun.*, 2016, **52**, 304–307.
- 167 B. Suarez, V. Gonzalez-Pedro, T. S. Ripolles, R. S. Sanchez, L. Otero and I. Mora-Sero, *J. Phys. Chem. Lett.*, 2014, **5**, 1628–1635.
- 168 C. Bi, Y. Yuan, Y. Fang and J. Huang, *Adv. Energy Mater.*, 2015, **5**, 1401616.
- 169 E. T. Hoke, D. J. Slotcavage, E. R. Dohner, A. R. Bowring, H. I. Karunadasa and M. D. McGehee, *Chem. Sci.*, 2015, **6**, 613–617.
- 170 Z. Yang, A. Rajagopal, S. B. Jo, C.-C. Chueh, S. Williams, C.-C. Huang, J. K. Katahara, H. W. Hillhouse and A. K.-Y. Jen, *Nano Lett.*, 2016, **16**, 7739–7747.
- 171 C. D. Bailie and M. D. McGehee, *MRS Bull.*, 2015, **40**, 681–686.
- 172 A. Ibraheem, H.-B. Anita and A. G. Martin, *Jpn. J. Appl. Phys.*, 2015, **54**, 08KD04.
- 173 M. Filipič, P. Löper, B. Niesen, S. De Wolf, J. Krč, C. Ballif and M. Topič, *Opt. Express*, 2015, **23**, A263–A278.
- 174 S. Foster and S. John, *J. Appl. Phys.*, 2016, **120**, 103103.
- 175 D. T. Grant, K. R. Catchpole, K. J. Weber and T. P. White, *Opt. Express*, 2016, **24**, A1454–A1470.
- 176 Y. Jiang, I. Almansouri, S. Huang, T. Young, Y. Li, Y. Peng, Q. Hou, L. Spiccia, U. Bach, Y.-B. Cheng, M. A. Green and A. Ho-Baillie, *J. Mater. Chem. C*, 2016, **4**, 5679–5689.
- 177 D. Shi, Y. Zeng and W. Shen, *Sci. Rep.*, 2015, **5**, 16504.
- 178 P. Loper, S. Moon, S. M. deNicolas, B. Niesen, M. Ledinsky, S. Nicolay, J. Bailat, J. Yum, S. DeWolf and C. Ballif, *Phys. Chem. Chem. Phys.*, 2015, **17**, 1619–1629.
- 179 P. Loper, B. Niesen, S.-J. Moon, S. Martin de Nicolas, J. Holovsky, Z. Remes, M. Ledinsky, F.-J. Haug, J.-H. Yum, S. De Wolf and C. Ballif, *IEEE J. Photovolt.*, 2014, **4**, 1545–1551.
- 180 R. Pandey and R. Chaujar, *Superlattices Microstruct.*, 2016, **100**, 656–666.
- 181 N. N. Lal, T. P. White and K. R. Catchpole, *IEEE J. Photovolt.*, 2014, **4**, 1380–1386.
- 182 K. Masuko, M. Shigematsu, T. Hashiguchi, D. Fujishima, M. Kai, N. Yoshimura, T. Yamaguchi, Y. Ichihashi, T. Mishima, N. Matsubara, T. Yamanishi, T. Takahama, M. Taguchi, E. Maruyama and S. Okamoto, *IEEE J. Photovolt.*, 2014, **4**, 1433–1435.
- 183 M. A. Green, *Sol. Energy Mater. Sol. Cells*, 2015, **143**, 190–197.
- 184 A. W. Blakers, A. Wang, A. M. Milne, J. Zhao and M. A. Green, *Appl. Phys. Lett.*, 1989, **55**, 1363–1365.
- 185 M. A. Green, *Prog. Photovoltaics Res. Appl.*, 2009, **17**, 183–189.
- 186 A. Wang, J. Zhao and M. A. Green, *Appl. Phys. Lett.*, 1990, **57**, 602–604.
- 187 S. De Wolf, A. Descoedres, C. Holman Zachary and C. Ballif, *Green*, 2012, **2**, 7.
- 188 E. Franklin, K. Fong, K. McIntosh, A. Fell, A. Blakers, T. Kho, D. Walter, D. Wang, N. Zin, M. Stocks, E.-C.

- Wang, N. Grant, Y. Wan, Y. Yang, X. Zhang, Z. Feng and P. J. Verlinden, *Prog. Photovoltaics Res. Appl.*, 2016, **24**, 411–427.
- 189 B. C. Duck, R. B. Dunbar, O. Lee, K. F. Anderson, T. W. Jones, G. J. Wilson and C. J. Fell, 43rd IEEE Photovoltaic Specialists Conference (PVSC), 2016, pp. 1624–1629, DOI: 10.1109/PVSC.2016.7749896.
- 190 I. L. Braly, R. J. Stoddard, A. Rajagopal, A. R. Uhl, J. K. Katahara, A. K. Y. Jen and H. W. Hillhouse, *ACS Energy Lett.*, 2017, **2**, 1841–1847.
- 191 F. Lang, M. A. Gluba, S. Albrecht, J. Rappich, L. Korte, B. Rech and N. H. Nickel, *J. Phys. Chem. Lett.*, 2015, **6**, 2745–2750.
- 192 C. D. Bailie, M. G. Christoforo, J. P. Mailoa, A. R. Bowring, E. L. Unger, W. H. Nguyen, J. Burschka, N. Pellet, J. Z. Lee, M. Grätzel, R. Noufi, T. Buonassisi, A. Salleo and M. D. McGehee, *Energy Environ. Sci.*, 2015, **8**, 956–963.
- 193 K. A. Bush, C. D. Bailie, Y. Chen, A. R. Bowring, W. Wang, W. Ma, T. Leijtens, F. Moghadam and M. D. Gehee, *Adv. Mater.*, 2016, **28**, 3937–3943.
- 194 T. Duong, N. Lal, D. Grant, D. Jacobs, P. Zheng, S. Rahman, H. Shen, M. Stocks, A. Blakers, K. Weber, T. P. White and K. R. Catchpole, *IEEE J. Photovolt.*, 2016, **6**, 679–687.
- 195 D. P. McMeekin, G. Sadoughi, W. Rehman, G. E. Eperon, M. Saliba, M. T. Hörantner, A. Haghighirad, N. Sakai, L. Korte, B. Rech, M. B. Johnston, L. M. Herz and H. J. Snaith, *Science*, 2016, **351**, 151–155.
- 196 B. Chen, Y. Bai, Z. Yu, T. Li, X. Zheng, Q. Dong, L. Shen, M. Boccard, A. Gruverman, Z. Holman and J. Huang, *Adv. Energy Mater.*, 2016, **6**, 1601128.
- 197 Z. Ren, J. Zhou, A. Ng, Q. Shen, H. Shen and C. Surya, 43rd IEEE Photovoltaic Specialists Conference (PVSC), 2016, pp. 816–820.
- 198 J. Peng, T. Duong, X. Zhou, H. Shen, Y. Wu, H. K. Mulmudi, Y. Wan, D. Zhong, J. Li, T. Tsuzuki, K. J. Weber, K. R. Catchpole and T. P. White, *Adv. Energy Mater.*, 2017, **7**, 1601768.
- 199 B. Niesen, J. Werner, A. Walter, J. P. Seif, C. Allebé, D. Sacchetto, M. Despeisse, S. J. Moon, S. Nicolay, S. D. Wolf and C. Ballif, 43rd IEEE Photovoltaic Specialists Conference (PVSC), 2016, p 0077.
- 200 J. Werner, L. Barraud, A. Walter, M. Bräuninger, F. Sahli, D. Sacchetto, N. Tétreault, B. Paviet-Salomon, S.-J. Moon, C. Allebé, M. Despeisse, S. Nicolay, S. D. Wolf, B. Niesen and C. Ballif, *ACS Energy Lett.*, 2016, **1**, 474–480.
- 201 T. Duong, Y. Wu, H. Shen, J. Peng, X. Fu, D. Jacobs, E.-C. Wang, T. C. Kho, K. C. Fong, M. Stocks, E. Franklin, A. Blakers, N. Zin, K. McIntosh, W. Li, Y.-B. Cheng, T. P. White, K. Weber and K. Catchpole, *Adv. Energy Mater.*, 2017, **7**, 1700228.
- 202 F. Matteocci, S. Razza, S. Casaluci, N. Yaghoobiniya, A. D. Carlo, L. Serenelli, M. Izzì, G. Stracci, A. Mittiga and M. Tucci, 2nd IEEE Photovoltaic Specialist Conference (PVSC), 2015, pp. 1–6.
- 203 H. Kanda, A. Uzum, H. Nishino, T. Umeyama, H. Imahori, Y. Ishikawa, Y. Uraoka and S. Ito, *ACS Appl. Mater. Interfaces*, 2016, **8**, 33553–33561.
- 204 A. Mojiri, R. Taylor, E. Thomsen and G. Rosengarten, *Renewable Sustainable Energy Rev.*, 2013, **28**, 654–663.
- 205 A. G. Imenes and D. R. Mills, *Sol. Energy Mater. Sol. Cells*, 2004, **84**, 19–69.
- 206 H. Uzu, M. Ichikawa, M. Hino, K. Nakano, T. Meguro, J. L. Hernández, H.-S. Kim, N.-G. Park and K. Yamamoto, *Appl. Phys. Lett.*, 2015, **106**, 013506.
- 207 R. Sheng, A. W. Y. Ho-Baillie, S. Huang, M. Keevers, X. Hao, L. Jiang, Y.-B. Cheng and M. A. Green, *J. Phys. Chem. Lett.*, 2015, **6**, 3931–3934.
- 208 T. Duong, D. Grant, S. Rahman, A. Blakers, K. J. Weber, K. R. Catchpole and T. P. White, *IEEE J. Photovolt.*, 2016, **6**, 1432–1439.
- 209 Y. Li, H. Hu, B. Chen, T. Salim, J. Zhang, J. Ding, N. Yuan and Y. M. Lam, *J. Mater. Chem. C*, 2017, **5**, 134–139.
- 210 R. Santbergen, R. Mishima, T. Meguro, M. Hino, H. Uzu, J. Blanker, K. Yamamoto and M. Zeman, *Opt. Express*, 2016, **24**, A1288–A1299.
- 211 J. Eisenlohr, B. G. Lee, J. Benick, F. Feldmann, M. Drießen, N. Milenkovic, B. Bläsi, J. C. Goldschmidt and M. Hermle, *Sol. Energy Mater. Sol. Cells*, 2015, **142**, 60–65.
- 212 H. Chung, R. Singh, L. Kumar, M. A. Alam and P. Bermel, 43rd IEEE Photovoltaic Specialists Conference (PVSC), 2016, 3625–3628.
- 213 J. Werner, A. Walter, E. Rucavado, S.-J. Moon, D. Sacchetto, M. Rienaecker, R. Peibst, R. Brendel, X. Niquille, S. D. Wolf, P. Löper, M. Morales-Masis, S. Nicolay, B. Niesen and C. Ballif, *Appl. Phys. Lett.*, 2016, **109**, 233902.
- 214 C. Battaglia, A. Cuevas and S. De Wolf, *Energy Environ. Sci.*, 2016, **9**, 1552–1576.
- 215 D. Zhang, A. Tavakoliyaraki, Y. Wu, R. A. C. M. M. van Swaaij and M. Zeman, *Energy Procedia*, 2011, **8**, 207–213.
- 216 J. P. Mailoa, C. D. Bailie, E. C. Johlin, E. T. Hoke, A. J. Akey, W. H. Nguyen, M. D. McGehee and T. Buonassisi, *Appl. Phys. Lett.*, 2015, **106**, 121105.
- 217 C. D. Bailie, J. P. Mailoa, E. C. Johlin, W. H. Nguyen, E. T. Hoke, A. J. Akey, T. Buonassisi and M. D. McGehee, 42nd IEEE Photovoltaic Specialist Conference (PVSC), 2015, 1–3.
- 218 S. Albrecht, M. Saliba, J. P. C. Baena, F. Lang, L. Kegelmann, M. Mews, L. Steier, A. Abate, J. Rappich, L. Korte, R. Schlatmann, M. K. Nazeeruddin, A. Hagfeldt, M. Grätzel and B. Rech, *Energy Environ. Sci.*, 2015, **9**, 81–88.
- 219 J. Werner, C.-H. Weng, A. Walter, L. Fesquet, J. P. Seif, S. D. Wolf, B. Niesen and C. Ballif, *J. Phys. Chem. Lett.*, 2015, **7**, 161–166.
- 220 K. A. Bush, A. F. Palmstrom, Z. J. Yu, M. Boccard, R. Cheacharoen, J. P. Mailoa, D. P. McMeekin, R. L. Z. Hoyer, C. D. Bailie, T. Leijtens, I. M. Peters, M. C. Minichetti, N. Rolston, R. Prasanna, S. Sofia, D. Harwood, W. Ma, F. Moghadam, H. J. Snaith, T. Buonassisi, Z. C. Holman, S. F. Bent and M. D. McGehee, *Nat. Energy*, 2017, **2**, 17009.
- 221 R. Kamada, T. Yagioka, S. Adachi, A. Handa, K. F. Tai, T. Kato and H. Sugimoto, 43rd IEEE Photovoltaic Specialists Conference, 2016, 1287–1291.

- 222 P. Jackson, R. Wuerz, D. Hariskos, E. Lotter, W. Witte and M. Powalla, *Phys. Status Solidi RRL*, 2016, **10**, 583–586.
- 223 A. Chirilă, S. Buecheler, F. Pianezzi, P. Bloesch, C. Gretener, A. R. Uhl, C. Fella, L. Kranz, J. Perrenoud, S. Seyrling, R. Verma, S. Nishiwaki, Y. E. Romanyuk, G. Bilger and A. N. Tiwari, *Nat. Mater.*, 2011, **10**, 857–861.
- 224 Z. M. Beiley and M. D. McGehee, *Energy Environ. Sci.*, 2012, **5**, 9173–9179.
- 225 M. Bär, W. Bohne, J. Röhrich, E. Strub, S. Lindner, M. C. Lux-Steiner, C.-H. Fischer, T. P. Niesen and F. Karg, *J. Appl. Phys.*, 2004, **96**, 3857–3860.
- 226 A. R. Uhl, J. K. Katahara and H. W. Hillhouse, *Energy Environ. Sci.*, 2016, **9**, 130–134.
- 227 T. Feurer, P. Reinhard, E. Avancini, B. Bissig, J. Löckinger, P. Fuchs, R. Carron, T. P. Weiss, J. Perrenoud, S. Stutterheim, S. Buecheler and A. N. Tiwari, *Prog. Photovoltaics Res. Appl.*, 2017, **25**, 645–667.
- 228 T. Todorov, T. Gershon, O. Gunawan, C. Sturdevant and S. Guha, *Appl. Phys. Lett.*, 2014, **105**, 173902.
- 229 A. De Vos, *J. Phys. D: Appl. Phys.*, 1980, **13**, 839.
- 230 S. R. Kurtz, P. Faine and J. M. Olson, *J. Appl. Phys.*, 1990, **68**, 1890.
- 231 F. Meillaud, A. Shah, C. Droz, E. Vallat-Sauvain and C. Miazza, *Sol. Energy Mater. Sol. Cells*, 2006, **90**, 2952–2959.
- 232 J. P. Mailoa, M. Lee, I. M. Peters, T. Buonassisi, A. Panchula and D. N. Weiss, *Energy Environ. Sci.*, 2016, **9**, 2644–2653.
- 233 M. Saliba, T. Matsui, K. Domanski, J.-Y. Seo, A. Ummadisingu, S. M. Zakeeruddin, J.-P. Correa-Baena, W. R. Tress, A. Abate, A. Hagfeldt and M. Grätzel, *Science*, 2016, **354**, 206–209.
- 234 W. S. Yang, J. H. Noh, N. J. Jeon, Y. C. Kim, S. Ryu, J. Seo and S. I. Seok, *Science*, 2015, **348**, 1234–1237.
- 235 H. Zhou, Q. Chen, G. Li, S. Luo, T.-b. Song, H.-S. Duan, Z. Hong, J. You, Y. Liu and Y. Yang, *Science*, 2014, **345**, 542–546.
- 236 J. H. Heo, H. J. Han, D. Kim, T. K. Ahn and S. H. Im, *Energy Environ. Sci.*, 2015, **8**, 1602–1608.
- 237 Z. Zhu, Y. Bai, X. Liu, C. C. Chueh, S. Yang and A. K. Y. Jen, *Adv. Mater.*, 2016, **28**, 6478–6484.
- 238 S. Ye, W. Sun, Y. Li, W. Yan, H. Peng, Z. Bian, Z. Liu and C. Huang, *Nano Lett.*, 2015, **15**, 3723–3728.
- 239 L. E. Polander, P. Pahnner, M. Schwarze, M. Saalfrank, C. Koerner and K. Leo, *APL Mater.*, 2014, **2**, 081503.
- 240 P.-W. Liang, C.-C. Chueh, S. T. Williams and A. K. Y. Jen, *Adv. Energy Mater.*, 2015, **5**, 1402321.
- 241 J. You, L. Meng, T.-B. Song, T.-F. Guo, Y. M. Yang, W.-H. Chang, Z. Hong, H. Chen, H. Zhou, Q. Chen, Y. Liu, N. D. Marco and Y. Yang, *Nat. Nanotechnol.*, 2015, **11**, 75–81.
- 242 B.-S. Kim, T.-M. Kim, M.-S. Choi, H.-S. Shim and J.-J. Kim, *Org. Electron.*, 2015, **17**, 102–106.
- 243 L. Kranz, A. Abate, T. Feurer, F. Fu, E. Avancini, J. Löckinger, P. Reinhard, S. M. Zakeeruddin, M. Grätzel, S. Buecheler and A. N. Tiwari, *J. Phys. Chem. Lett.*, 2015, **6**, 2676–2681.
- 244 F. Fu, T. Feurer, T. Jäger, E. Avancini, B. Bissig, S. Yoon, S. Buecheler and A. N. Tiwari, *Nat. Commun.*, 2015, **6**, 8932.
- 245 F. Fu, T. Feurer, S. Pisoni, E. Avancini, C. Andres and S. Buecheler, *Nat. Energy*, 2016, **2**, 16190.
- 246 A. Guchhait, H. A. Dewi, S. W. Leow, H. Wang, G. Han, F. B. Suhaimi, S. Mhaisalkar, L. H. Wong and N. Mathews, *ACS Energy Lett.*, 2017, 807–812.
- 247 U. W. Paetzold, M. Jaysankar, R. Gehlhaar, E. Ahlswede, S. Paetel, W. Qiu, J. Bastos, L. Rakocevic, B. S. Richards, T. Aernouts, M. Powalla and J. Poortmans, *J. Mater. Chem. A*, 2017, **5**, 9897–9906.
- 248 M. Lee, S. J. Park, Y. J. Hwang, Y. Jun and B. K. Min, *Adv. Opt. Mater.*, 2016, **4**, 2102–2108.
- 249 Y. M. Yang, Q. Chen, Y.-T. Hsieh, T.-B. Song, N. D. Marco, H. Zhou and Y. Yang, *ACS Nano*, 2015, **9**, 7714–7721.
- 250 A. R. Uhl, Z. Yang, A. K. Y. Jen and H. W. Hillhouse, *J. Mater. Chem. A*, 2017, **5**, 3214–3220.
- 251 A. Chirilă, P. Bloesch, S. Seyrling, A. Uhl, S. Buecheler, F. Pianezzi, C. Fella, J. Perrenoud, L. Kranz, R. Verma, D. Guettler, S. Nishiwaki, Y. E. Romanyuk, G. Bilger, D. Brémaud and A. N. Tiwari, *Prog. Photovoltaics Res. Appl.*, 2011, **19**, 560–564.
- 252 A. R. Uhl, P. Fuchs, A. Rieger, F. Pianezzi, C. M. Sutter-Fella, L. Kranz, D. Keller, H. Hagendorfer, Y. E. Romanyuk, F. LaMattina, S. Yoon, L. Karvonen, T. Magorian-Friedlmeier, E. Ahlswede, D. VanGenechten, F. Stassin and A. N. Tiwari, *Prog. Photovoltaics*, 2015, **23**, 1110–1119.
- 253 Y. E. Romanyuk, H. Hagendorfer, P. Stücheli, P. Fuchs, A. R. Uhl, C. M. Sutter-Fella, M. Werner, S. Haass, J. Stückelberger, C. Broussillou, P. P. Grand, V. Bermudez and A. N. Tiwari, *Adv. Funct. Mater.*, 2015, **25**, 12–27.
- 254 M. Saliba, T. Matsui, J.-Y. Seo, K. Domanski, J.-P. Correa-Baena, M. K. Nazeeruddin, S. M. Zakeeruddin, W. Tress, A. Abate, A. Hagfeldt and M. Grätzel, *Energy Environ. Sci.*, 2016, **9**, 1989–1997.
- 255 B. Conings, J. Drijkoningen, N. Gauquelin, A. Babayigit, J. D'Haen, L. D'Olieslaeger, A. Ethirajan, J. Verbeeck, J. Manca, F. D. Angelis and H. G. Boyen, *Adv. Energy Mater.*, 2015, **5**, 1500477.
- 256 R. K. Misra, S. Aharon, B. Li, D. Mogilyansky, I. Visoly-Fisher, L. Etgar and E. A. Katz, *J. Phys. Chem. Lett.*, 2015, **6**, 326–330.
- 257 S. Kijima and T. Nakada, *Appl. Phys. Express*, 2008, **1**, 075002.
- 258 I. Repins, M. A. Contreras, B. Egaas, C. DeHart, J. Scharf, C. L. Perkins, B. To and R. Noufi, *Prog. Photovoltaics Res. Appl.*, 2008, **16**, 235–239.
- 259 C. Platzer-Björkman, J. Lu, J. Kessler and L. Stolt, *Thin Solid Films*, 2003, **431–432**, 321–325.
- 260 T. Todorov, T. Gershon, O. Gunawan, Y. S. Lee, C. Sturdevant, L. Y. Chang and S. Guha, *Adv. Energy Mater.*, 2015, **5**, 1500799.
- 261 F. Fu, T. Feurer, T. P. Weiss, S. Pisoni, E. Avancini, C. Andres, S. Buecheler and A. N. Tiwari, *Nat. Energy*, 2016, **2**, 16190.
- 262 C.-W. Chen, S.-Y. Hsiao, C.-Y. Chen, H.-W. Kang, Z.-Y. Huang and H.-W. Lin, *J. Mater. Chem. A*, 2015, **3**, 9152–9159.

- 263 G. E. Eperon, T. Leijtens, K. A. Bush, R. Prasanna, T. Green, J. T.-W. Wang, D. P. McMeekin, G. Volonakis, R. L. Milot, R. May, A. Palmstrom, D. J. Slotcavage, R. A. Belisle, J. B. Patel, E. S. Parrott, R. J. Sutton, W. Ma, F. Moghadam, B. Conings, A. Babayigit, H.-G. Boyen, S. Bent, F. Giustino, L. M. Herz, M. B. Johnston, M. D. McGehee and H. J. Snaith, *Science*, 2016, **354**, 861–865.
- 264 M. Anaya, J. P. Correa-Baena, G. Lozano, M. Saliba, P. Anguita, B. Roose, A. Abate, U. Steiner, M. Grätzel, M. E. Calvo, A. Hagfeldt and H. Miguez, *J. Mater. Chem. A*, 2016, **4**, 11214–11221.
- 265 F. Hao, C. C. Stoumpos, D. H. Cao, R. P. H. Chang and M. G. Kanatzidis, *Nat. Photonics*, 2014, **8**, 489–494.
- 266 W. Liao, D. Zhao, Y. Yu, N. Shrestha, K. Ghimire, C. R. Grice, C. Wang, Y. Xiao, A. J. Cimaroli, R. J. Ellingson, N. J. Podraza, K. Zhu, R.-G. Xiong and Y. Yan, *J. Am. Chem. Soc.*, 2016, **138**, 12360–12363.
- 267 Z. Yang, A. Rajagopal, C.-C. Chueh, S. B. Jo, B. Liu, T. Zhao and A. K. Y. Jen, *Adv. Mater.*, 2016, **28**, 8990–8997.
- 268 J. H. Heo and S. H. Im, *Adv. Mater.*, 2016, **28**, 5121–5125.
- 269 F. Jiang, T. Liu, B. Luo, J. Tong, F. Qin, S. Xiong, Z. Li and Y. Zhou, *J. Mater. Chem. A*, 2016, **4**, 1208–1213.
- 270 D. Forgács, L. Gil-Escrig, D. Pérez-Del-Rey, C. Momblona, J. Werner, B. Niesen, C. Ballif, M. Sessolo and H. J. Bolink, *Adv. Energy Mater.*, 2017, **7**, 1602121.
- 271 Y. Ogomi, A. Morita, S. Tsukamoto, T. Saitho, N. Fujikawa, Q. Shen, T. Toyoda, K. Yoshino, S. S. Pandey, T. Ma and S. Hayase, *J. Phys. Chem. Lett.*, 2014, **5**, 1004–1011.
- 272 P. K. Nayak and D. Cahen, *Adv. Mater.*, 2014, **26**, 1622–1628.
- 273 H. J. Snaith, *Adv. Funct. Mater.*, 2010, **20**, 13–19.
- 274 C. Zuo and L. Ding, *J. Mater. Chem. A*, 2015, **3**, 9063–9066.
- 275 Y. Liu, L. A. Renna, M. Bag, Z. A. Page, P. Kim, J. Choi, T. Emrick, D. Venkataraman and T. P. Russell, *ACS Appl. Mater. Interfaces*, 2016, **8**, 7070–7076.
- 276 Y. Liu, Z. Hong, Q. Chen, W. Chang, H. Zhou, T.-B. Song, E. Young, Y. Yang, J. You and G. Li, *Nano Lett.*, 2015, **15**, 662–668.
- 277 J. Kim, G. Kim, H. Back, J. Kong, I.-W. Hwang, T. K. Kim, S. Kwon, J.-H. Lee, J. Lee, K. Yu, C.-L. Lee, H. Kang and K. Lee, *Adv. Mater.*, 2016, **28**, 3159–3165.
- 278 M. Cheng, C. Chen, K. Aitola, F. Zhang, Y. Hua, G. Boschloo, L. Kloo and L. Sun, *Chem. Mater.*, 2016, **28**, 8631–8639.
- 279 K. H. Hendriks, G. H. L. Heintges, V. S. Gevaerts, M. M. Wienk and R. A. J. Janssen, *Angew. Chem., Int. Ed.*, 2013, **52**, 8341–8344.
- 280 M. Yu, X. Ren, L. Ma and Y. Wu, *Nat. Commun.*, 2014, **5**, 5111.
- 281 N. Li, Y. Wang, D. Tang and H. Zhou, *Angew. Chem.*, 2015, **127**, 9403–9406.
- 282 C. Tang, B.-Q. Li, Q. Zhang, L. Zhu, H.-F. Wang, J.-L. Shi and F. Wei, *Adv. Funct. Mater.*, 2016, **26**, 577–585.
- 283 Z. Zheng, H. Guo, F. Pei, X. Zhang, X. Chen, X. Fang, T. Wang and N. Zheng, *Adv. Funct. Mater.*, 2016, **26**, 8952–8959.
- 284 M. M. Ottakam Thotiyl, S. A. Freunberger, Z. Peng, Y. Chen, Z. Liu and P. G. Bruce, *Nat. Mater.*, 2013, **12**, 1050–1056.
- 285 Z. Li, H. B. Wu and X. W. Lou, *Energy Environ. Sci.*, 2016, **9**, 3061–3070.
- 286 F. Hetsch, X. Xu, H. Wang, S. V. Kershaw and A. L. Rogach, *J. Phys. Chem. Lett.*, 2011, **2**, 1879–1887.
- 287 C. Xu, X. Wang and Z. L. Wang, *J. Am. Chem. Soc.*, 2009, **131**, 5866–5872.
- 288 C. Xu and Z. L. Wang, *Adv. Mater.*, 2011, **23**, 873–877.
- 289 C. Pan, W. Guo, L. Dong, G. Zhu and Z. L. Wang, *Adv. Mater.*, 2012, **24**, 3356–3361.
- 290 X. Pu, W. Song, M. Liu, C. Sun, C. Du, C. Jiang, X. Huang, D. Zou, W. Hu and Z. L. Wang, *Adv. Energy Mater.*, 2016, **6**, 1601048.
- 291 J. Chen, Y. Huang, N. Zhang, H. Zou, R. Liu, C. Tao, X. Fan and Z. L. Wang, *Nat. Energy*, 2016, **1**, 16138.
- 292 S. Wang, X. Wang, Z. L. Wang and Y. Yang, *ACS Nano*, 2016, **10**, 5696–5700.
- 293 X. Chen, H. Sun, Z. Yang, G. Guan, Z. Zhang, L. Qiu and H. Peng, *J. Mater. Chem. A*, 2014, **2**, 1897–1902.
- 294 T. Miyasaka and T. N. Murakami, *Appl. Phys. Lett.*, 2004, **85**, 3932–3934.
- 295 T. N. Murakami, N. Kawashima and T. Miyasaka, *Chem. Commun.*, 2005, 3346–3348.
- 296 P. Liu, H. X. Yang, X. P. Ai, G. R. Li and X. P. Gao, *Electrochem. Commun.*, 2012, **16**, 69–72.
- 297 L. Li, Z. Wu, S. Yuan and X.-B. Zhang, *Energy Environ. Sci.*, 2014, **7**, 2101–2122.
- 298 K. Wang, H. Wu, Y. Meng, Y. Zhang and Z. Wei, *Energy Environ. Sci.*, 2012, **5**, 8384–8389.
- 299 M. F. El-Kady and R. B. Kaner, *Nat. Commun.*, 2013, **4**, 1475.
- 300 C. Merlet, C. Péan, B. Rotenberg, P. A. Madden, B. Daffos, P. L. Taberna, P. Simon and M. Salanne, *Nat. Commun.*, 2013, **4**, 2701.
- 301 P. Simon and Y. Gogotsi, *Nat. Mater.*, 2008, **7**, 845–854.
- 302 J. Chmiola, C. Largeot, P.-L. Taberna, P. Simon and Y. Gogotsi, *Science*, 2010, **328**, 480–483.
- 303 N. A. Kelly and T. L. Gibson, *J. Power Sources*, 2011, **196**, 10430–10441.
- 304 Z. Yang, L. Li, H. Lin, Y. Luo, R. He, L. Qiu, J. Ren and H. Peng, *Chem. Phys. Lett.*, 2012, **549**, 82–85.
- 305 X. Zhang, X. Huang, C. Li and H. Jiang, *Adv. Mater.*, 2013, **25**, 4093–4096.
- 306 J. Xu, H. Wu, L. Lu, S.-F. Leung, D. Chen, X. Chen, Z. Fan, G. Shen and D. Li, *Adv. Funct. Mater.*, 2014, **24**, 1840–1846.
- 307 H.-W. Chen, C.-Y. Hsu, J.-G. Chen, K.-M. Lee, C.-C. Wang, K.-C. Huang and K.-C. Ho, *J. Power Sources*, 2010, **195**, 6225–6231.
- 308 H. Nagai and H. Segawa, *Chem. Commun.*, 2004, 974–975.
- 309 H. Chih-Yu, C. Hsin-Wei, L. Kun-Mu, H. Chih-Wei and H. Kuo-Chuan, *J. Power Sources*, 2010, **195**, 6232–6238.
- 310 T. Chen, L. B. Qiu, Z. B. Yang, Z. B. Cai, J. Ren, H. P. Li, H. J. Lin, X. M. Sun and H. S. Peng, *Angew. Chem., Int. Ed.*, 2012, **51**, 11977–11980.

- 311 X. L. Chen, H. Sun, Z. B. Yang, G. Z. Guan, Z. T. Zhang, L. B. Qiu and H. S. Peng, *J. Mater. Chem. A*, 2014, **2**, 1897–1902.
- 312 Z. Yang, J. Deng, H. Sun, J. Ren, S. Pan and H. Peng, *Adv. Mater.*, 2014, **26**, 7038–7042.
- 313 Y. Saito, S. Uchida, T. Kubo and H. Segawa, *Thin Solid Films*, 2010, **518**, 3033–3036.
- 314 N. F. Yan, G. R. Li, G. L. Pan and X. P. Gao, *J. Electrochem. Soc.*, 2012, **159**, A1770–A1774.
- 315 G. A. Niklasson and C. G. Granqvist, *J. Mater. Chem.*, 2007, **17**, 127–156.
- 316 N. Bagheri, A. Aghaei, M. Y. Ghotbi, E. Marzbanrad, N. Vlachopoulos, L. Häggman, M. Wang, G. Boschloo, A. Hagfeldt, M. Skunik-Nuckowska and P. J. Kulesza, *Electrochim. Acta*, 2014, **143**, 390–397.
- 317 C.-Y. Hsu, H.-W. Chen, K.-M. Lee, C.-W. Hu and K.-C. Ho, *J. Power Sources*, 2010, **195**, 6232–6238.
- 318 P. Yang, X. Xiao, Y. Li, Y. Ding, P. Qiang, X. Tan, W. Mai, Z. Lin, W. Wu, T. Li, H. Jin, P. Liu, J. Zhou, C. P. Wong and Z. L. Wang, *ACS Nano*, 2013, **7**, 2617–2626.
- 319 A. P. Cohn, W. R. Erwin, K. Share, L. Oakes, A. S. Westover, R. E. Carter, R. Bardhan and C. L. Pint, *Nano Lett.*, 2015, **15**, 2727–2731.
- 320 J. Bae, Y. J. Park, M. Lee, S. N. Cha, Y. J. Choi, C. S. Lee, J. M. Kim and Z. L. Wang, *Adv. Mater.*, 2011, **23**, 3446–3449.
- 321 X. Xu, S. Li, H. Zhang, Y. Shen, S. M. Zakeeruddin, M. Graetzel, Y.-B. Cheng and M. Wang, *ACS Nano*, 2015, **9**, 1782–1787.
- 322 F. Zhou, Z. Ren, Y. Zhao, X. Shen, A. Wang, Y. Y. Li, C. Surya and Y. Chai, *ACS Nano*, 2016, **10**, 5900–5908.
- 323 H. Sun, Y. Jiang, L. Qiu, X. You, J. Yang, X. Fu, P. Chen, G. Guan, Z. Yang, X. Sun and H. Peng, *J. Mater. Chem. A*, 2015, **3**, 14977–14984.
- 324 H. Xiao, J. Wang, H. Huang, L. Lu, Q. Lin, Z. Fan, X. Chen, C. Jeong, X. Zhu and D. Li, *Nano Energy*, 2015, **11**, 78–87.
- 325 R. Guo, H. Huang, P. Chang, L. Lu, X. Chen, X. Yang, Z. Fan, B. Zhu and D. Li, *Nano Energy*, 2014, **8**, 141–149.
- 326 J. H. Zhao, A. H. Wang, M. A. Green and F. Ferrazza, *Appl. Phys. Lett.*, 1998, **73**, 1991–1993.
- 327 R. Gaudiana, *J. Phys. Chem. Lett.*, 2010, **1**, 1288–1289.
- 328 A. S. Westover, K. Share, R. Carter, A. P. Cohn, L. Oakes and C. L. Pint, *Appl. Phys. Lett.*, 2014, **104**, 213905.
- 329 C. W. Lo, C. S. Li and H. R. Jiang, *AIP Adv.*, 2011, **1**, 042104.
- 330 C.-T. Chien, P. Hiralal, D.-Y. Wang, I. S. Huang, C.-C. Chen, C.-W. Chen and G. A. J. Amaratunga, *Small*, 2015, **11**, 2929–2937.
- 331 Z. Zhang, X. Chen, P. Chen, G. Guan, L. Qiu, H. Lin, Z. Yang, W. Bai, Y. Luo and H. Peng, *Adv. Mater.*, 2014, **26**, 466–470.
- 332 L. Alibabaei, H. Luo, R. L. House, P. G. Hoertz, R. Lopez and T. J. Meyer, *J. Mater. Chem. A*, 2013, **1**, 4133–4145.
- 333 D. L. Ashford, M. K. Gish, A. K. Vannucci, M. K. Brennaman, J. L. Templeton, J. M. Papanikolas and T. J. Meyer, *Chem. Rev.*, 2015, **115**, 13006–13049.
- 334 V. Balzani, A. Credi and M. Venturi, *ChemSusChem*, 2008, **1**, 26–58.
- 335 M. Bonomo and D. Dini, *Energies*, 2016, **9**, 373.
- 336 M. K. Brennaman, R. J. Dillon, L. Alibabaei, M. K. Gish, C. J. Dares, D. L. Ashford, R. L. House, G. J. Meyer, J. M. Papanikolas and T. J. Meyer, *J. Am. Chem. Soc.*, 2016, **138**, 13085–13102.
- 337 R. Brimblecombe, G. C. Dismukes, G. F. Swiegers and L. Spiccia, *Dalton Trans.*, 2009, 9374–9384.
- 338 J. J. Concepcion, R. L. House, J. M. Papanikolas and T. J. Meyer, *Proc. Natl. Acad. Sci. U. S. A.*, 2012, **109**, 15560–15564.
- 339 G. C. Dismukes, R. Brimblecombe, G. A. N. Felton, R. S. Pryadun, J. E. Sheats, L. Spiccia and G. F. Swiegers, *Acc. Chem. Res.*, 2009, **42**, 1935–1943.
- 340 D. Gust, T. A. Moore and A. L. Moore, *Acc. Chem. Res.*, 2009, **42**, 1890–1898.
- 341 L. Hammarström, *Acc. Chem. Res.*, 2015, **48**, 840–850.
- 342 R. L. House, N. Y. M. Iha, R. L. Coppo, L. Alibabaei, B. D. Sherman, P. Kang, M. K. Brennaman, P. G. Hoertz and T. J. Meyer, *J. Photochem. Photobiol., C*, 2015, **25**, 32–45.
- 343 M. D. Kärkäs, O. Verho, E. V. Johnston and B. Åkermark, *Chem. Rev.*, 2014, **114**, 11863–12001.
- 344 A. Singh and L. Spiccia, *Coord. Chem. Rev.*, 2013, **257**, 2607–2622.
- 345 J. R. Swierk and T. E. Mallouk, *Chem. Soc. Rev.*, 2013, **42**, 2357–2387.
- 346 H. Tian, *ChemSusChem*, 2015, **8**, 3746–3759.
- 347 K. J. Young, L. A. Martini, R. L. Milot, R. C. Snoeberger Iii, V. S. Batista, C. A. Schmuttenmaer, R. H. Crabtree and G. W. Brudvig, *Coord. Chem. Rev.*, 2012, **256**, 2503–2520.
- 348 W. J. Youngblood, S.-H. A. Lee, K. Maeda and T. E. Mallouk, *Acc. Chem. Res.*, 2009, **42**, 1966–1973.
- 349 Z. Yu, F. Li and L. Sun, *Energy Environ. Sci.*, 2015, **8**, 760–775.
- 350 G. Liu, K. Du, S. Haussener and K. Wang, *ChemSusChem*, 2016, **9**, 2878–2904.
- 351 M. A. Modestino and S. Haussener, *Annu. Rev. Chem. Biomol. Eng.*, 2015, **6**, 13–34.
- 352 P. Peerakiatkhajohn, J.-H. Yun, S. Wang and L. Wang, *PHOTOE*, 2016, **7**, 012006.
- 353 M. S. Prévot and K. Sivula, *J. Phys. Chem. C*, 2013, **117**, 17879–17893.
- 354 K. Zhang, M. Ma, P. Li, D. H. Wang and J. H. Park, *Adv. Energy Mater.*, 2016, **6**, 1600602.
- 355 J. H. Park and A. J. Bard, *Electrochem. Solid-State Lett.*, 2006, **9**, E5–E8.
- 356 J. K. Kim, K. Shin, S. M. Cho, T.-W. Lee and J. H. Park, *Energy Environ. Sci.*, 2011, **4**, 1465–1470.
- 357 H. Arakawa, C. Shiraishi, M. Tatemoto, H. Kishida, D. Usui, A. Suma, A. Takamisawa and T. Yamaguchi, *Proc. SPIE*, 2007, **6650**, 665003.
- 358 J. Brilllet, M. Cornuz, F. Le Formal, J.-H. Yum, M. Grätzel and K. Sivula, *J. Mater. Res.*, 2010, **25**, 17–24.
- 359 J.-H. Yum, P. Walter, S. Huber, D. Rentsch, T. Geiger, F. Nüesch, F. De Angelis, M. Grätzel and M. K. Nazeeruddin, *J. Am. Chem. Soc.*, 2007, **129**, 10320–10321.
- 360 J. Brilllet, J.-H. Yum, M. Cornuz, T. Hisatomi, R. Solarska, J. Augustynski, M. Grätzel and K. Sivula, *Nat. Photonics*, 2012, **6**, 824–828.

- 361 V. González-Pedro, I. Zarazua, E. M. Barea, F. Fabregat-Santiago, E. de la Rosa, I. Mora-Seró and S. Giménez, *J. Phys. Chem. C*, 2014, **118**, 891–895.
- 362 K. Shin, J.-B. Yoo and J. H. Park, *J. Power Sources*, 2013, **225**, 263–268.
- 363 X. Shi, K. Zhang, K. Shin, M. Ma, J. Kwon, I. T. Choi, J. K. Kim, H. K. Kim, D. H. Wang and J. H. Park, *Nano Energy*, 2015, **13**, 182–191.
- 364 B. D. Sherman, J. J. Bergkamp, C. L. Brown, A. L. Moore, D. Gust and T. A. Moore, *Energy Environ. Sci.*, 2016, **9**, 1812–1817.
- 365 B. D. Sherman, M. V. Sheridan, K.-R. Wee, S. L. Marquard, D. Wang, L. Alibabaei, D. L. Ashford and T. J. Meyer, *J. Am. Chem. Soc.*, 2016, **138**, 16745–16753.
- 366 Y. Qiu, W. Liu, W. Chen, G. Zhou, P.-C. Hsu, R. Zhang, Z. Liang, S. Fan, Y. Zhang and Y. Cui, *Sci. Adv.*, 2016, **2**, e1501764.
- 367 J. H. Kim, Y. Jo, J. H. Kim, J. W. Jang, H. J. Kang, Y. H. Lee, D. S. Kim, Y. Jun and J. S. Lee, *ACS Nano*, 2015, **9**, 11820–11829.
- 368 J. H. Baek, B. J. Kim, G. S. Han, S. W. Hwang, D. R. Kim, I. S. Cho and H. S. Jung, *ACS Appl. Mater. Interfaces*, 2017, **9**, 1479–1487.
- 369 Y.-S. Chen, J. S. Manser and P. V. Kamat, *J. Am. Chem. Soc.*, 2015, **137**, 974–981.
- 370 X. Zhang, B. Zhang, K. Cao, J. Brillat, J. Chen, M. Wang and Y. Shen, *J. Mater. Chem. A*, 2015, **3**, 21630–21636.
- 371 D. Sabba, M. H. Kumar, L. H. Wong, J. Barber, M. Grätzel and N. Mathews, *Nano Lett.*, 2015, **15**, 3833–3839.
- 372 P. Dias, M. Schreier, S. D. Tilley, J. Luo, J. Azevedo, L. Andrade, D. Bi, A. Hagfeldt, A. Mendes, M. Grätzel and M. T. Mayer, *Adv. Energy Mater.*, 2015, **5**, 1501537.
- 373 J. Luo, D. A. Vermaas, D. Bi, A. Hagfeldt, W. A. Smith and M. Grätzel, *Adv. Energy Mater.*, 2016, **6**, 1600100.
- 374 M. Schreier, L. Curvat, F. Giordano, L. Steier, A. Abate, S. M. Zakeeruddin, J. Luo, M. T. Mayer and M. Grätzel, *Nat. Commun.*, 2015, **6**, 7326.
- 375 S. Yun, X. Zhou, J. Even and A. Hagfeldt, *Angew. Chem., Int. Ed.*, 2017, **56**, 15806–15817.
- 376 J. Li, S. Yun, X. Zhou, Y. Hou, W. Fang, T. Zhang and Y. Liu, *Carbon*, 2018, **126**, 145–155.
- 377 Y. Liu, S. Yun, X. Zhou, Y. Hou, T. Zhang, J. Li and A. Hagfeldt, *Electrochim. Acta*, 2017, **242**, 390–399.
- 378 D. M. Powell, R. Fu, K. Horowitz, P. A. Basore, M. Woodhouse and T. Buonassisi, *Energy Environ. Sci.*, 2015, **8**, 3395–3408.
- 379 X. Liu, Y. Feng, H. Cui, F. Liu, X. Hao, G. Conibeer, D. B. Mitzi and M. Green, *Prog. Photovoltaics Res. Appl.*, 2016, **24**, 879–898.
- 380 O. Ergen, S. M. Gilbert, T. Pham, S. J. Turner, M. T. Z. Tan, M. A. Worsley and A. Zettl, *Nat. Mater.*, 2017, **16**, 522–525.
- 381 M. T. Hörantner, T. Leijtens, M. E. Ziffer, G. E. Eperon, M. G. Christoforo, M. D. McGehee and H. J. Snaith, *ACS Energy Lett.*, 2017, **2**, 2506–2513.
- 382 Z. L. Wang, J. Chen and L. Lin, *Energy Environ. Sci.*, 2015, **8**, 2250–2282.